University of California

Santa Barbara

Joint Study of the 1952 Kern County, California Earthquake

A thesis submitted in partial satisfaction

of the requirements for the degree

Master of Science

in

Earth Science

by

Scott James Condon

Committee in charge:

Professor Chen Ji, Chair
Professor Toshiro Tanimoto
Professor Zach Eilon

March 2020

The thesis of Scott James Condon is approved.

_____

Professor Toshiro Tanimoto

_____

Professor Zach Eilon

_____

Professor Chen Ji, Committee Chair

December 2019

Joint Study of the 1952 Kern County, California Earthquake

Copyright © 2020

by

Scott James Condon

Acknowledgements

Abstract

Joint Study of the 1952 Kern County, California Earthquake

by

Scott James Condon

Our understanding of earthquakes that occurred prior to the establishment of the World-Wide Standardized Seismographic Network (WWSSN) is generally limited by the availability of high-quality geophysical observations. As a result, significant variability exists among source studies for important seismic events such as the historic 1952 Kern County, California earthquake. Here, combining reported geodetic observations with a collection of previously unused, local seismic recordings, we conduct a series of inversions to constrain a slip model for the main rupture. Our results suggest that it initiates on a low-angle fault plane with dominant strike-slip motion (strike=49±3°; dip=35±1°; and rake=11±5°) then triggers an abnormally energetic rupture on a high-angle fault plane (strike = 51°, dip = 75°), 2 s later. This energetic rupture, contained within a 9×6 km patch near the hypocenter, accumulates 6–7 m of slip and has a high average static stress-drop (larger than 50 MPa). P-waves excited by this powerful sub-event saturates seismic recordings as far as Berkeley (approximately 430 km away). The total rupture has a duration 23–26 s and a cumulative moment of 7.61×10^{19} Nm, or M_W 7.18. The majority of moment release occurs within a 36 km section in the southwest portion of White Wolf fault (assumed to be 60 km long). The weighted, average rake-angle over the southwest segment of the fault is 47–57°, falling between previous results based on individual seismic or geodetic data sets. Investigation of the regional velocity structure reveals high P-wave velocities near the southwest portion of the White Wolf fault, adjacent to the presumed hypocenter.

Contents

Introduction

The 1952 Kern County earthquake is one of the largest earthquakes to occur in California during the 20th century. This earthquake struck on the morning of July 21st along a portion of the White-Wolf fault, a left-lateral strike-slip fault north of the San Andreas-Garlock junction. Recordings of the main event, along with 267 aftershocks of magnitude 4.0 and greater [*Richter*, 1955], provide an excellent opportunity for seismologists characterizing seismic hazards in Central California. However, because this event struck before the establishment of the World-Wide Standard Seismographic Network (WWSSN), high quality instrumental recordings are not available. Characterization of this event relies on local seismic recordings which are either missing P-wave first-motions or become saturated shortly after their arrival. As a result, fundamental parameters such as earthquake source mechanism vary significantly in the literature. For these reasons, we have combined available triangulation and leveling data with a previously unused strong-motion data set in a finite-fault inversion. This joint analysis, which incorporates both seismic and geodetic constraints, provides a unique depiction of the earthquake's complex slip history and resolves apparent discrepancies among published source mechanisms. With a greater understanding of seismology and the advent of modern analytical tools we have the ability to improve the characterization of mysterious seismic events such as the 1952 Kern County, California earthquake.

This work is divided into four chapters: Previous Works, First-Motion Study, Finite Fault Inversion and Discussion. Each chapter begins with a brief introduction and ends with a summary of important information. Readers less interested in a specific chapter can refer to the table of contents and skip to the desired location.

In chapter one, we review previous works. These works include seismic, geodetic and intensity studies which provide estimates for earthquake magnitude and source mechanisms. We find general agreement among published earthquake magnitudes and disagreement among earthquake source mechanisms. Ultimately, the latter motivated us to re-analyze P-wave first-motion observations in the following chapter.

In chapter two, we use reported P-wave first-motion observations to constrain a source mechanism for the earthquake's rupture initiation. We find surprisingly that none of the previously published source mechanisms can explain these first-motion observations. Our subsequent first-motion focal inversion reveals that the rupture of the 1952 Kern County earthquake initiated with a strike-slip dominant event on a low angle fault plane running parallel with the White Wolf fault system. We investigate the earthquake's complex slip history further in the following chapter.

In chapter three, we conduct a series of finite-fault inversions which combine available triangulation and leveling observations with a previously unused strong-motion data set. This well established inversion technique improves upon previous geodetic studies by allowing us to resolve complex, non-uniform slip. The resulting slip model reveals that the rupture of the 1952 Kern County earthquake consisted of four separate sub-events with cumulative moment consistent with previous studies.

Finally, in chapter four we investigate the relationship between the earthquake's slip history and 3D velocity structures. We find that the distribution of slip along the White Wolf fault is coincident with regions of abnormally high V_P and V_S, and are located beneath transitions from low to high topography.

Chapter 1

Previous Works

Nearly 70 years have elapsed since the 1952 earthquake struck Kern County, California. A number of important source studies have since been published, characterizing the earthquake's complex slip history. A notable collection of works are available in the 1955 California Division of Mines Special Bulletin, *Earthquakes in Kern County California During 1952*. This bulletin includes reports from many influential scientists and provides a comprehensive firsthand geologic and seismic account of the event. Anyone interested in exploring the 1952 Kern County earthquake beyond the contents of this manuscript should begin here.

Despite extensive efforts to understand this mysterious earthquake, important questions regarding its complex slip history remain unanswered. In this chapter, we revisit notable source studies related to source magnitudes and mechanisms. While we find general agreement among source magnitudes in the literature, we find disagreement among source mechanisms. Ultimately, the latter motivates us to revisit this historic event.

1.1 Magnitudes

Studies presented in this chapter show general agreement among seismic, geodetic, and intensity derived magnitude estimates for the 1952 Kern County earthquake. Estimates range from M 7.2–7.4 and have been tabulated for convenience in Table 1.1. General methodologies and other notable findings can be found in the following sections.

TABLE 1.1 SOURCE MAGNITUDES

Source Study	Magnitude Estimate
Gutenberg [1955a]	M_S 7.6–7.7; revised, M_S 7.4
Ben-Menahem [1978]	M_W 7.24
Kanamori and Jennings [1978]	M_L 7.21 ± 0.17; w/ corr. M_L 7.34 ± 0.17
Bolt [1978]	M_L 7.2 ± 0.2
Salditch et al. [2018]	M_I 7.2 ± 0.2
Dunbar et al. [1980]	M_0 0.9 × 10^{20} N m; or M_W 7.27
Stein and Thatcher [1981]	M_0 1.1 × 10^{20} N m; or M_W 7.32
Bawden [2001]	M_0 9.2 ± 0.5 ×10^{19} Nm; or M_W 7.28 ± 0.02

Table 1.1: Collection of seismic, geodetic and intensity derived source magnitudes. Abbreviations: surface-wave magnitude (M_S), moment magnitude (M_W), local magnitude (M_L), intensity dervived magnitude (M_I) and seismic moment (M_0).

1.1.1 M_S, Gutenberg [1955a]

Gutenberg [1955a] published the first magnitude estimate for the 1952 Kern County, California earthquake. He analyzed 278 measured body and surface wave peak amplitudes at stations with epicentral distances from 18°to 160°. The analysis of these recordings yielded an estimate of M_S 7.6–7.7, making it the largest earthquake to strike California since the 1906 San Francisco earthquake. This initial estimate, however, was based on the definition of earthquake magnitude outlined in [*Gutenberg and Richter*, 1942]. It was

later revised to M_S 7.4 after Gutenberg and Richter modified the relationship between peak amplitude and magnitude [*Gutenberg and Richter*, 1955]. This revision is noted at the bottom of page 171 in Gutenberg's [1955a] report:

> "In a letter to *Nature* (1955) Gutenberg and Richter have re-discussed the definition of magnitude. For the main shock the new magnitude M is 7.4 from body waves as well as from surface waves. Revised equations and calculations give a corresponding energy release of 4×10^{23} ergs. The correction C in equation (2) is no longer added, but a correction has to be used if M is calculated from surface waves" [*Gutenberg*, 1955a].

Therefore, the commonly cited M_S of 7.6–7.7 *Gutenberg* [1955a] is used incorrectly [*Kanamori and Jennings*, 1978; *Bolt*, 1978; *Dunbar et al.*, 1980; *Castillo and Zoback*, 1995; *Bawden et al.*, 1997; *Dreger and Savage*, 1999; *Bawden*, 2001; *Brune et al.*, 2004; *Hough et al.*, 2017; *Salditch et al.*, 2018].

1.1.2 M_W, Ben-Menahem [1978]

Ben-Menahem [1978] reanalyzed Gutenberg's [1955a] collection of seismic data using a theory for the wave propagation based on a finite, uniform rupture and constant rupture velocity. In his analysis, he found that a unilateral rupture on a 65 km × 34 km rectangular fault and a rupture velocity of 3.2 km/s could best explain these surface wave amplitudes. This fault plane strikes N50°E, dips 50° to the southeast, has a rake angle of 80° and an average slip of 1.2 m over the entire fault surface. *Ben-Menahem* [1978] used a crustal model with shear wave velocity of 3.59 km/s. Therefore, if we assume a reasonable crustal density of 2.7×10^3 kg/m³, the corresponding seismic moment would be 9.2×10^{19} Nm, or M_W 7.24. We note that this resulting seismic moment is in fact slightly smaller than the GCMT solution for the 1992 Landers earthquake (1.06×10^{19} Nm, or M_W 7.3;

http://www.globalcmt.org) [*Dziewonski et al.*, 1981; *Ekström et al.*, 2012] which also had a larger surface wave magnitude (M_S 7.5; http://www.globalcmt.org) [*Dziewonski et al.*, 1981; *Ekström et al.*, 2012].

1.1.3 M_L, Kanamori and Jennings [1978]

As ground motions resulting from the main shock exceeded the magnification of all Wood-Anderson instruments with epicentral distances less than 600 km, no records were available to estimate local magnitude (M_L) using the standard approach proposed by *Richter* [1935]. *Kanamori and Jennings* [1978] were the first to estimate M_L. They used strong-motion recordings (at Taft, Santa Barbara, Hollywood, and Caltech) to synthesize Wood-Anderson seismograms. This analysis yielded an average M_L estimate of 7.21 ± 0.17. We note that when *Kanamori and Jennings* [1978] calculated synthetic Wood-Anderson instrument responses, they used a static magnification of 2800 rather than the calibrated value of 2080 [*Hutton and Boore*, 1987]. Taking this into consideration, we find the M_L estimate of 7.34 ± 0.17 more fitting.

1.1.4 M_L, Bolt [1978]

The results of *Kanamori and Jennings* [1978] were later supported by *Bolt* [1978]. He extended the distance correction terms of *Richter* [1935], and estimated M_L using two distant and unsaturated Wood-Anderson recordings at Mineral ($\Delta = 630km$) and Arcata ($\Delta = 780km$). The final resulting estimate of M_L 7.2 ± 0.2 is similar to the estimate of M_L 7.21 ± 0.17, proposed by *Kanamori and Jennings* [1978]. To our best knowledge, these M_L estimates are the largest of any earthquake in the literature. We note that local magnitudes in California were predicted to saturate at about M_L 6.4–6.5 in accordance with maximum effective stress drop of 10 MPa [*Brune*, 1970].

1.1.5 M_I, Salditch et al. 2018

The recent intensity study by *Salditch et al.* [2018] used empirically derived intensity prediction equations to estimate a source magnitude for the Kern County main shock. With a primary data set of 1144 reevaluated intensity reports and with intensity prediction equations from *Bakun* [2006] and *Atkinson and Wald* [2007], the analysis yielded an intensity magnitude estimate (M_I) of 7.2 ± 0.2.

1.1.6 M_0, Dunbar et al. [1980]

Using 103 angle changes and 10 elevation changes, *Dunbar et al.* [1980] developed a slip model for the main shock. *Dunbar et al.* [1980] began by converting the triangulation measurements and geodetic network into shear strains averaged over a collection of quadrilaterals. He then modeled the White Wolf fault as single rectangular fault plane, extending 70 km along strike (N50°E) and 20 km down dip (dip angle = 60°) [*Gutenberg*, 1955b]. This fault plane was further divided into four sub-faults which were allowed to move independently of one another. He concluded that the rupture had a cumulative moment of 0.9×10^{20} Nm, or M_W 7.27 [*Hanks and Kanamori*, 1979]. However, *Dunbar et al.* [1980] acknowledged that this estimate is a lower bound because geodetic observations generally have poor sensitivities with greater depths.

1.1.7 M_0, Stein and Thatcher [1981]

Stein and Thatcher [1981] performed a more comprehensive analysis of the triangulation and leveling observations, this time incorporating additional geophysical information. Upon close examination of geodetic data, seismically derived aftershock locations, and surface geology, *Stein and Thatcher* [1981] created a three-segment fault model. This fault geometry differs significantly as compared to Dunbar's [1980] single rectangular

fault plane. Despite this difference, the estimated cumulative moment for their preferred model is 1.1×10^{20} Nm (M_W 7.32), which is consistent with *Dunbar et al.* [1980].

1.1.8 M_0, Bawden [2001]

The most recent geodetic study comes from *Bawden* [2001], who revisited previously discussed works and proposed an alternative fault model. The key difference between this study and the other two geodetic studies is the size and extent of the assumed fault surface, as well as how *Bawden* [2001] represents the geodetic data in his inversion. Unlike *Dunbar et al.* [1980] and *Stein and Thatcher* [1981], *Bawden* [2001] used the geodetic observations directly in his assessment of fault geometry and was able to quantify model misfit through the forward prediction of this data. His resulting slip model is only 60 km long and consists of two right stepping rectangular fault segments striking N50°E and dipping 75° to the southeast. His analysis suggests that strike-slip motions are best resolved for shallow depths (0–5 km) while dip-slip motions are best resolved along the edges of his fault model at shallow to intermediate depths (0–10 km). This conclusion is intuitive when one examines the location and extent of the triangulation and leveling network with respect to the location of the White Wolf fault. Despite these differences, *Bawden* [2001] estimated a final moment of $9.2 \pm 0.5 \times 10^{19}$ Nm, or M_W 7.28 ± 0.02, which agrees with previously published results.

1.2   Source Mechanisms

Previous source studies presented in this chapter have significantly different source mechanisms despite having similar source magnitudes. Seismic studies generally favor source mechanisms with stronger thrust components, whereas geodetic source studies generally favor source mechanisms with stronger strike-slip components. Both seismic

and geodetic methodologies have strengths and weaknesses with regard to the determination of source mechanisms. As a result, they provide conflicting interpretations to the extent and type of faulting that occurred during the main shock. In this section, we address the apparent discrepancies among source mechanisms and discuss the differences in methodologies employed to determine them.

1.2.1   Gutenberg [1955b], 50°/63°/70°

Gutenberg [1955b] published the first focal solution to the 1952 Kern County main shock, using local P-wave first-motions and teleseismic S-wave polarization angles (strike = 50°; dip = 63°; rake = 70°) (Figure 1.1). He used the apparent strike of the White Wolf Fault (N50°E) as an *a priori* condition, and examined P-wave first-motion data from local seismic stations to determine the rupture's dip angle. Assuming the source could be represented by a double-couple source mechanism, Gutenberg estimated a dip angle between 60° and 66° to the southeast (average of 63°). Finally, he used S-wave polarization angles estimated from teleseismic recordings to constrain the direction of slip. He concluded that motion along the White Wolf Fault had 1.4 times greater vertical motion than horizontal, resulting in a rake angle of 70° [*Gutenberg*, 1955b]. Thus, his final source mechanism, 50°/63°/70°, suggests that the main rupture occurred on a steeply dipping fault plane with dominant thrust motion.

1.2.2   Ben-Menahem [1978], 50°/50°/80°

Ben-Menahem [1978] found that a unilateral rupture on a 65 km × 34 km rectangular fault and rupture velocity of 3.2 km/s could best explain surface wave amplitudes reported by *Gutenberg* [1955a]. The resulting source mechanism (strike = 50°; dip = 50°; rake = 80°) (Figure 1.1) supports the observation that seismic studies favor source mechanisms

with strong thrust components. Together, the two studies by *Gutenberg* [1955b] and *Ben-Menahem* [1978] provide an important seismic description of the White Wolf fault and the surrounding stress-field orientation. An advantage to using seismic data in the determination of source mechanisms is the ability to include observations from distant stations, unlike geodetic studies, which have limited spatial resolution. One trade off, however, is that large magnitude earthquakes typically exhibit complex slip behavior. As a result, the source mechanisms presented by *Gutenberg* [1955b] and *Ben-Menahem* [1978] may be considered over-simplistic. We know, in some circumstances, the orientation of the fault surface and direction of slip changes throughout the rupture propagation.

1.2.3   Dunbar et al. [1980], rake = 40°–20°

Dunbar et al. [1980] modeled the White Wolf fault as a single rectangular fault plane extending 70 km along strike (N50°E) and 20 km down dip (with a dip angle of 60°) [*Gutenberg*, 1955b]. He further discretized the plane into four sub-faults, allowing each to slip independently from one another to best fit the observed triangulation and leveling data. Their corresponding source mechanisms are significantly different as compared to solutions proposed by *Gutenberg* [1955b] and *Ben-Menahem* [1978] (Figure 1.1). They have greater left-lateral strike-slip components compared to reverse dip-slip components. Converting these relative motions into angles of rake, the source mechanisms for the two dominant sub-faults are 50°/60°/40° (southwest segment; 2.5 ± 0.1 strike-slip, 1.9 ± 0.08 reverse) and 50°/60°/20° (northeast segment; 2.3 ± 0.1 strike-slip, 0.58 ± 0.05 reverse) (Figure 1.1) [*Dunbar et al.*, 1980]. This geodetic slip model allows for a more detailed slip history of the 1952 Kern County earthquake as compared to seismic studies .

1.2.4   Stein and Thatcher [1981], rake = 50°–27°–22°

Stein and Thatcher [1981] created an alternative slip model consisting of three independent fault planes. As mentioned in the previous section, these 25 *km* segments have varying degrees of strike and dip. Through their analysis of available geodetic observations and calculated shear strains, *Stein and Thatcher* [1981] found that total displacements decreased and slip direction became more strike-slip dominant moving northeast. The southwest fault segment has 2.4 meters of reverse-slip and 2.0 meters of strike-slip. The central fault has 1.0 meters of reverse-slip and 2.0 meters of strike-slip. The northeast fault segment has 0.4 meters of reverse-slip and 1.0 meters of left-lateral slip. We converted these relative motions into the following three source mechanisms: 73°/ 75°/ 50° (southwest), 58°/ 35°/ 27° (central), 43°/ 20°/ 22° (northeast) (Figure 1.1). In this study, we see a pattern of rake-angle change where the rupture becomes more strike-slip dominant as it propagates northeast along strike. Additionally, the majority of slip within this model is contained within the southwest fault segment near the hypocenter.

1.2.5   Bawden [2001], rake = 24°–88°

Bawden [2001], presents an alternative description of the 1952 Kern County earthquake, utilizing a similar data set. Compared to *Dunbar et al.* [1980] and *Stein and Thatcher* [1981], Bawden's preferred model has considerably larger components of left-lateral strike slip within the southwest segment (rake = 24°) as opposed to the northeast segment (rake = 83°) (Figure 1.1). The southwest fault segment has 1.63 ± 0.03 meters of reverse slip and 3.56 ± 0.32 meters of strike-slip (rake=24°). The northeast fault segment has 1.89 ± 0.04 meters of reverse slip and 0.22 ± 0.14 meters of strike-slip (rake=88°). The pattern of rake-angle change is reversed, where the rupture becomes more thrust-

dominant as it propagates to the northeast. It changes from a low rake-angle of 24° to a high rake angle of 83°moving along strike. This particular aspect of Bawden's slip model sets it apart from previous geodetic studies.

It is worth noting that an important difference among these three geodetic studies is assumed fault geometry. *Dunbar et al.* [1980], *Stein and Thatcher* [1981], and *Bawden* [2001] approximate the earthquake's rupture surface with several rectangular fault planes of varied size and orientation (across which there is uniform slip). As a result, their slip models reflect average displacements over the areas covered by their model and cannot capture small, complex features. With a regular grid-work of numerous sub-faults, however, we may be better able to resolve heterogeneous slip distributions.

1.3   Summary

The characterization of the 1952 Kern County earthquake as one of the largest events to strike California during the last century is apparent, given the agreement among estimates of its magnitude, (M 7.2–7.4). According to our best knowledge, the M_L estimates of 7.2–7.3 *Kanamori and Jennings* [1978] and *Bolt* [1978] are the largest local magnitude estimates of any earthquake to exist in the literature.

Seismically derived source mechanisms proposed by *Gutenberg* [1955b] and *Ben-Menahem* [1978] favor a rupture with dominant thrust components, while geodetic studies by *Dunbar et al.* [1980], *Stein and Thatcher* [1981], and *Bawden* [2001] favor a stronger left-lateral strike-slip component. As seen in Figure 1.1, these solutions have fundamentally different rupture geometries and slip directions, which have broader implications for the surrounding tectonics. For this reason we have reopened the case of Kern County in an attempt to shed light on these apparent discrepancies and improve our understanding of this mysterious earthquake.

FIGURE 1.1 SOURCE MECHANISM COMPILATION

Gutenberg—50/63/70
North

Ben-Menahem—50/50/80
North

Stein & Thatcher 1—73/75/50
North

Dunbar 1—50/60/37
North

Bawden 1—51/75/24
North

Stein & Thatcher 2—58/35/27
North

Dunbar 2—50/60/14
North

Bawden 2 — 51/75/83
North

Stein & Thatcher 3—43/20/22
North
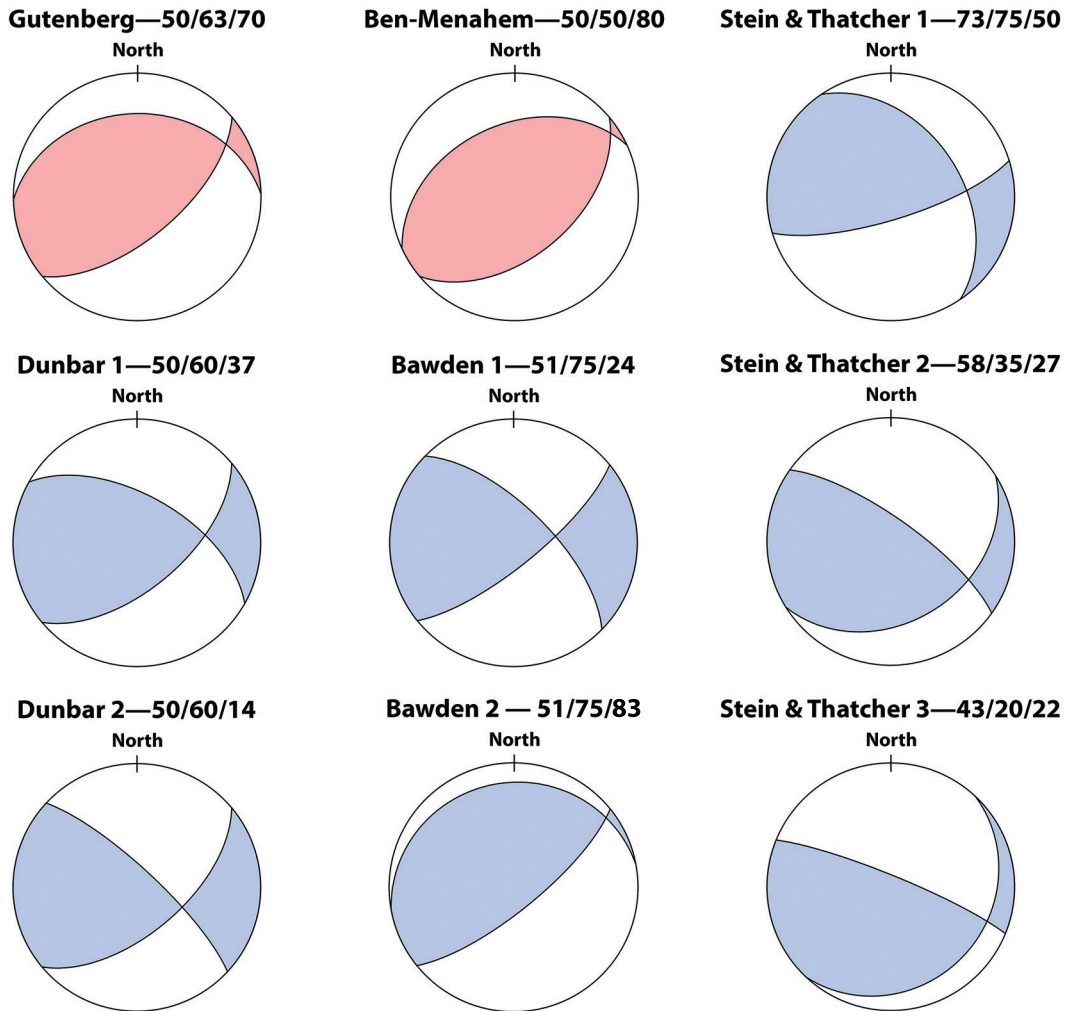
Figure 1.1: Compilation of seismic (red) and geodetic (blue) source mechanisms. All source mechanisms are adapted from relative strike-slip and dip-slip motions. Multiple source mechanisms are indicative of separate sub-events. Studies by *Gutenberg* [1955b] and *Ben-Menahem* [1978] are consistent with local and teleseismic recordings, whereas studies by *Dunbar et al.* [1980], *Stein and Thatcher* [1981] and *Bawden* [2001] are consistent with triangulation and leveling observations.

13

Chapter 2

First-Motion Study

Local seismic analysis of the 1952 Kern County, California earthquake is made challenging due to the limitations presented by analog seismic instruments. At the time, seismographs in California were not calibrated to record large magnitude earthquakes and therefore, many local recordings of this event became saturated shortly after P-wave arrivals [*Benioff*, 1955]. Consequently, there are few local observations from which to infer fault plane solutions. In an attempt to reproduce Gutenberg's source mechanism (strike=50°; dip=63°; and rake=70°) [*Gutenberg*, 1955b], we adopt an inversion strategy that exclusively uses reported local P-wave first-motions [*Gutenberg*, 1955b]. We justify this approach through the analysis of the earthquake's rupture initiation as recorded by the 3-component Wilip-Galitzin seismic instrument in Berkeley, California. These recordings clearly show two impulsive signals, in the form of P-wave first-motions, immediately after rupture initiation. Combined with the observation that both Big Bear and Riverside had small amplitude first-motions with opposite polarity [*Gutenberg*, 1955b], we are able to constrain a source mechanism for the earthquake's rupture initiation (strike=49±3°; dip=35±1°; and rake=11±5°).

2.1   Berkeley Seismic Record

We have digital scans of an instrumental recording that captures the earthquake's rupture initiation. As seen in Figure 2.1, these seismograms were made by a Wilip-Galitzin instrument at the UC Seismology Lab in Berkeley, California (approximately 430 km from the earthquake's epicenter; 35°N, 119°W) [*Gutenberg*, 1955c]. The first visible pulse in these recordings is relatively small, but clearly negative in the up-down (UD) direction. Approximately 2.0 s later, a second, much larger pulse arrives with opposite polarity. The second (compressional) motion exceeds the magnification of the instrument in the north-south (NS) and UD directions. As seen in Figure 2.1, the trace in these components is no longer distinguishable approximately 3 s after the onset of *P*-wave first-motions. We are lucky however, that the EW component of this recording retains the full waveform of this secondary motion, revealing that it is approximately 23 times larger than the first.

2.1.1   Wilip-Galitzin Instrument Response

To explore whether the second motion is an artifact of the Wilip-Galitzin instrument, we have calculated its frequency and time domain response using formulae published in *Lee et al.* [1988]. Figure 2.2 clearly shows a positive impulse (at t=0; duration $\sim$1 s) immediately followed by a lower-frequency signal with smaller, negative amplitude (duration $\sim$3 s). This suggests that the response of any impulsive ground motion will be immediately followed by a wider feedback phase with opposite polarity. We note that this feedback phase also has a much smaller amplitude compared to the original impulse. Given the fact that the second pulse observed at Berkeley (Figure 2.1) is significantly larger than the first, it is safe to conclude that the former cannot be attributed to the instrument's response. Therefore, we entertain the possibility that the first two motions

observed at BRK originated from separate source mechanisms. For the convenience of discussion, we will refer to the first-dilatation as sub-event 1, and the second-compression as sub-event 2.

2.2 *P*-wave Focal Inversion

The Wilip-Galitzin recording clearly suggests that the rupture of the 1952 Kern County, California earthquake began with multiple sub-events. These sub-events could have been nucleation phases with different source mechanisms [*Ellsworth and Beroza*, 1995]. If this were the case, Gutenberg's joint analysis, of local *P*-wave first-motions and teleseismic *S*-wave polarization angles, could lead to an erroneous solution. Seismic signals from sub-event 1 are large enough to be recorded locally, as *P*-wave first-motions. Signals from a much larger sub-event 2, however, would dominate *S*-wave recordings. For this reason, we have adopted a first-motion focal inversion algorithm to constrain a source mechanism for the earthquake's rupture initiation.

2.2.1 *P*-wave Observations

To test whether Gutenberg's solution is consistent with our two sub-event hypothesis, we re-examined local *P*-wave observations [*Gutenberg*, 1955b]. These 11 first-motion observations were recorded by seismic instruments located less than 500 km from the earthquake's epicenter (35°N, 119°W) [*Gutenberg*, 1955c]. As can be seen in Figure 2.3, all stations with the exception of Riverside (RVR) experienced dilatational first-motions. Additionally, first-motion amplitudes recorded at RVR and Big Bear (BBR) were relatively small compared to background noise levels. Gutenberg noted that:

"*The main shock of July 21 P and Pn started with a dilatation at all stations,*

16

except perhaps for Riverside, where the first very short motion is small and possibly a compression. At the Big Bear station, about 50 km northeast of Riverside, the beginning is small, but a clear dilatation" [*Gutenberg*, 1955b].

As we discuss in the next section, this observation provides an important constraint to first-motion focal mechanisms, as RVR and BBR must be in proximity to the nodal plane.

We compare first-motion observations to previously published focal solutions. We adopt a 1D velocity structure for Southern California (Figure 2.4) [*Kanamori and Hadley*, 1975] and a source depth of 15 km (35°N, 119°W, 15±6 km) [*Gutenberg*, 1955c] to calculate azimuth and take-off angles. We plot the resulting information atop previously established source mechanisms. Figure 2.5 shows that none of the published solutions, even the two based on seismic data, agree with the first-motion observations. All solutions with the exception of *Ben-Menahem* [1978] predict the incorrect polarity at BRK and no solution can explain the polarities of RVR and BBR simultaneously.

2.2.2 HASH First-Motion Focal Inversion

We use the HASH inversion algorithm [*Hardebeck and Shearer*, 2002] to constrain first-motion focal mechanisms for the earthquake's rupture initiation. This program uses the 11 P-wave first-motion observations [*Gutenberg*, 1955b] and a 1D velocity structure for Southern California (Figure 2.4) [*Kanamori and Hadley*, 1975], to calculate station azimuth and take-off angles. With this information, HASH conducts a grid search to derive double-couple point-source solutions in a pre-defined model space. In our case, we define model space as any combination of strike (0.01°), dip (2°), and rake (2°) with the corresponding step-intervals. We also modify the source code allowing HASH to find only solutions with zero misfit. If the program finds greater than 500 optimal solutions, it selects and returns a random sample of this larger data set.

In our first test, we specify a source depth (15 km) and location (35°N, 119°W) consistent with *Gutenberg* [1955c]. As a result, HASH finds 14 optimal focal mechanisms, which are tightly grouped around a mean solution (49±3°/ 35±1°/ 11±5°) (Figure 2.6). Note that the strike of this mean solution is similar to the apparent strike of White-Wolf Fault (strike ≈ 50°). In order to satisfy the opposite polarities at RVR and BBR, which have similar azimuth and take-off angles, these stations must be located along nodal planes (Figure 2.6). This puts a strong constraint on the dip-angle of this solution (dip = 35±1°). This mean first-motion focal solution suggests that rupture of the 1952 Kern County, California earthquake initiated with a strike-slip dominant event (rake = 11±5°), on a shallow dipping plane (dip = 35±1°), roughly oriented in the same direction as the White Wolf Fault (strike = 49±3°).

We have performed additional inversions with source depths of 5, 10, and 20 km. Mean solutions corresponding to source depths of 10 km (51±2°/ 36°/ 17±7°) and 20 km (48±5°/ 34±1°/ 10±9°) produce similar results as compared to 15 km (49±3°/ 35±1°/ 11±5°) (Figure 2.6). With a focal depth of 5 km, however, HASH is unable to find a solution that satisfies all *P*-wave first-motions. While there are large uncertainties associated with source depth, we have decided to omit 5 km in further tests.

2.2.3   HASH Solution Stability

According to *Hardebeck and Shearer* [2002], the stability of our solution can be tested by flipping the polarity at a single station and observing the resulting change. Therefore, to further explore our first-motion data [*Gutenberg*, 1955b] we assume that one of the polarity observations is incorrect (9% probability of mis-pick). As a result, HASH returns 500 random solutions that satisfy at least 10 first-motion observations (Figure 2.7). This set of first-motion focal mechanisms does not appear to be well constrained. The strike

of these solutions, for example ranges considerably from 26–352° and is inconsistent with the apparent strike of the White Wolf fault (Figure 2.7).

When we apply an additional constraint to strike (strike = 50±1°) by filtering the 500 solutions, the resulting set of focal mechanisms still vary significantly (50±1°/ 41±11°/ 40±14°). We note that the mean solution of this filtered case has a considerably higher thrust component (rake = 40±14°) as compared to the mean solution with zero misfit (rake = 11±5°). Ultimately, this stability test informs us that all first-motion observations are required to be accurate in order to constrain a unique focal solution for the earthquake's rupture initiation. If the polarity of RVR is changed, the stability of the inversion is reduced considerably.

Again, we examine the results 10 km and 20 km source depths, we obtain similar solutions (Figure 2.8). At a 10 km source depth, the mean solution has a dip of 44±6° and a rake of 37±13°. For 20 km, the mean solution has a dip of 43±7° and a rake of 40±16°. This method does not appear to be depth sensitive, as dips only vary from 41° to 44° and rakes from 37° to 40°. As a result, we cannot put tight bounds on the source depth of this solution, which may vary from 10–20 km.

2.3   Summary

Ground motions produced by the 1952 Kern County, California earthquake led to the saturation of the 3-component Wilip-Galitzin seismic instrument in Berkeley, California (approximately 430 km from the earthquake's epicenter; 35°N, 119°W) [*Gutenberg*, 1955c]. Digital scans of this record (Figure 2.1) reveal two impulsive signals in the form of *P*-wave first-motions. Given the fact that both signals are (1) impulsive in appearance (2) have opposite polarities and (3) different relative magnitudes, it is likely that these signals correspond to different source mechanisms. If this were the case, Gutenberg's

joint analysis, of local P-wave first-motions and teleseismic S-wave polarization angles, would lead to an erroneous point-source solution.

We subsequently revisit the P-wave first-motion observations collected by [*Gutenberg*, 1955b] to evaluate their consistency with previously published source mechanisms. According to Gutenberg, all stations with the exception of Riverside (RVR) experience dilatational first-motions. Additionally, first-motion amplitudes recorded at RVR and Big Bear (BBR) were relatively small compared to background noise levels, indicating that these stations are in proximity to the nodal plane. We note that none of the published solutions, even the two based on seismic data, agree with the first-motion observations (Figure 2.5). All solutions with the exception of *Ben-Menahem* [1978] predict the incorrect polarity at BRK and no solution places RVR and BBR along the nodal plane.

Using Gutenberg's reported P-wave first-motion observations, we constrain a mean focal solution for the earthquake's rupture initiation. To accomplish this we use the HASH inversion algorithm [*Hardebeck and Shearer*, 2002] and conduct a grid search to find optimal solutions with zero misfit. As a result, HASH finds 14 optimal focal mechanisms, which are tightly grouped around a mean solution (49±3°/ 35±1°/ 11±5°) (Figure 2.6). This mean solution is apparently well constrained assuming all reported observations are accurate. It also satisfies two important observations, the known strike of the White Wolf Fault (strike ≈ 50°) and the polarities of RVR and BBR.

We note that this mean solution is highly reliant on the quality of first-motion observations, the accuracy of which is impossible for us to quantify [*Gutenberg*, 1955c]. If we are frugal and assume that one of the polarity observations is incorrect (9% probability of mis-pick) the solution becomes highly unstable. Even if we apply an additional constraint to strike (strike = 50±1°), the spread of acceptable solutions is significant. We note that, on average, this filtered mean produces larger dip and rake angles with greater standard deviations (dip= 41±11° and a rake= 40±14°). While this test emphasizes the

20

importance of each observation in the final inversion we ultimately prefer the focal solution with zero misfit, as it agrees with the apparent strike of White-Wolf Fault (strike $\approx$ 50°) and satisfies the polarities of RVR and BBR, simultaneously. Source depth, however, is not well constrained but is most likely 10–20 km based on previous works (15±6 km) [*Gutenberg*, 1955c] and our limited testing.

Ultimately, this work suggests that rupture of the 1952 Kern County, California earthquake initiated with a strike-slip dominant event (rake = 11±5°), on a shallow dipping branch (dip = 35±1°)of the White Wolf fault system (strike = 49±3°).

FIGURE 2.1 BERKELEY WILIP-GALITZIN SEISMIC RECORDING
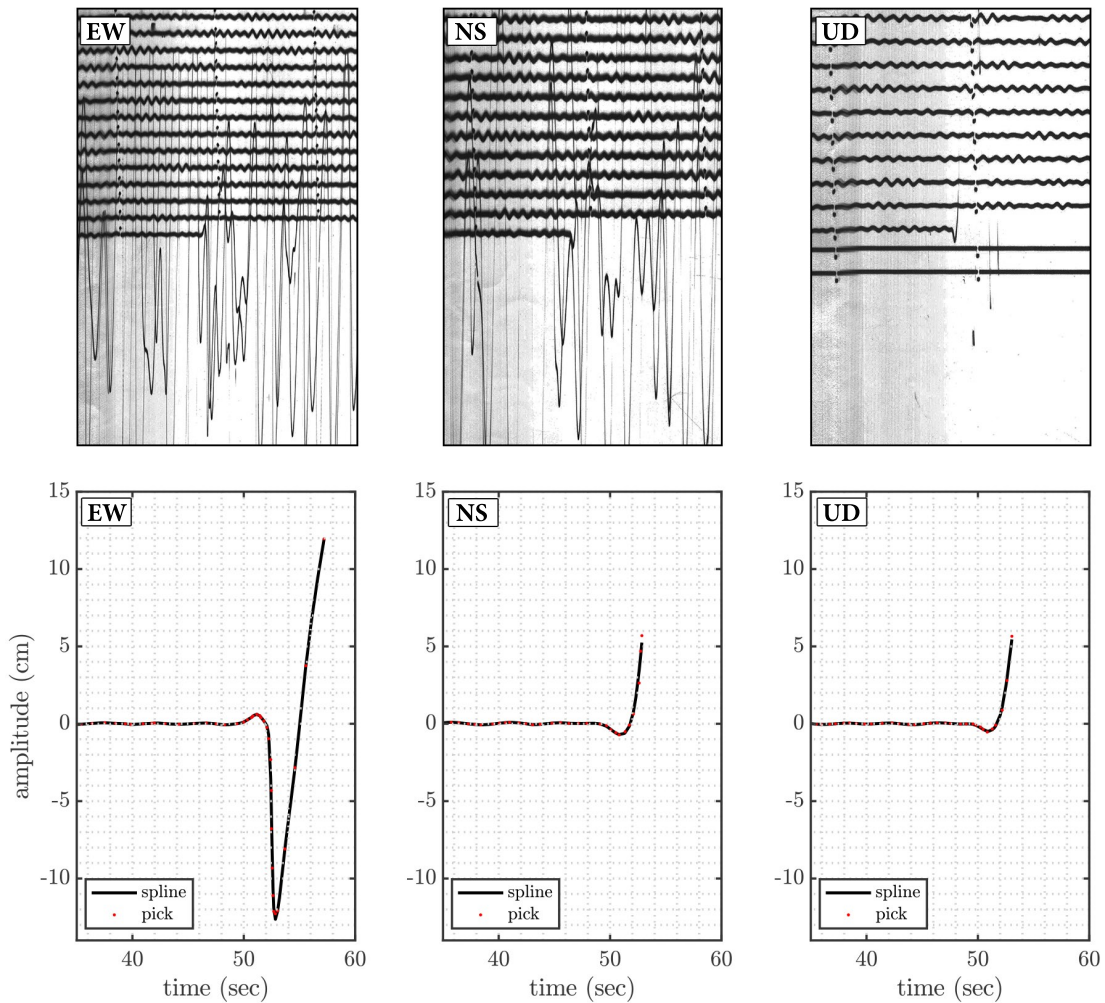
Figure 2.1: Wilip-Galitzin, 3-component) instrumental recording of the 1952 Kern County, California earthquake. The top three panels show digital scans of the original seismograms whereas the bottom three panels show digitized P-wave first-motions for additional clarity. Components include: east-west (EW), north-south (NS) and up-down (UD). Shortly after P-wave arrivals, the NS and UD components become saturated ($\sim$3 s). Luckily, the EW component retains the entire secondary motion.

FIGURE 2.2 GALITZIN SEISMIC INSTRUMENT
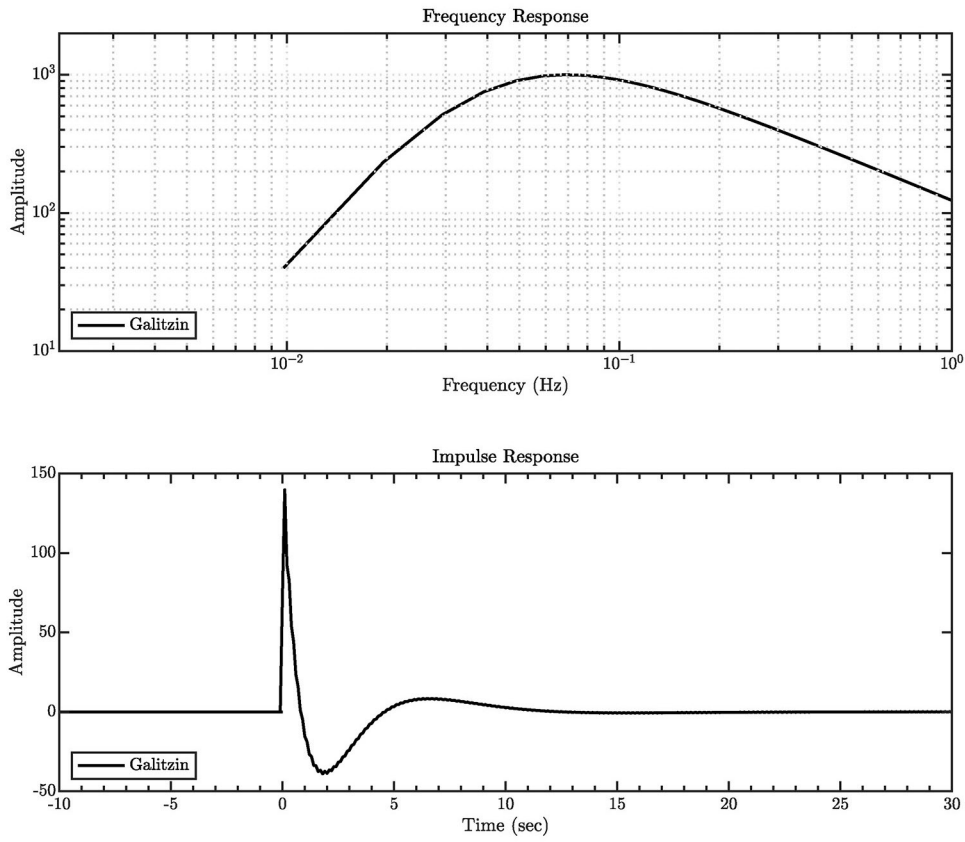
Figure 2.2: Synthetic response for the horizontal component of the Wilip-Galitzin seismic instrument. The instrument has a peak frequency response at 0.083 Hz or 12 s. Any impulsive signal recorded by this instrument will be followed by a characteristic, low-frequency tail with opposite polarity and smaller amplitude.

23

FIGURE 2.3 FIRST-MOTION POLARITY OBSERVATIONS
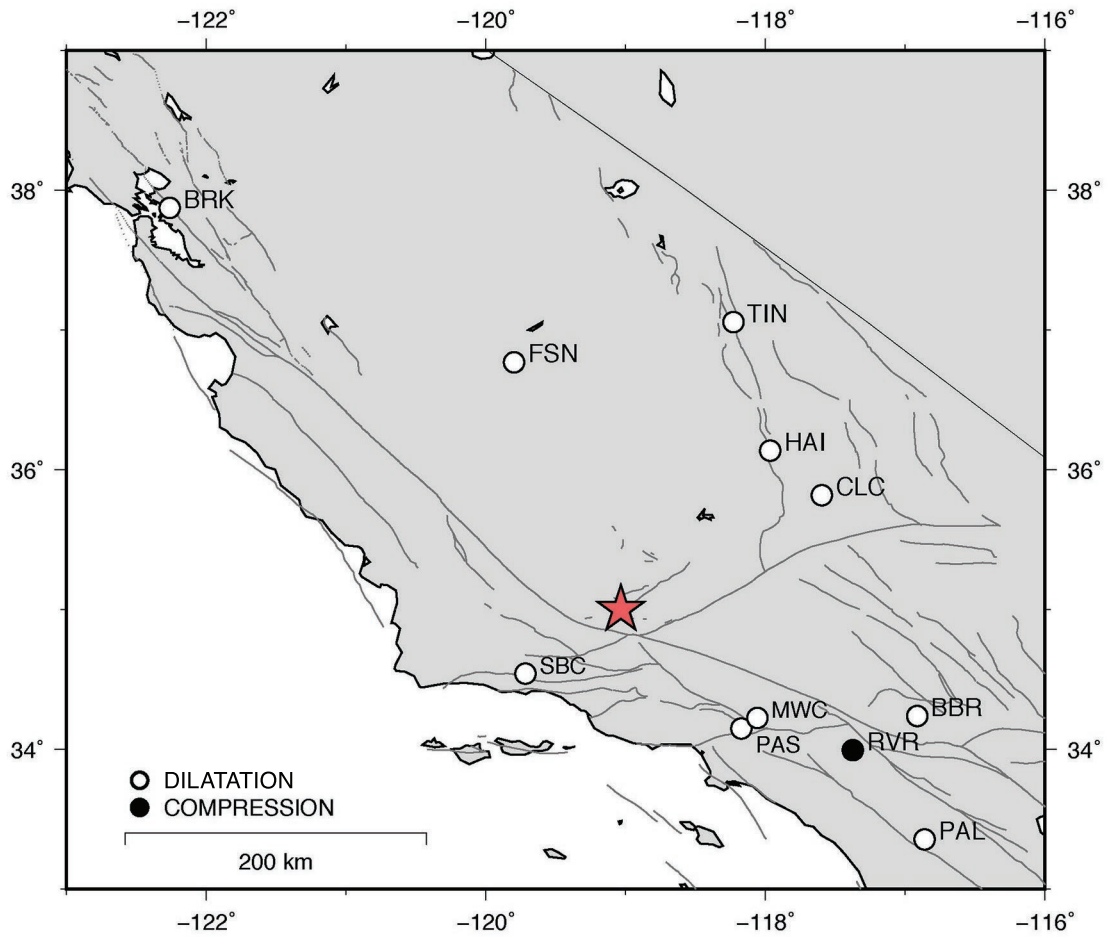
Figure 2.3: First-motions reported by *Gutenberg* [1955b], included in the HASH focal inversion. The red star represents the earthquake's epicenter. Negative (or dilatational) first-motions are represented by white, open circles. Positive (or compressional) first-motions are represented by black, filled circles. There are 11 observations in total, all of which are dilatations, with the exception of Riverside. Stations include: Berkeley (BRK), Fresno (FSN), Tinemaha (TIN), Haiwee (HAI), China Lake (CLC), Santa Barbara (SBC), Big Bear (BBR), Riverside (RVR), Palomar (PAL), Mount Wilson (MWC) and Pasadena (PAS).

Figure 2.4: Southern California 1D velocity structure proposed by *Kanamori and Hadley* [1975] (SOCAL). This 1D velocity structure represents an average for Southern California and is used in the calculation of P-wave first-motion take-off angles.

FIGURE 2.5 FIRST-MOTION FOCAL SOLUTIONS
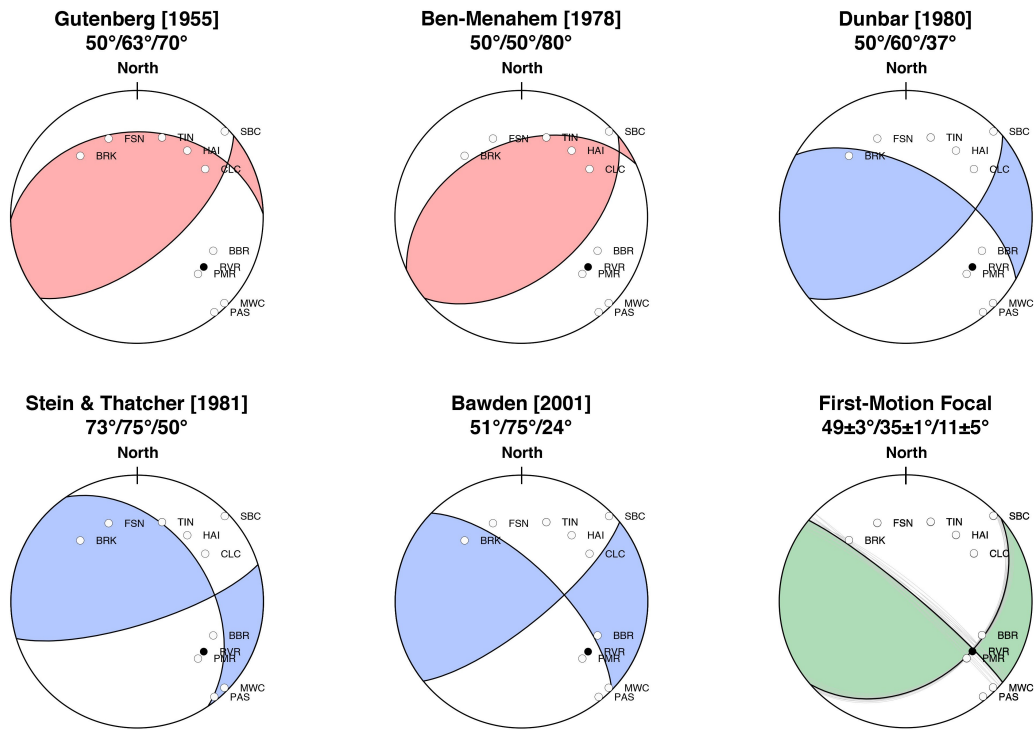
Figure 2.5: Comparison between published source mechanisms and *P*-wave first-motion observations. We use a source depth of 15 and location consistent with *Gutenberg* [1955c] (35°N, 119°W, 15±6 km). Seismic studies (in red) favor thrust dominant solutions. Geodetic studies (in blue) favor strike-slip dominant solutions. No published solutions can explain reported first-motions [*Gutenberg*, 1955b] and most importantly the polarity of Berkeley (BRK), Riverside (RVR) and Big Bear (BBR), simultaneously.

FIGURE 2.6 ZERO MISFIT

10 km
51±2°/36°/17±7°

15 km
49±3°/35±1°/11±5°
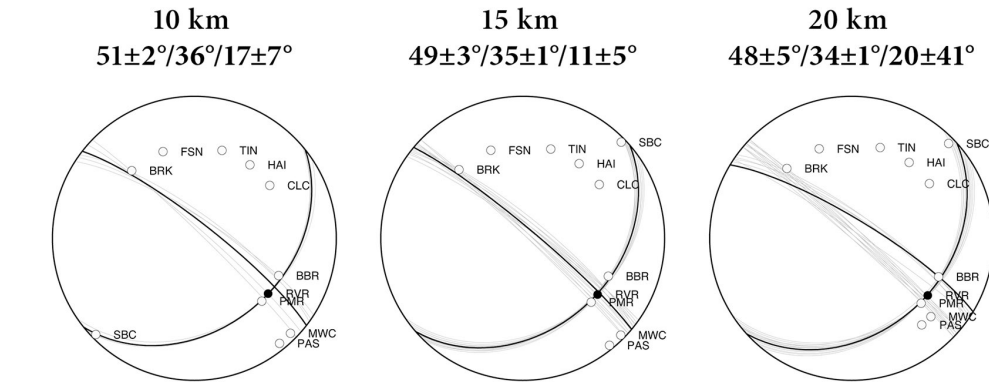
20 km
48±5°/34±1°/20±41°

15 km Solution Distributions
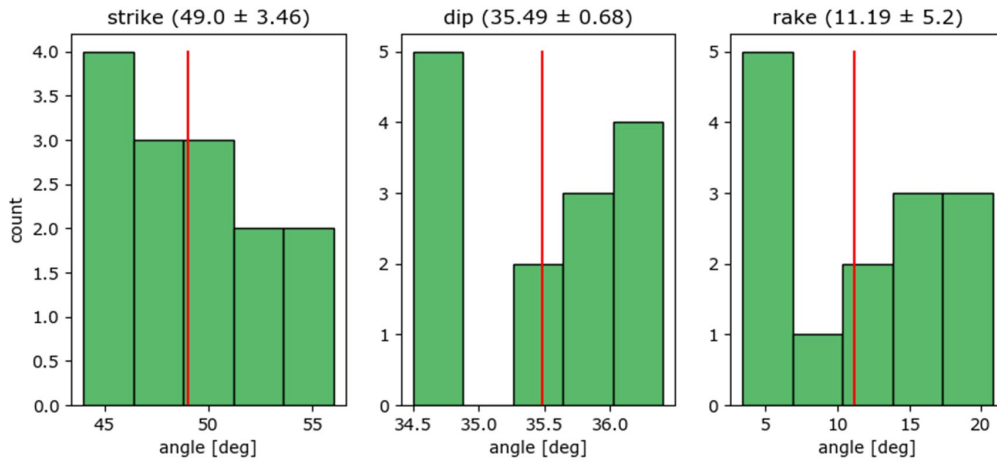
Figure 2.6: HASH inversion results with zero misfit and source depths of 10 km, 15 km and 20 km. Station azimuth and take-off angles are plotted atop focal spheres with acceptable solutions in grey and the mean solution in black. The mean solution along with one standard deviation is labeled below each source depth. All polarity observations are satisfied simultaneously and agree with the known strike of the White Wolf Fault (strike ≈ 50°). Histograms in green represent the spread of optimal solutions accepted by HASH. The red line in the histograms represents the mean solution.

27

FIGURE 2.7 PROBABILITY OF MIS-PICK, 9%

15 km
(25±39°/45±17°/43±20)

Solution Distributions
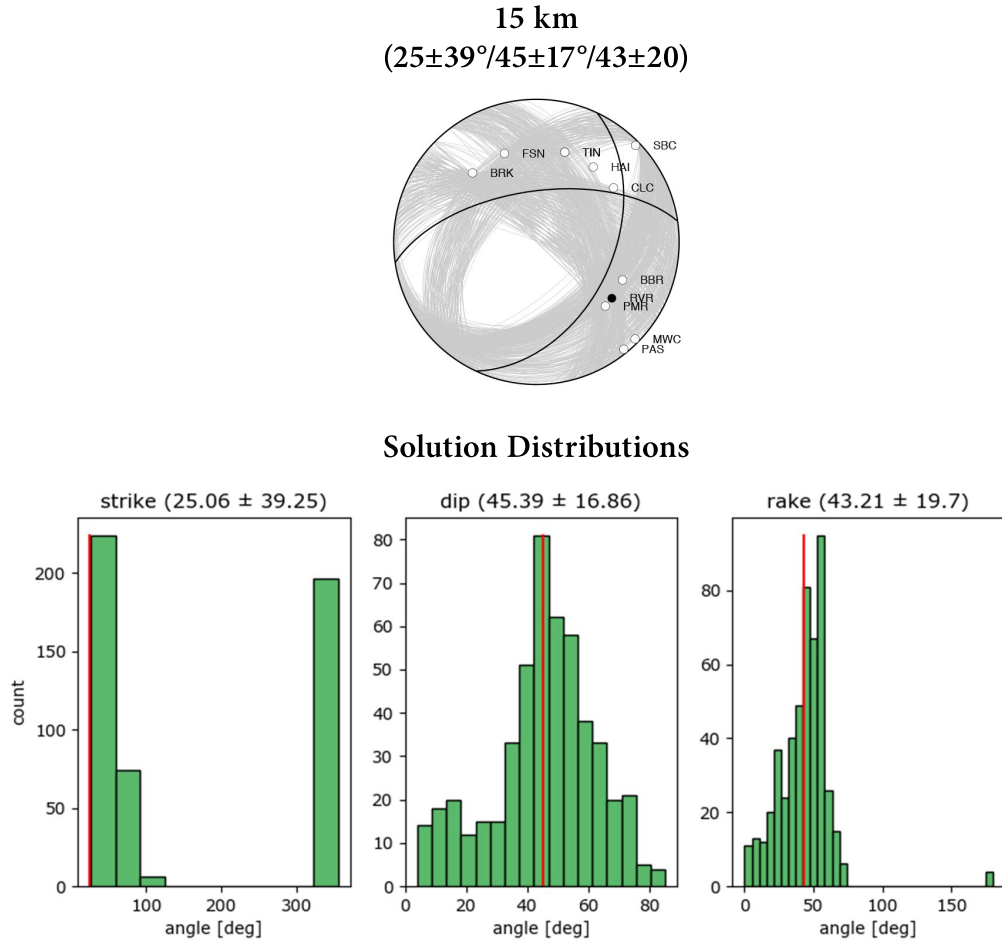
Figure 2.7: HASH returns 500 random solutions that satisfy at least 10, out of the 11, first-motion observations. Solutions have significant variability and do not appear to cluster around a preferred focal mechanism. Histograms in green represent the spread of solutions accepted by HASH. The red line in the histograms represents the mean solution. Strike mean and std are calculated assuming circular statistics.

Figure 2.8 HASH Fixed Strike 50±1°, Source Depth

10 km	15 km	20 km
50±1°/44±6°/37±13°	50±1°/41±11°/40±14°	50±1°/43±7°/40±16°
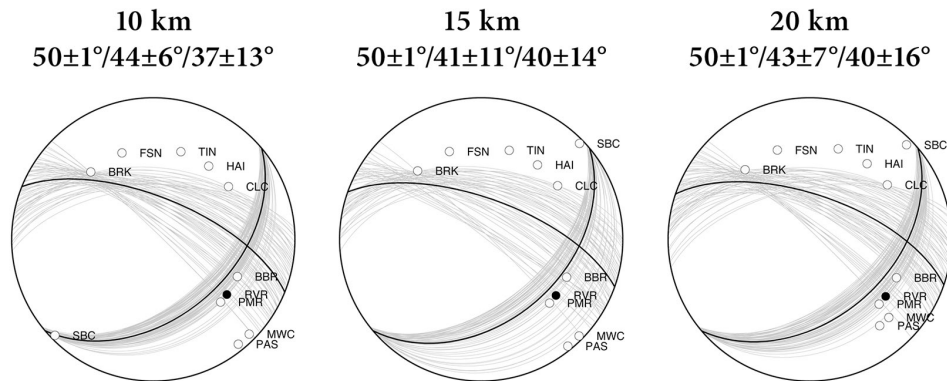
15 km Solution Distributions
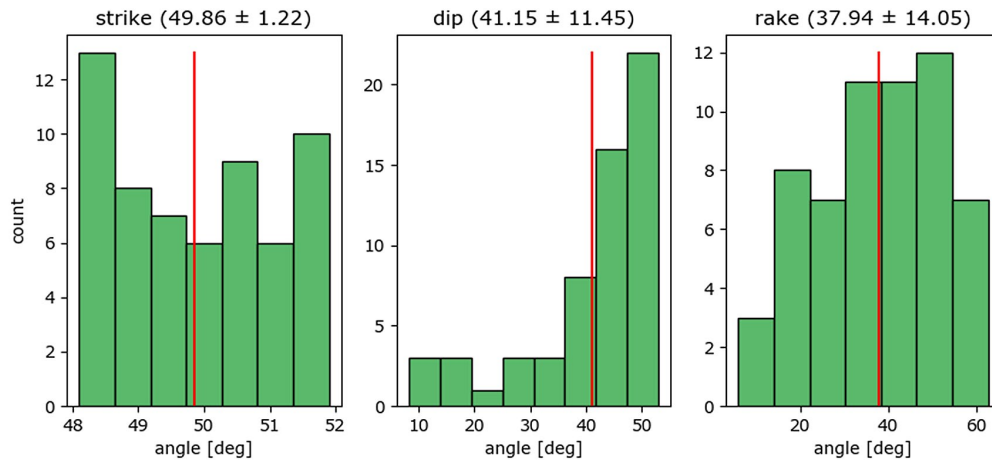
Figure 2.8: HASH inversion results that satisfy at least 10 first-motion observations and have a strike consistent with the White Wolf Fault (strike = 50±1°). Station azimuth and take-off angles are plotted atop focal spheres with acceptable solutions in grey and the mean solution in black. The mean solution along with one standard deviation is labeled below each source depth. There is general agreement among mean solutions but significant variability among the filtered sub-set. Mean solutions cannot satisfy observed polarities at RVR and BBR, simultaneously. Histograms in green represent the spread of solutions. The red line in the histograms represents the mean solution.

Chapter 3

Finite Fault Inversion

With the development of modern computational seismology, ground displacements can be synthetically calculated given a rectangular starting fault model. Since the pioneer work of *Trifunac* [1974], observed seismic waveforms and static deformations have been used either separately or jointly to constrain the rupture spatiotemporal evolutions of large earthquakes. In this chapter, we adapt a finite-fault inversion to establish a slip history of the 1952 Kern County, California, earthquake using strong-motion seismic records [*Kanamori and Jennings*, 1978] and reported triangulation and leveling observations [*Bawden*, 2001].

3.1   Observations

3.1.1   Strong-Motion Seismic Recordings

Local seismic data used in the joint inversion consists of strong motion seismic recordings from the following five strong motion stations: Caltech Athenaeum (CITA), Caltech (CITL), Hollywood Storage Basement (HWSB), Santa Barbara City Hall (SBCH) and Taft (TAFT). All seismic recordings, shown in Figure 3.2, were recorded on analog instruments and have since been digitized and processed for our analysis. The seismograph at Caltech Athenaeum (CITA) is a specially designed low-gain Wood-Anderson instrument with two horizontal displacement components. All other stations, which have standard 3-component strong motion sensors, are integrated into units of velocity for our purposes. We further filtered our original recordings from 0.08 to 0.5 Hz, to reduce the impact of long period observational noise and unmodeled 3D propagation effects.

The 0.5 Hz lowpass filter comes from MATLAB's built-in `FIRPM()` function. This function uses the Parks-McClellan algorithm to design an optimal filter based on an idealized input [*Rabiner et al.*, 1975] (Figure 3.3). We chose a simple lowpass filter with a corner frequency of 0.5 Hz and an order of 128 to produce an optimized lowpass filter with minimal spectral leakage. To avoid any unwanted phase shifts we apply this filter using the non-causal command, `filtfilt()`. To validate the filter, we utilize the filtered spike method [*Gubbins*, 2004] to see the effects across all frequencies. As expected, the impulse is spread across lower frequencies and has a smaller maximum amplitude (Figure 3.3). Lastly, this filter is applied to the original strong-motion seismic recordings, which will be used in the finite-fault inversion (Figure 3.4).

Unfortunately, due to the nature of these seismic instruments, all recordings were triggered. As a result, we are not able to align the data with their P-wave first-motions. This greatly reduces the effectiveness of these recordings as constraints within our joint

inversion. None the less, these records do however, contain the very important S-wave pulse. Before each inversion, we calculate synthetic seismograms using a source at the hypocenter and align its impulse with the observed S-waves. Afterwards, we run each inversion without changing the alignment further.

3.1.2   Triangulation and Leveling Observations

We use the geodetic data selected by *Bawden* [2001], which consists of 142 triangulation angle-changes and 33 elevation-changes. All measurements and their accompanying standard errors are provided in Tables B.6–B.9 and correspond to the geodetic network depicted in Figure 3.5.

Geodetic surveys were conducted from 1926–1972 and record static surfaces changes that resulted from the 1952 Kern County, California earthquake. Careful consideration must be made, however, to isolate the effects of pre-, co- and post-seismic deformations, as well as any alternative sources of displacements or subsidence. *Bawden* [2001] examined these effects in detail and only includes triangulation angle changes from 1951–1953, bracketing the main rupture sequence by a year before, and after the earthquake. Leveling measurements, on the other hand, were taken in 1926, 1947 and again in 1953. Thus, these measurements reflect changes corresponding to greater periods of time as compared with the triangulation measurements. Despite this, *Bawden* [2001] is confident that the leveling data he used contains little contamination associated with non-tectonic processes.

Data uncertainties attributed to this geodetic network (Figure 3.5) are quantified through the assessment of triangulation mis-closures and measurement standard errors [*Bawden*, 2001]. The final observational error for each triangulation angle-change is 1.18 arc s [*Bawden*, 2001]. For each leveling elevation-change, error is defined as $\alpha\sqrt{L}$, where α is 2 mm and L is the distance between subsequent measurements in km [*Bawden*, 2001].

Following *Bawden* [2001], we constrain slip by directly modeling angle- and leveling-changes rather than using reconstructed absolute coseismic displacements at the surface. Using this approach, the observational error associated with each measurement becomes much easier to manage. To verify our forward geodetic model, we used Bawden's fault geometry and half-space velocity structure to predict triangulation and leveling observations. We obtain a similar degree of misfits as compared to [*Bawden*, 2001].

From the distribution of geodetic measurements, *Bawden* [2001] argued that strike-slip motions are best resolved in the center of his fault model whereas dip-slip motions are best resolved along the edges. As mentioned in a chapter one, this is because, leveling lines are valuable for assessing the degree of dip-slip and the triangulation network is valuable for assessing the degree of strike-slip. Leveling lines are absent in the middle of the geodetic network (Figure 3.5) and therefore this region has large uncertainties associated with dip-slip motions. Luckily, however, seismic constraints complement these geodetic displacements. Together, both data sets provide important information as to the timing, magnitude, location and orientation of earthquake sub-events in our joint inversion.

3.1.3   Velocity Models

Unlike our first-motion study, we use five different 1D velocity profiles within our joint inversion. Velocity structures are made by interpolating along 2D cross-sections of the 3D SCEC CVM-S4.26 [*Lee et al.*, 2014; *Small et al.*, 2017]. As seen in Figure 3.6, the velocities within the vicinity of the White Wolf fault (KERN) and outside (CITA, HWSB, SBCH and TAFT) vary significantly from the average 1D structure proposed by *Kanamori and Hadley* [1975] (SOCAL). Tabulated values corresponding to each of these five velocity model can be found in Tabels B.1–B.5 in Appendix B.

3.2   Inversion Method

The finite-fault inversion employed in this study, as described in *Ji et al.* [2002a], begins with the preliminary analysis of geophysical observations. Previous works, as discussed in chapter one, lay the foundation through which this joint analysis is made possible. They establish fundamental source characteristics, such as magnitude, and provide insight into the earthquake's complex rupture behavior. Paired alongside a detailed understanding of the region's velocity structure, this information allows us to model the spatiotemporal evolution of the 1952 Kern County, California earthquake.

We begin by constructing a starting fault model comprised of two, right stepping fault planes [*Bawden*, 2001]. We then further discretize these planes into a regular grid of sub-faults. Each sub-fault is a finite, 2D plane with five additional model parameters: slip amplitude, rake-angle, rupture velocity, rupture initiation time and rise time. Together these model parameters allow us to describe how much and where slip accumulates, the type and degree of faulting, as well as the onset and duration of the rupture at specific points on the fault surface. Throughout the inversion, we perturb these parameters until we find a slip model that is consistent with our seismic and geodetic data.

3.2.1   Source Representation

The response of a finite-fault rupture can be calculated by summing the contributions of a regular grid work of sub-faults [*Heaton and Helmberger*, 1979]:

$$u(\mathbf{x}, t) = \sum_{j=1}^{n} \sum_{k=1}^{n} \mathrm{D}_{jk} \left[\cos\left(\lambda_{jk}\right) Y_{jk}^{1}\left(V_{jk}, \mathbf{x}, t\right) + \sin\left(\lambda_{jk}\right) Y_{jk}^{2}\left(V_{jk}, \mathbf{x}, t\right) \right] * \dot{S}_{jk}(t). \quad (3.1)$$

Here, $u(\mathbf{x}, t)$ is the synthetic displacement at an arbitrary location $\mathbf{x}$. D_{jk}, λ_{jk}, and $S_{jk}(t)$ are the slip amplitude, rake angle, the rise time function, respectively. jk

is the jth element along strike and k^{th} element down dip. V_{jk} represents the average rupture velocity from the hypocenter to sub-fault jk. Lastly, $Y_{jk}^{m}(V_{jk}, \mathbf{x}, t)$ is the sub-fault's Green's function and represents the static and dynamic response for unit strike-slip (m=1) and dip-slip motions (m=2) on sub-fault jk. Thus, given a set of source model parameters (i.e., D_{jk}, λ_{jk}, V_{jk} and $S_{jk}(t)$) and an appropriate velocity structure, we can synthesize static and dynamic changes at any arbitrary location [*Ji et al.*, 2002a]. The advantage of representing the source in this way is that we can use Equation 3.1 to calculate synthetic static displacements in addition to seismic waveforms.

3.2.2   Objective Functions

Each slip model is validated through the forward prediction of synthetic data. In order to quantify how well the synthetic data predicts observations, we must define several objective functions [*Ji et al.*, 2002a]. For seismic data, the comparison between synthetic and observed seismograms are made in the wavelet domain. Both observed and synthetic seismograms are transformed into a summation of wavelets, each with a specific scale and position [*Mallat*, 1999; *Yamada and Ohkitani*, 1991]. For geodetic data, we must first calculate static displacements at each station, then subsequently calculate relative angle and elevation changes.

Seismic Waveforms

Using a pair of objective functions we can quantify the seismic waveform misfit [*Lian-She Zhao and Helmberger*, 1994]. For long-period signals we use the L1 and L2 norms:

$$e_l = \sum_{j=j_{min}}^{j_c} W_j \left(\frac{1}{k_j} \sum^{k_j} |o_{j,k} - y_{j,k}| + \sqrt{\frac{1}{k_j} \sum^{k_j} (o_{j,k} - y_{j,k})^2} \right). \tag{3.2}$$

Here, $o_{j,k}$ represents observed wavelet coefficients and $y_{j,k}$ represents synthetic wavelet coefficients. j is the index of scale and k is the index of position. Lastly, W_j is a weighting matrix used to separate long period signals from shorter ones. The final resulting error is termed e_l for longer periods. For short period signals we use:

$$e_{\mathrm{h}} = \sum_{j_c+1}^{j_{\max}} W_j \left(1.0 - \frac{2 \sum^{k_j} o_{j,k} y_{j,k}}{\sum^{k_j} o_{j,k}^2 + \sum^{k_j} y_{j,k}^2} \right). \tag{3.3}$$

Originally proposed by *Sen and Stoffa* [1990], this function is optimized for signal shape rather than amplitude and works well for higher-frequency seismic signals [*Ji et al.*, 2002a]. The combined waveform objective function is simply the addition of the short- and long-period terms:

$$E_{wf} = e_l + e_h. \tag{3.4}$$

From this expression, we can easily evaluate a slip model's performance in matching observed seismograms [*Ji et al.*, 2002a].

Geodetic Objective Functions

With the known observational standard deviation, we define the geodetic error functions as:

$$\mathrm{E_{st}} = \sum_i^N \left(\frac{S_{\mathrm{o}}^i - S_{\mathrm{s}}^i}{\sigma_i} \right)^2. \tag{3.5}$$

Here, S_{o}^i and S_{s}^i are the observed and synthetic leveling or triangulation-angle changes. The σ_i denotes the standard deviation with respect to the ith measurement. N is the total number of measurements. After each iteration of the inversion procedure we are left with two χ^2 values, one corresponding to triangulation measurements and another to leveling observations.

Combined Objective Functions

With seismic and geodetic objective functions defined, the last step is to combine objective functions into a single expression [*Ji et al.*, 2002a]:

$$E_{tot}(m) = E_{wf} + \lambda_1 E_{st} + \lambda_2 E_{moment} + \lambda_3 E_{time} + \lambda_4 E_{smooth} \qquad (3.6)$$

This error function includes a term for waveform-fit (E_{wf}), a term for geodetic-fit (E_{st}), constraints to the seismic moment (E_{moment}) and finally a smoothing constraint to the rupture propagation through time (E_{time}) and space (E_{smooth}). These additional constraints act to stabilize the inversion, which is highly non-unique [*Hartzell et al.*, 1996]. The importance of each of these terms is mediated through weighting coefficients λ_{1-4}, where: $\lambda_1 = 1$, $\lambda_2 = 0.0001$, $\lambda_3 = 0.4$ and $\lambda_4 = 0.4$. These values were selected to emphasize the importance of our seismic and geodetic constraints followed by the rupture smoothness through time and space.

3.2.3   Inversion Strategy

The joint, finite fault inversion uses a simulated annealing, heat-bath algorithm [*Rothman*, 1985, 1986] to search model space for a set of parameters that satisfy our combined error function. This strategy has the advantage of simultaneously perturbing parameters with each iteration of the inversion while avoiding local minimum in error space.

Let's assume that the source model has M parameters. During each iteration of the heat-bath algorithm, our code loops through all M parameters and calculates the probability of selecting new values. If there are N possible values for any one arbitrary parameter m^k, the probability of picking the ith value (i.e., $m^k = m_i^k$) is defined as:

$$P_i = \exp\left(-E(m_i^k)/kT\right) / \left(\sum_i^N \exp\left(-E(m_i^k)/kT\right)\right). \tag{3.7}$$

Here, $E(m)$ is the error function defined above. k and T denote the Boltzmann constant and temperature, respectively. After calculating the probability (P_i), a random number $0 < R < 1$ is generated to decide which value will be selected. We select the jth model value for this parameter (i.e., $m^k = m_j^k$) if:

$$\sum_{i=1}^{j-1} P_i < R < \sum_{i=1}^{j} P_i \tag{3.8}$$

The same procedure is repeated for the next parameter (m^{k+1}) until all M parameters have been perturbed. After, the inversion saves the current set of parameters, decreases the temperature of the inversion by αT ($\alpha = 0.985$) and starts again. The inversion will end either when the change in error ($E(m)$) becomes negligible or when the total number of iterations reaches a pre-determined maximum (max $= 600$).

Note that model parameter perturbations are mediated through the inversion temperature (T). The relative probability difference of two model values, for example, m_i^k and m_{i+1}^k, is:

$$\exp\left(-\Delta E/kT\right) \tag{3.9}$$

where,

$$\Delta E = E(m_i^k) - E(m_{i+1}^k) \tag{3.10}$$

Therefore, if we assume $\Delta E > 0$ (i.e., m_{i+1}^k is the better solution). When T is high, the $\exp\left(-\Delta E/kT\right) \approx 1$, and the two model values (m_i^k and m_{i+1}^k) have similar probabilities of being selected. When T is low, $\exp\left(-\Delta E/kT\right) \approx 0$ and m_{i+1}^k has much larger chance of being selected over m_i^k.

3.3   Inversion Results

We have performed numerous tests and found that fault geometry plays an important role in determining the final slip model. For this reason, we have adopted the fault geometry proposed by *Bawden* [2001] and used it as the starting model (Model 1) to run our inversion. According to the subsequent results, we made incremental changes to fault geometry. Here, we present and discuss four of these models. General information regarding these models can be found in Table 3.1 below.

TABLE 3.1 FOUR SLIP MODELS

Model	SWF	NEF	SD (km)	E_{tot}	E_{wf}	χ^2_{tri}	chi^2_{lvl}	SW_{rake}	NE_{rake}	M_W
1	10×7	8×4	16.5	1.18	0.53	1.85	4.46	57°	50°	7.28
2	12×7	10×4	16.5	1.12	0.52	1.66	4.06	57°	32°	7.30
2	12×7	10×4	9.5	1.14	0.55	1.60	3.79	47°	46°	7.21
4	12×6	10×4	9.5	1.18	0.58	1.64	3.80	50°	41°	7.18

Table 3.1: General information regarding Models 1–4. Here, SWF is the dimensions of the southwest fault plane in terms of sub-fault segments (3×3 km each). NEF is the northeast fault plane. SD is source depth in units of km. E_{tot} is the combined error. E_{wf} is the waveform-fit. χ^2_{tri} and chi^2_{lvl} are triangulation and leveling errors, respectively. SW_{rake} and NE_{rake} are the weighted rake angles over respective faults. M_W is the cumulative moment magnitude.

3.3.1   Model 1

Model 1 uses the fault geometry determined by *Bawden* [2001] (summarized in Table 3.3.1), which consists of two, right stepping fault planes. They are termed "right step-ping" because there is a small separation between fault planes. Both of the fault planes strike N51°E and dip 75° to the southeast. For the purposes of performing our joint inversion, we further discretized these fault planes into 3 km by 3 km sub-faults. The

dimensions of the southwest fault plane (SWF) are 30 km along strike and 21 km down dip (10 sub-faults by 7 sub-faults, respectively). The SWF also extends from a depth of 6 km down to 27 km below earth's surface. The geodetic study by *Bawden* [2001] does not include an earthquake hypocenter. Therefore, we assign a hypocenter (34.992°N, -119.015°; depth = 16.5 km) to the middle of the 3rd sub-fault along strike and 4th sub-fault down dip (SWF). The dimensions of the northeast fault plane (NEF) are 24 km along strike and 12 km down dip (8 sub-faults by 4 sub-faults, respectively). The NEF also extends from a depth of 1km down to 6 km below earth's surface. The fault geometry is positioned such that the SWF extends from Wheeler Ridge to Comanche Point. The NEF continues northeast towards the Scodie seismic lineament [*Bawden*, 2001].

Figures 3.7–3.9 show the inverted slip, velocity, rise time, and the cumulative moment rate function for Model 1. The corresponding fit to strong motion waveforms and geodetic data are presented in Figures 3.10 and 3.11. Model 1 can fit the long-period CITL records relatively well, however, the fit to the remaining strong motion waveforms is considerably worse. Geodetic fit has improved significantly with respect to errors in *Bawden* [2001], however, there seems to be several anomalous measurements that cannot be explained by our model. Total error (E_{tot}) for Model 1 is 1.18. Waveform error (E_{wf}) is 0.53. Triangulation and leveling errors (χ^2_{tri} and χ^2_{lvl}) are 1.85 and 4.46, respectively.

Model 1 contains four major regions of slip (Figure 3.7), there are two relatively large regions within the SWF and two smaller regions in NEF. According to Figure 3.8, these regions are also associated with high rupture velocities. The slip area located near the hypocenter has a relatively short rise time (Figure 3.8). Generally, slip within the SWF is confined to depths greater than 10 km. The weighted average rake [*Ji et al.*, 2002b] over the SWF is 57°and over the NEF is 38°. According to Figure 3.9, 95% of the rupture occurred within the first 23.4 s. The cumulative moment of this rupture is 1.08×10^{20} Nm, or M_W 7.28.

Table 3.3.1 Starting Fault Geometry [*Bawden*, 2001]

Parameter	Southwest	Northeast
Strike °	51	51
Dip °	75	75
Length, *km*	29.7	23.6
Upper depth, *km*	6	1
Lower depth, *km*	27	12.5
Latitude, Northern endpoint of fault	35.132	35.265
Longitude, Northern endpoint of fault	-118.840	-118.636
Latitude, Southern endpoint of fault	34.970	35.132
Longitude, Southern endpoint of fault	-119.100	-118.840

3.3.2   Model 2, Along Strike Extension

As both the SWF and NEF of Model 1 have high slip areas near their northeast edge, we extend both fault segments by 6 km in the northeast direction (Figure 3.12). As a result, we see a significant improvement fitting triangulation observations (Figure 3.16). Total error (E_{tot}) is reduced to 1.12. Waveform error (E_{wf}) is 0.52. Triangulation and leveling errors (χ^2_{tri} and χ^2_{lvl}) are 1.66 (10% reduction) and 4.06, respectively.

While Model 2 consists of 124 sub-faults, the general distribution of slip does not change significantly. The only notable difference between the two models is the weighted average rake over the NEF (32°). According to Figure 3.14, 95% of the rupture occurred within the first 25 s, which is a slight increase compared to Model 1. The cumulative seismic moment is 1.13×10^{20} Nm, or M_W 7.30.

3.3.3   Model 3, Source Depth 9.5 km

Model 1 and 2 have large areas of slip at depths greater than 20 km. To explore whether this pattern is correlated with the pre-assigned source depth of 16.5 km (35°N, 119°W; depth = 15±6 km) [*Gutenberg*, 1955c], we incrementally raise the source depth up two 6 km. The model with hypocenter depth of 9.5 km fits the geodetic data the best and is presented here as Model 3. Following this decrease in source depth, the SWF plane moves upward, and we assign the hypocenter to the middle of the 3rd sub-fault along strike and 3rd sub-fault down dip (SWF). These changes further improve the fits to both triangulation and leveling changes with errors of 1.60 and 3.79, respectively. Waveform error (E_{wf}) however, becomes slightly worse, with a value of 0.55. The resulting total error (E_{tot}) is also slightly worse at 1.14.

Despite the changes made to source depth, the general slip distribution within the SWF is similar. The NEF however, is significantly different. We do not see the same distribution of slip as compared with Models 1 and 2. The third major slip area along strike, has significantly smaller peak displacement. Additionally, the NEF has a high rupture velocity (approximately 10 km/s) as indicated by the contours, which are spaced every two s (Figure 3.17). We also note a considerable change to rake angles. The weighted average rake over the SWF is 47°and over the NEF is 46°. According to Figure 3.14, 95% of the rupture occurred within the first 25.9 s and the cumulative seismic moment is 8.62×10^{19} Nm, or M_W 7.21.

3.3.4   Model 4, Reduced Down-dip Extension

Model 3 still has significant strike-slip motion within the SWF at depths exceeding 20 km. This is inconsistent with the general rake of the shallower ruptures. To evaluate whether this is required by the data, we reduce down-dip extension further by changing

the dimensions of the SWF. The SWF is now 36 km by 18 km (10 sub-faults by 6 sub-faults, respectively) and extends from a depth of 2 km to 20 km below earth's surface. The total number of sub-faults is reduced to 112.

We find that the fits to the geodetic data is similar, with $\chi^2_{tri} = 1.64$ and $\chi^2_{lvl} = 3.08$, however, the fit to seismic data is worse, with $E_{wf} = 0.58$. As expected, the inverted cumulative seismic moment is reduced to 7.61×10^{19} Nm, or M_W 7.18. The total rupture duration is 24.6 s (Figure 3.24). We no longer see a high rupture velocity within the NEF. The weighted average rake angle over the SWF changes to 50°and the weighted average rake angle over NEF changes to 41°.

3.4   Summary

The four slip models presented above demonstrate the multitude of possible scenarios that can fit the seismic and geodetic observations. While Model 2 fits the data the best, Model 4 is more consistent with what we know about seismicity in southern California. Below, we summarize the common features shared by these models:

1. All seismic moments are similar but the seismic moment of 7.84×10^{19} Nm, or M_W 7.18 is preferred.

2. The rupture duration, defined as 95% of seismic moment, is about 23-26 s. However, most of the slip (>85%) occurs in first 20 s.

3. The rupture propagates slowly with speed approximately 1.5 km/s, less than 50% of shear wave speed in the source region.

4. There are two large asperities centered at 0 km and 18-21 km along strike within SWF, and two relatively smaller asperities centering at 30 km and 46 km along

strike within the NEF. We refer these as asperities A, B, C and D, respectively along the strike.

5. About three-fourths of the total seismic moment occurs within the SWF, which has a weighted average rake angle of 47°–57°. The remainder occurs within the NEF, which has a weighted average rake of 32°– 50°.

6. The centroid times of the first two asperities are well constrained. As indicated by consistent moment rate functions among different slip models. Ruptures within the NEF, on the other hand, are not as well constrained.

7. Although, the down-dip extension is poorly constrained, the centroid depth of asperity A (15-17 km) is independent of our choice of source depth (consistent throughout all models).

FIGURE 3.1 LOCAL STRONG-MOTION SEISMIC STATIONS
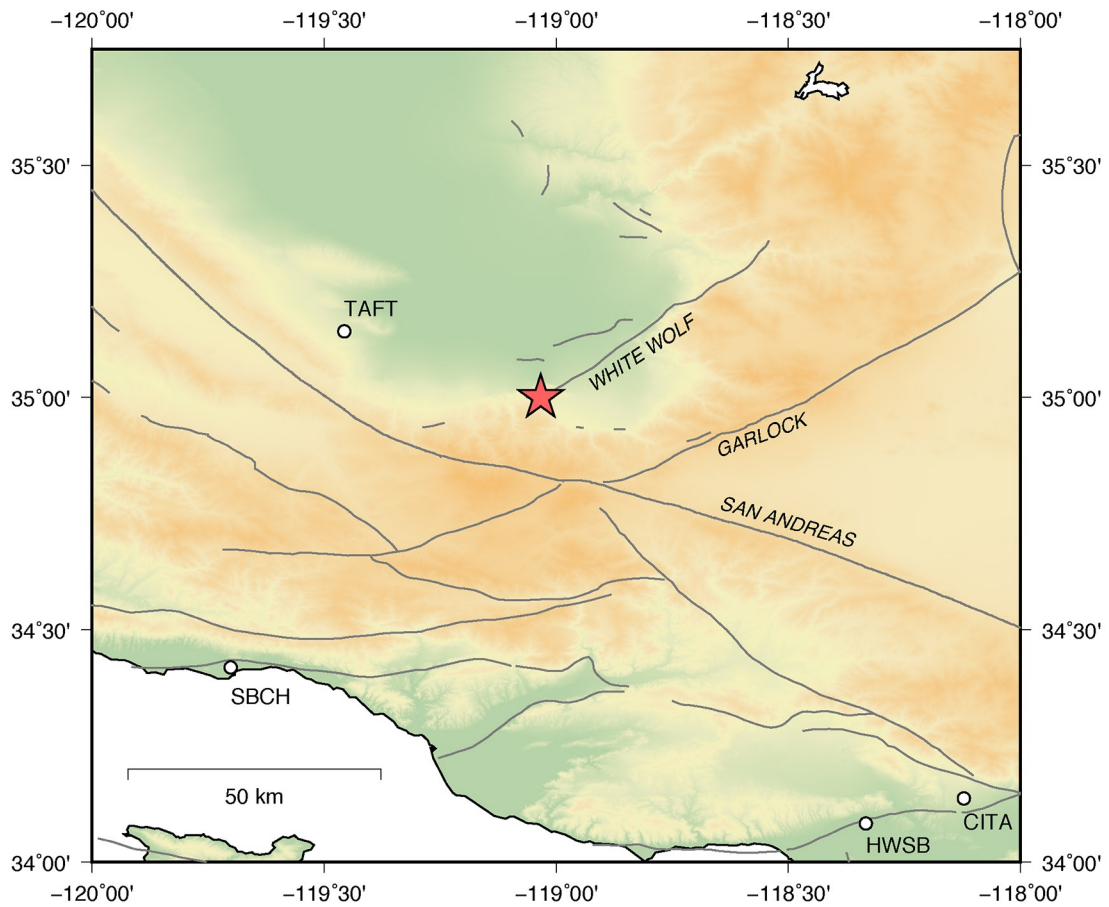
Figure 3.1: Regional map of Kern County and surrounding strong-motion seismic stations. Faults are outlined in grey and the 1952 Kern County epicenter is represented as a red star. Stations include: Caltech, Athenaeum (CITA & CITL); Hollywood Storage Basement (HWSB); Santa Barbara City Hall (SBCH) and Taft (TAFT)

FIGURE 3.2 UNFILTERED STRONG-MOTION SEISMIC RECORDINGS
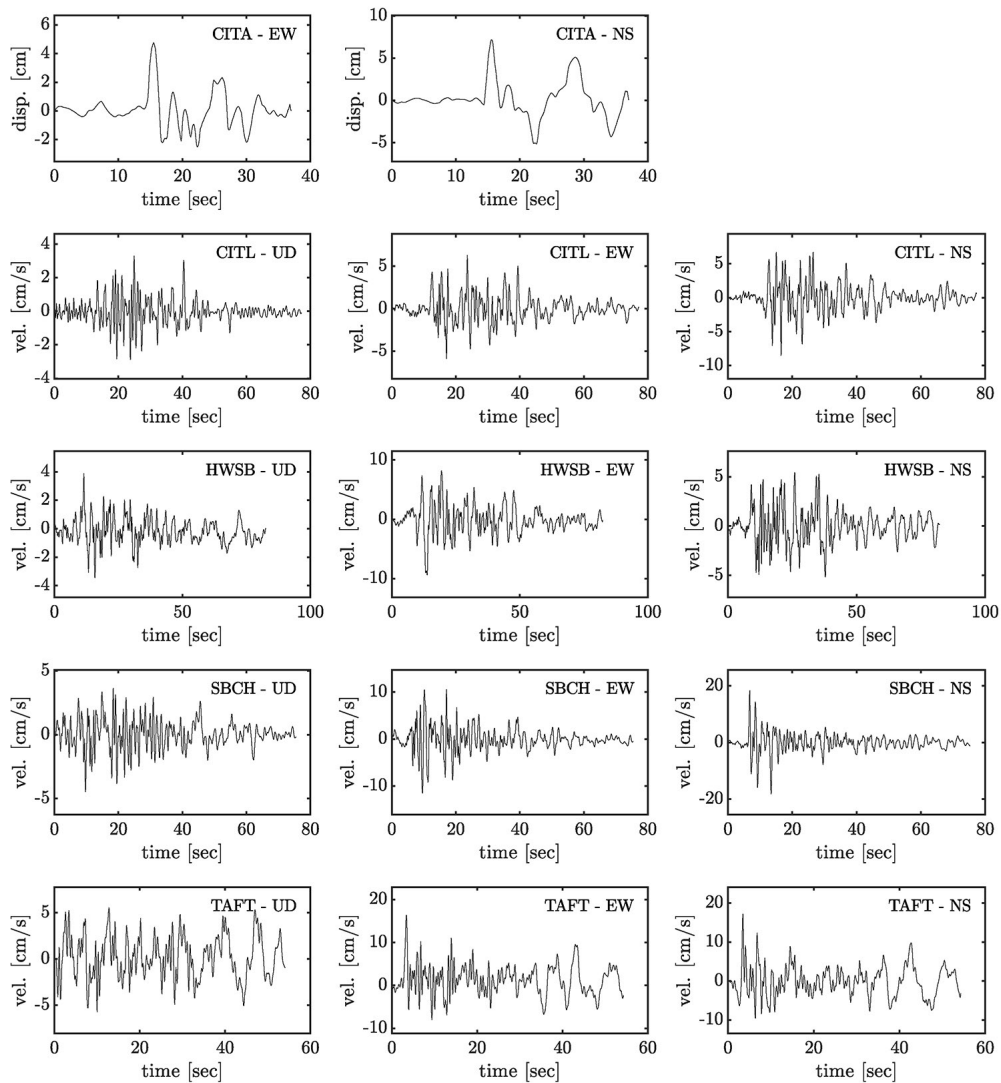
Figure 3.2: Digitized, analog strong-motion seismic recordings of the 1952 Kern County earthquake. All recording are in an up-down (UD), north-south (NS), east--west (EW) coordinate system. All recordings are in units of velocity, with the exception of the CITA records which are in units of displacement, and are filtered from 0.08–2.5Hz. We note that these instrumental recordings are missing initial P-wave arrivals but contain the important S-wave pulse. Stations include: Caltech, Athenaeum (CITA & CITL); Hollywood Storage Basement (HWSB); Santa Barbara City Hall (SBCH) and Taft (TAFT).

46

FIGURE 3.3 LOWPASS FILTER, FIRPM() AND SPIKE METHOD
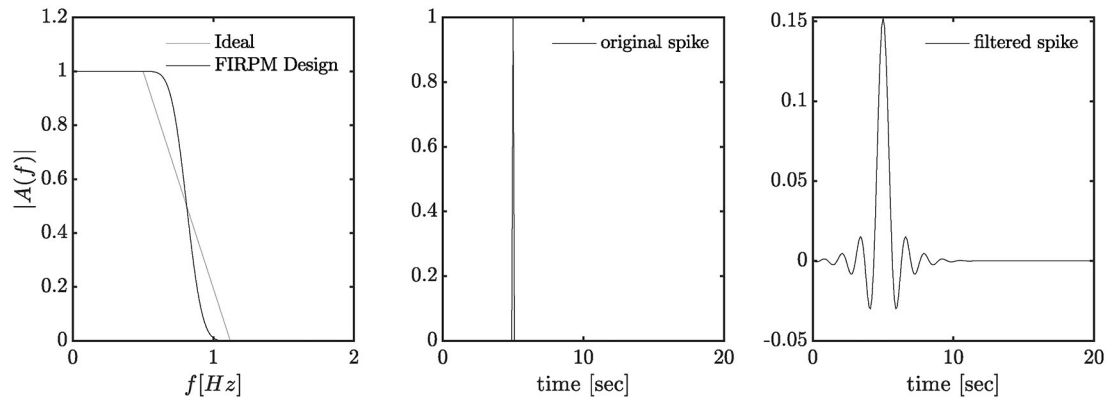
Figure 3.3: The first panel shows the input (light-grey) and output (black) of MATLAB's FIRPM() function. The FIRPM() function is used to create a filter that is as close to ideal as possible without producing artifacts in either the time-series or frequency response. The next two panels show the results of filtering an impulse, or spike, with original amplitude equal to 1. As expected the filtered pulse exhibits low frequency oscillations in the frequency range 0.08–0.5Hz.

FIGURE 3.4 FILTERED STRONG-MOTION RECORDINGS 0.08–0.5Hz
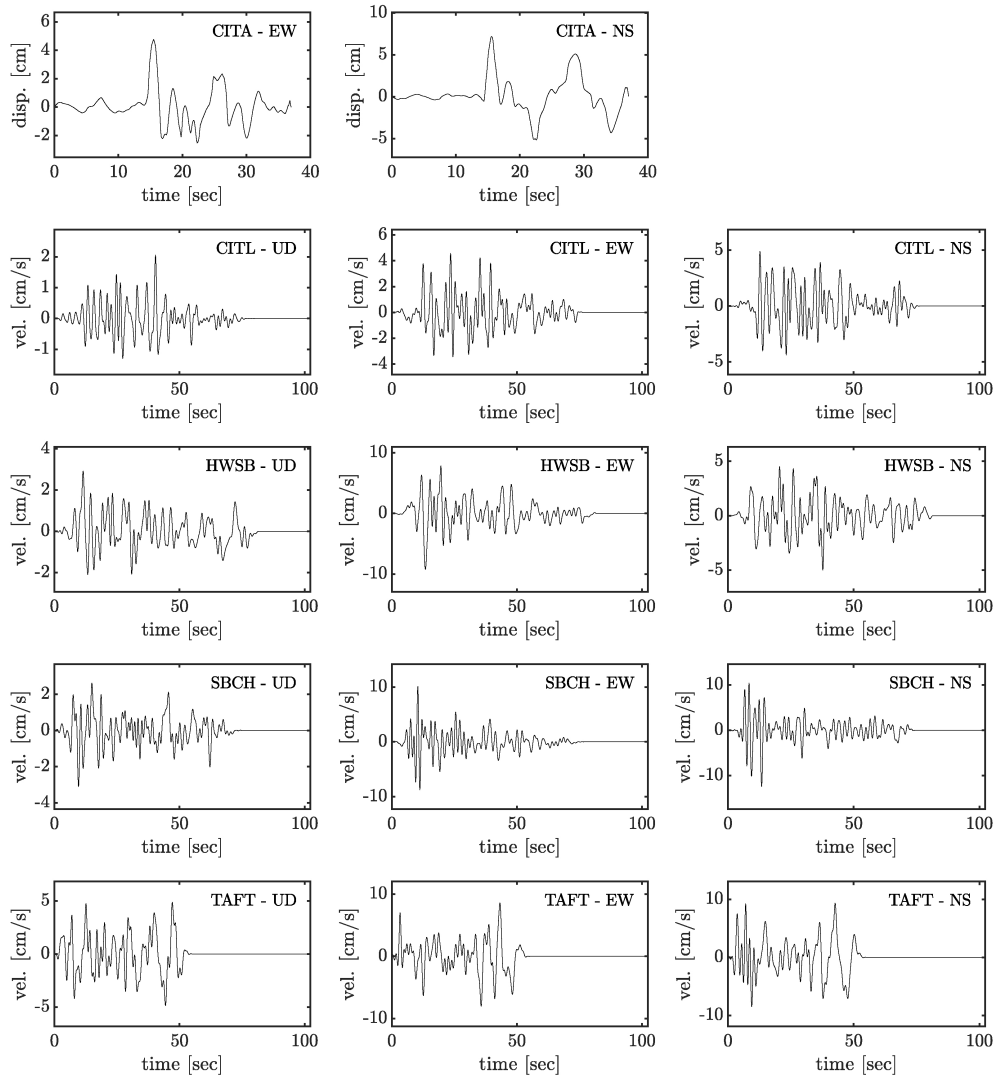
Figure 3.4: Low-pass filtered strong-motion seismic recordings of the 1952 Kern County earthquake. All recording are in an up-down (UD), North-South (NS), East--West (EW) coordinate system. All recording are in units of velocity, with the exception of the CITA records which are in units of displacement, and are filtered from 0.08–0.5Hz. We note that these instrumental recordings are missing initial P-wave arrivals but contain the important S-wave pulse. Stations include: Caltech, Athenaeum (CITA & CITL); Hollywood Storage Basement (HWSB); Santa Barbara City Hall (SBCH) and Taft (TAFT)

FIGURE 3.5 GEODETIC TRIANGULATION NETWORK AND LEVELING LINES
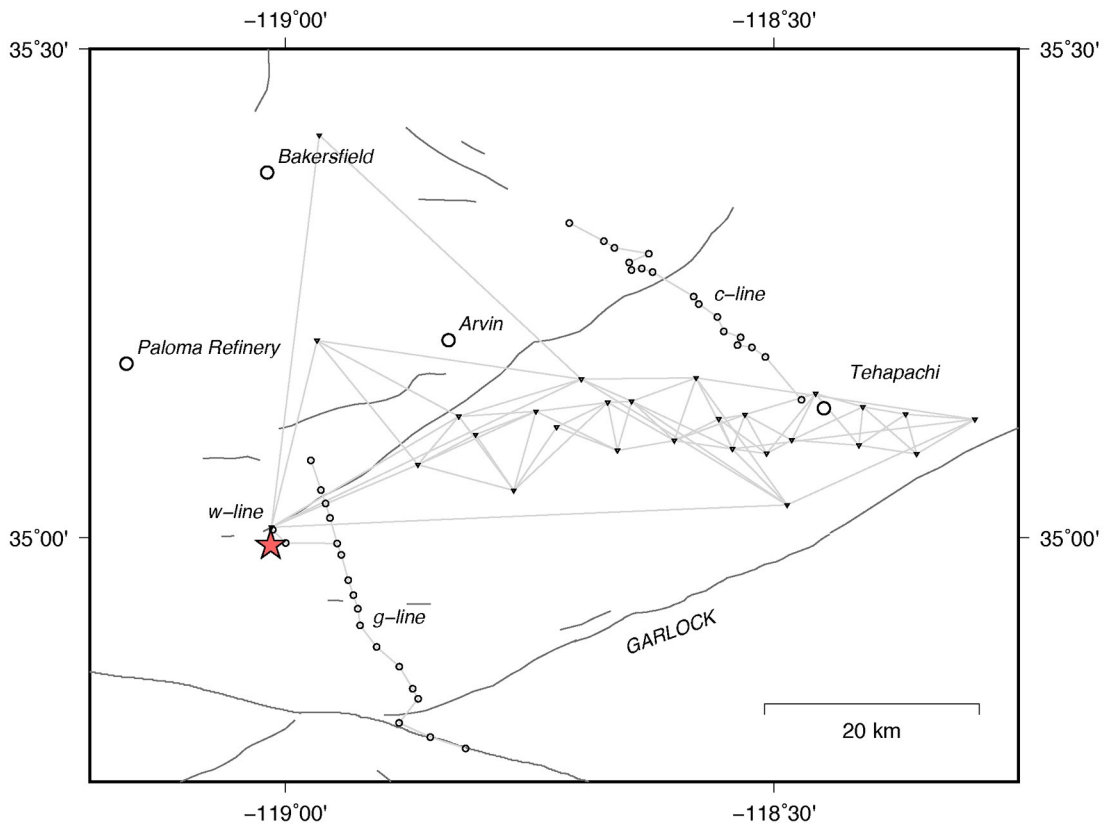

Figure 3.5: Regional map of triangulation network and leveling lines (1926–1972). Faults are outlined in dark grey and the earthquake's epicenter is represented by a red star. Triangulation stations are represented by inverted triangles and connected to one another with light grey lines. There are three leveling lines (c-line, g-line and w-line), which are represented by open circles and connected by light grey lines. Notable places in Kern County include: Bakersfield, Arvin, and Tehachapi.

49

FIGURE 3.6 VELOCITY MODELS
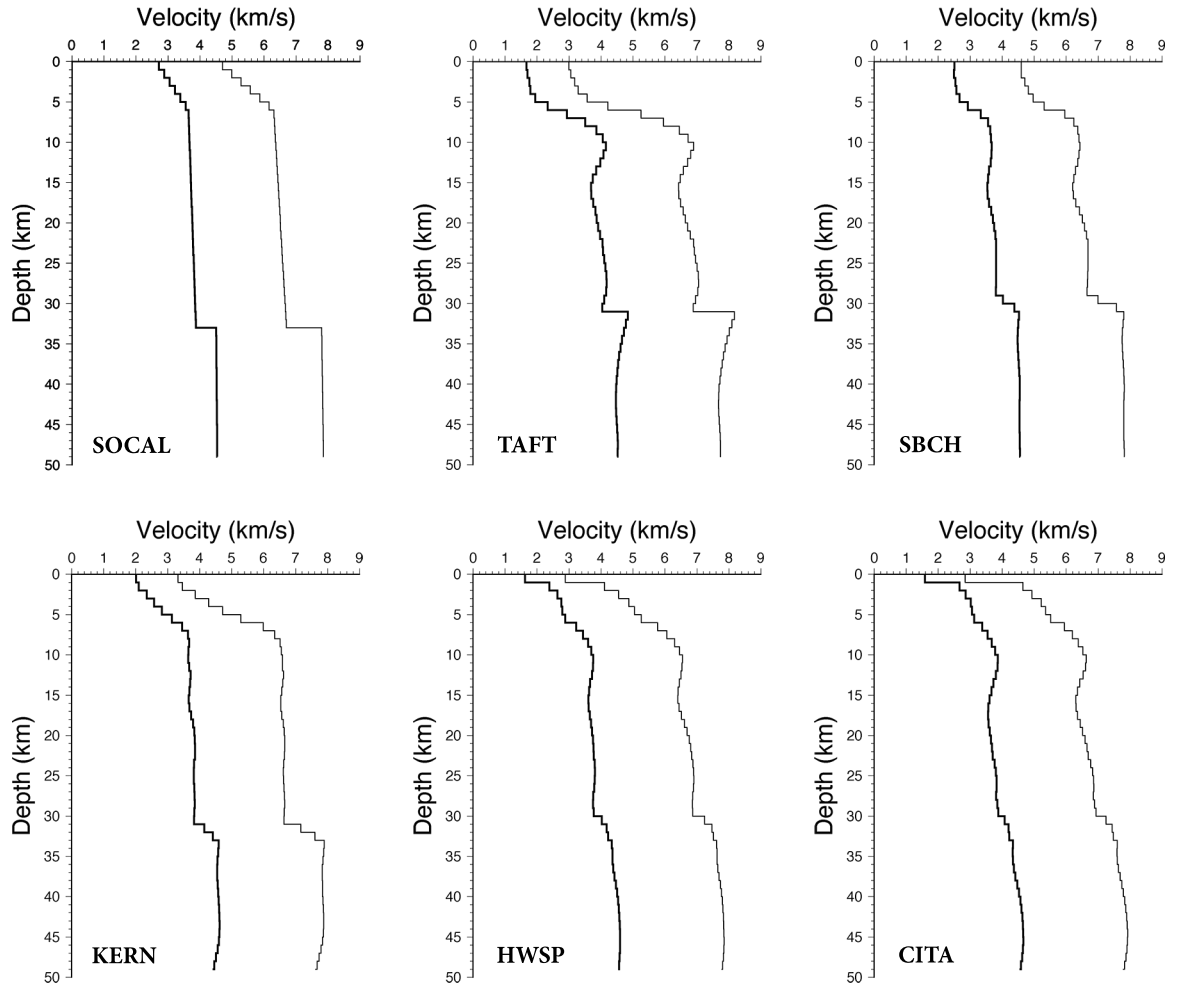
Figure 3.6: Comparison between the average 1D structure proposed by *Kanamori and Hadley* [1975] (SOCAL) and SCEC CVM-S4.26 [*Lee et al.*, 2014; *Small et al.*, 2017]. The geodetic velocity structure (KERN) is made by averaging along- and cross-fault 2D, interpolated cross sections of SCEC CVM-S4.26. All seismic velocity models are averaged from 2D cross-sections between the earthquake hypocenter and station location. Seismic models include: Caltech, Athenaeum (CITA & CITL); Hollywood Storage Basement (HWSB); Santa Barbara City Hall (SBCH) and Taft (TAFT).

FIGURE 3.7 MODEL 1, SLIP AMPLITUDE & DIRECTION
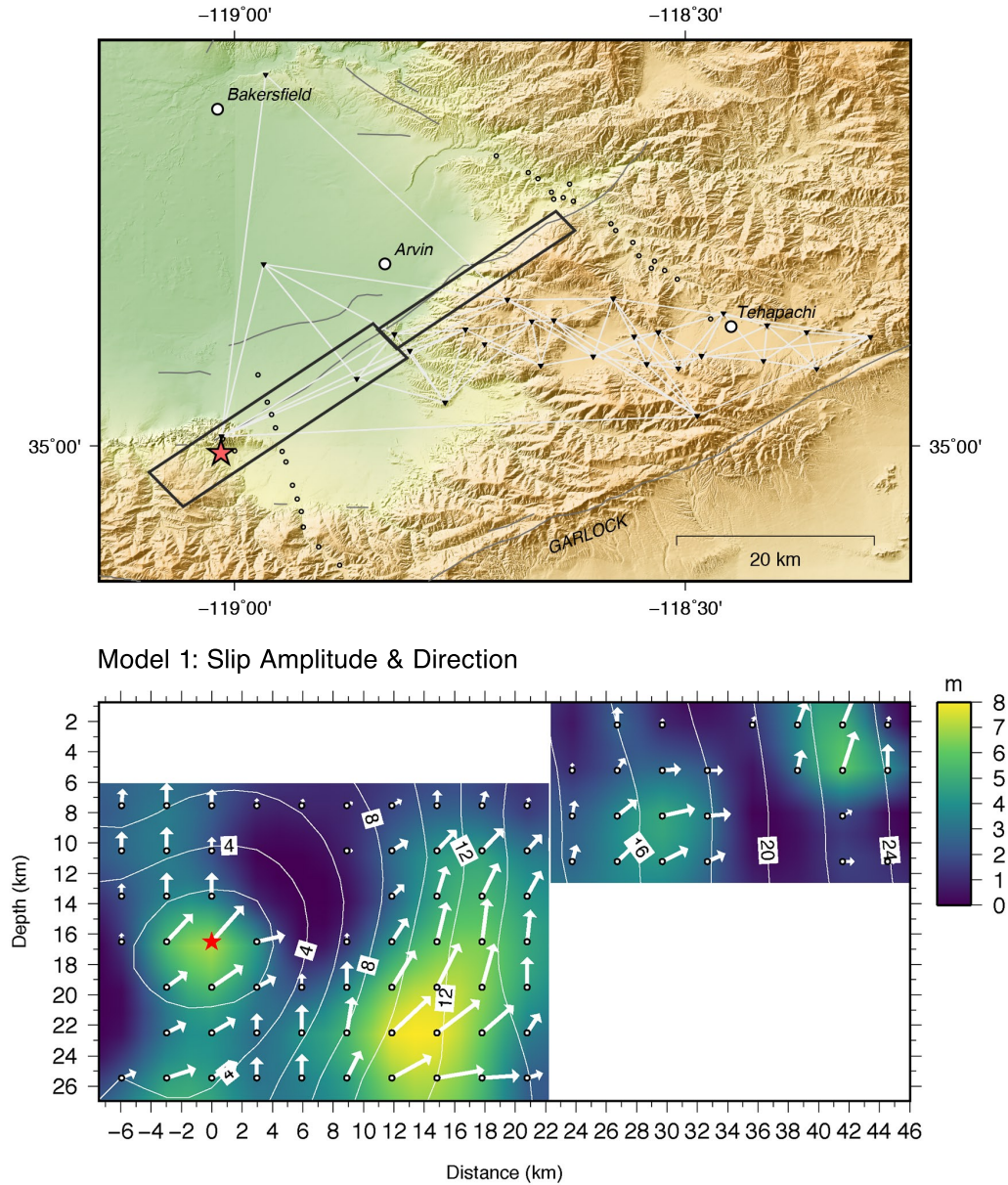
Figure 3.7: Slip amplitude resulting from inversion assuming Bawden's two-segment, right-stepping geometry. There are 102 fault segments in total (open circles). The rupture begins at the hypocenter (red star) and propagates to the northeast. Depth is on the y-axis and along-strike distance on the x-axis. Colors correspond to total displacements (m) and contours denote the rupture propagation through time (s). Vectors point in the direction of rake, (0° to the right and 90° upward) and are also scaled according to total displacements (m).

FIGURE 3.8 MODEL 1, SLIP VELOCITY & RISE TIME
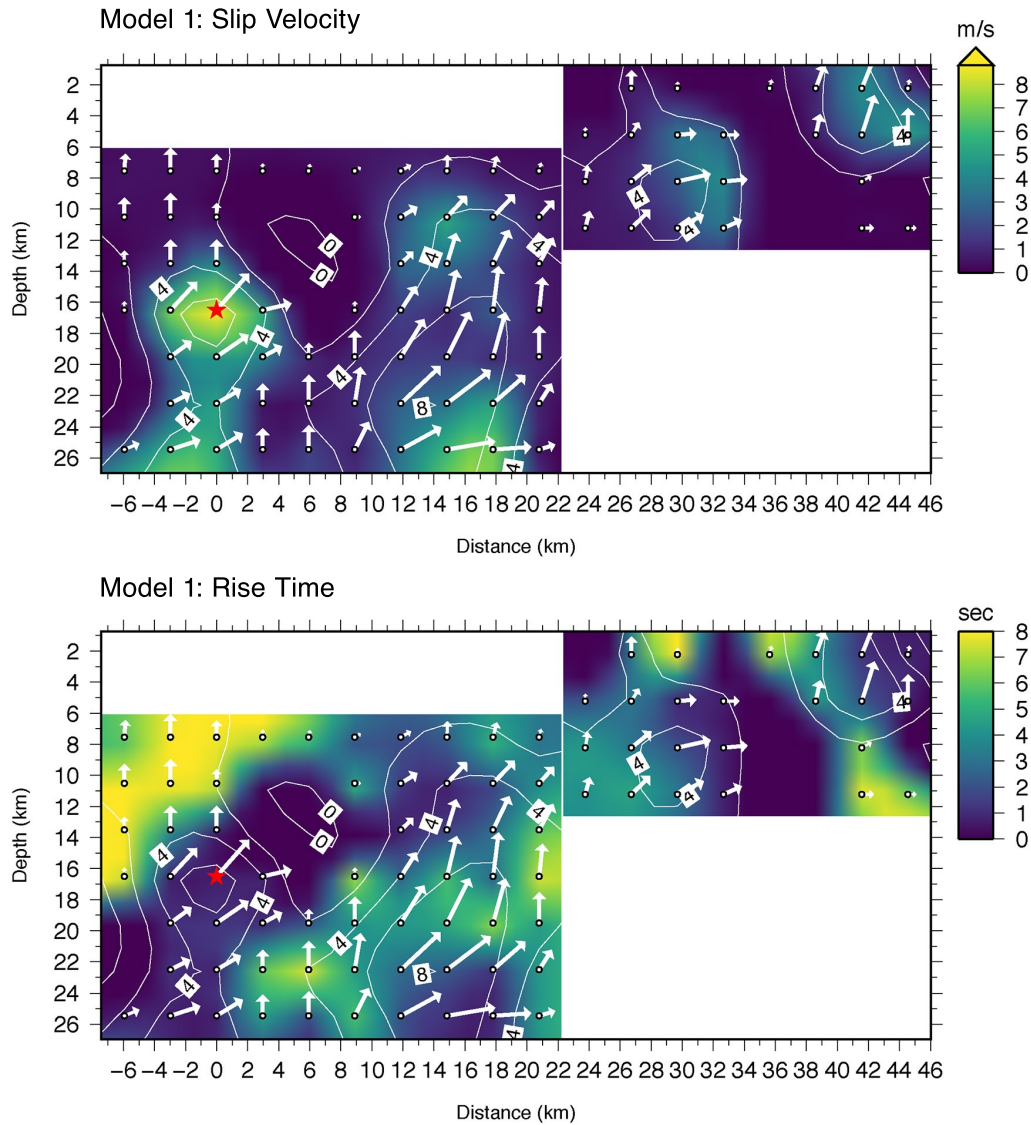
Figure 3.8: Slip velocity and rise time resulting from inversion assuming Bawden's two-segment, right-stepping geometry (continuation of Figure 3.7). Colors correspond to slip velocity (m/s) and rise time (s). Contours and vectors correspond to total slip displacements and directions (Figure 3.7).

FIGURE 3.9 MODEL 1, MOMENT RATE FUNCTION

Figure 3.9: Moment rate function resulting from inversion assuming Bawden's two-segment, right-stepping geometry. The shaded region represents 95% of cumulative moment.

FIGURE 3.10 MODEL 1, SEISMIC WAVEFORM FIT
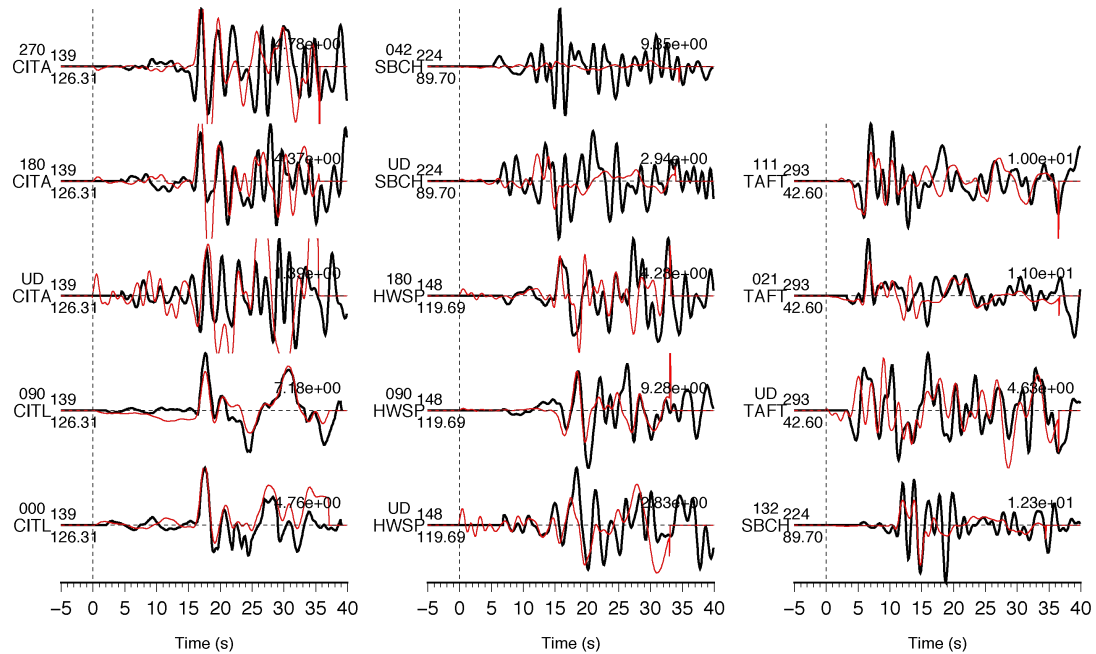
Figure 3.10: Seismic waveform fit resulting from inversion assuming Bawden's two-segment, right-stepping geometry. Black waveforms correspond to observations, filtered from 0.08 to 0.5Hz. Red waveforms correspond to synthetics. Station locations are provided in Figure 3.1. Each recording has a corresponding station name, component orientation (N°E), distance from epicenter (km) and azimuth (N°E).

FIGURE 3.11 MODEL 1, GEODETIC RESIDUALS

Figure 3.11: Triangulation and leveling residuals resulting from inversion assuming Bawden's two-segment, right-stepping geometry. Circles are for triangulation residuals and hexagons are for leveling residuals. Scales corresponding to each measurement residuals are plotting in the top right corner.

FIGURE 3.12 MODEL 2, SLIP AMPLITUDE & DIRECTION
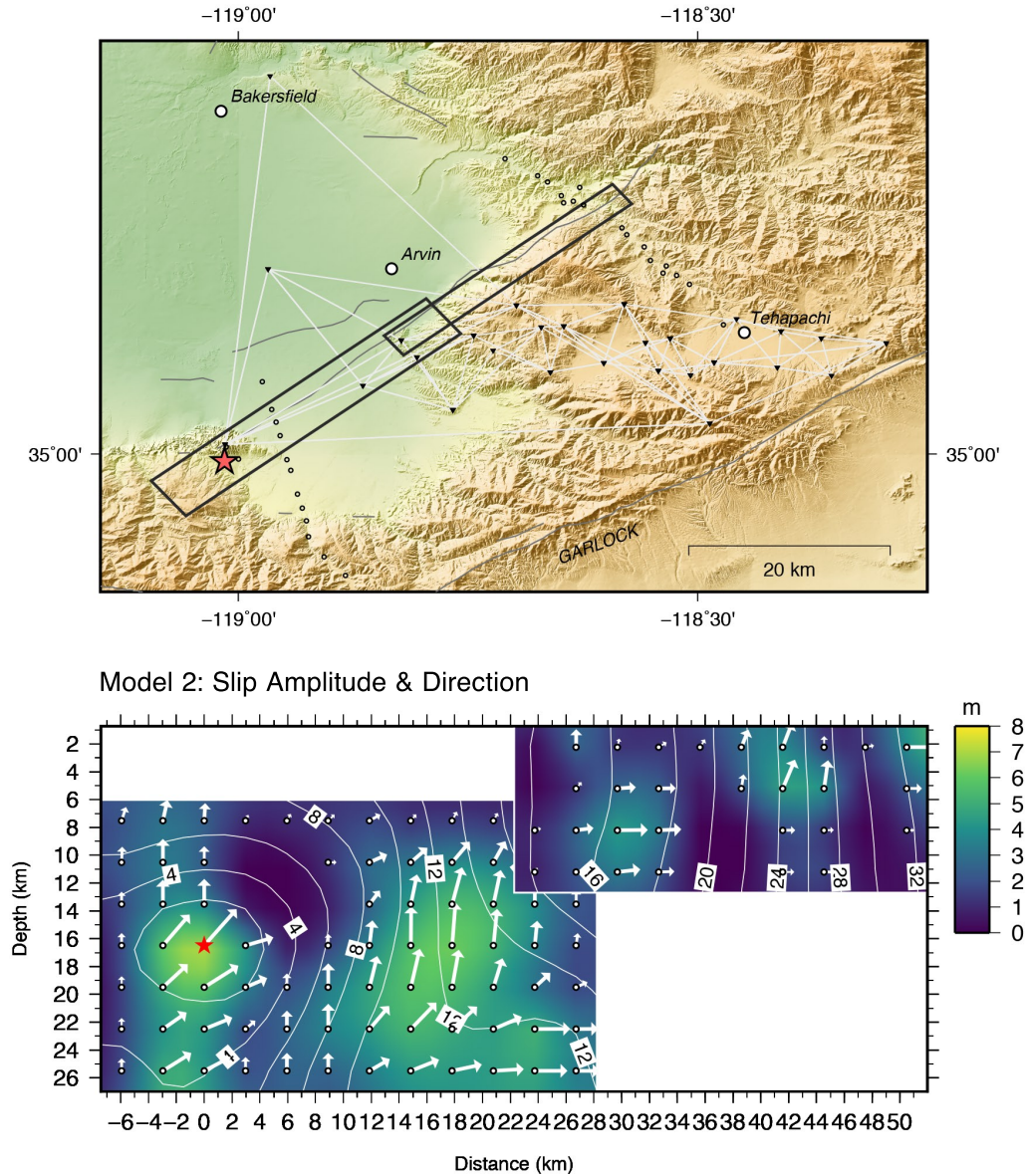
Figure 3.12: Slip amplitude resulting from inversion assuming extended fault planes. There are 124 fault segments in total (open circles). The rupture begins at the hypocenter (red star) and propagates to the northeast. Depth is on the y-axis and along-strike distance is on the x-axis. Colors correspond to total displacements (m) and contours denote the rupture propagation through time (s). Vectors point in the direction of rake, (0° to the right and 90° upward) and are also scaled according to total displacements (m).

FIGURE 3.13 MODEL 2, SLIP VELOCITY & RISE TIME
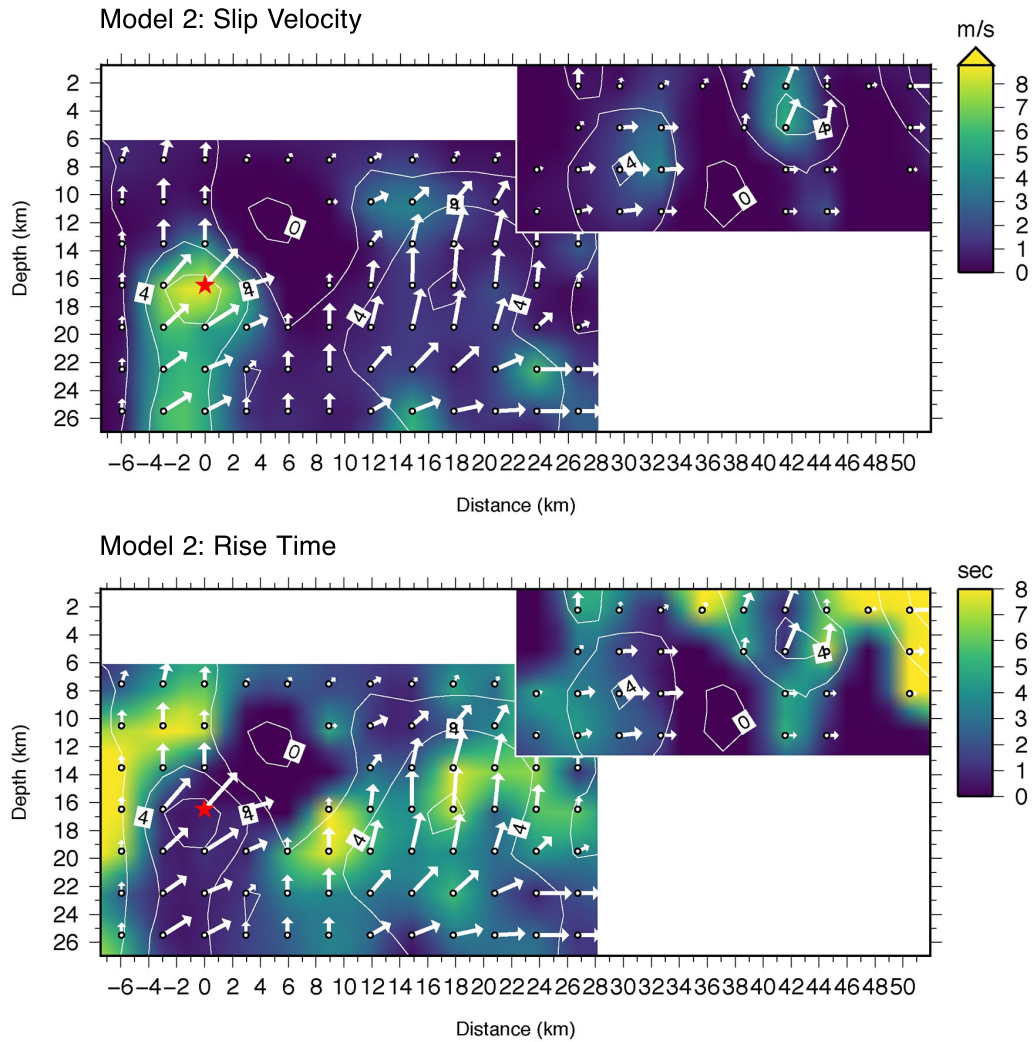
Figure 3.13: Slip velocity and rise time resulting from inversion assuming extended fault planes (continuation of Figure 3.12). Colors correspond to slip velocity (m/s) and rise time (s). Contours and vectors correspond to total slip displacements and directions (Figure 3.12).

FIGURE 3.14 MODEL 2, MOMENT RATE FUNCTION

Figure 3.14: Moment rate function resulting from inversion assuming assuming extended fault planes. The shaded region represents 95% of cumulative moment.

FIGURE 3.15 MODEL 2, SEISMIC WAVEFORM FIT
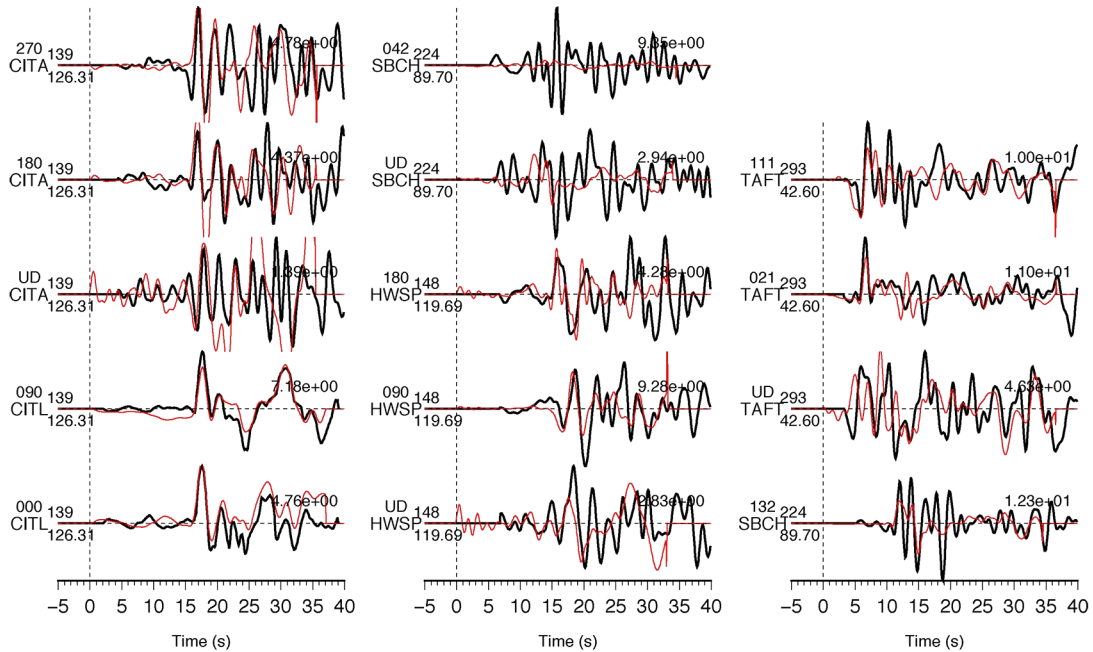
Figure 3.15: Seismic waveform fit resulting from inversion assuming extended fault planes. Black waveforms correspond to observations, filtered from 0.08 to 0.5Hz. Red waveforms correspond to synthetics. Station locations are provided in Figure 3.1. Each recording has a corresponding station name, component orientation (N°E), distance from epicenter (km) and azimuth (N°E).

57

FIGURE 3.16 MODEL 2, GEODETIC RESIDUALS
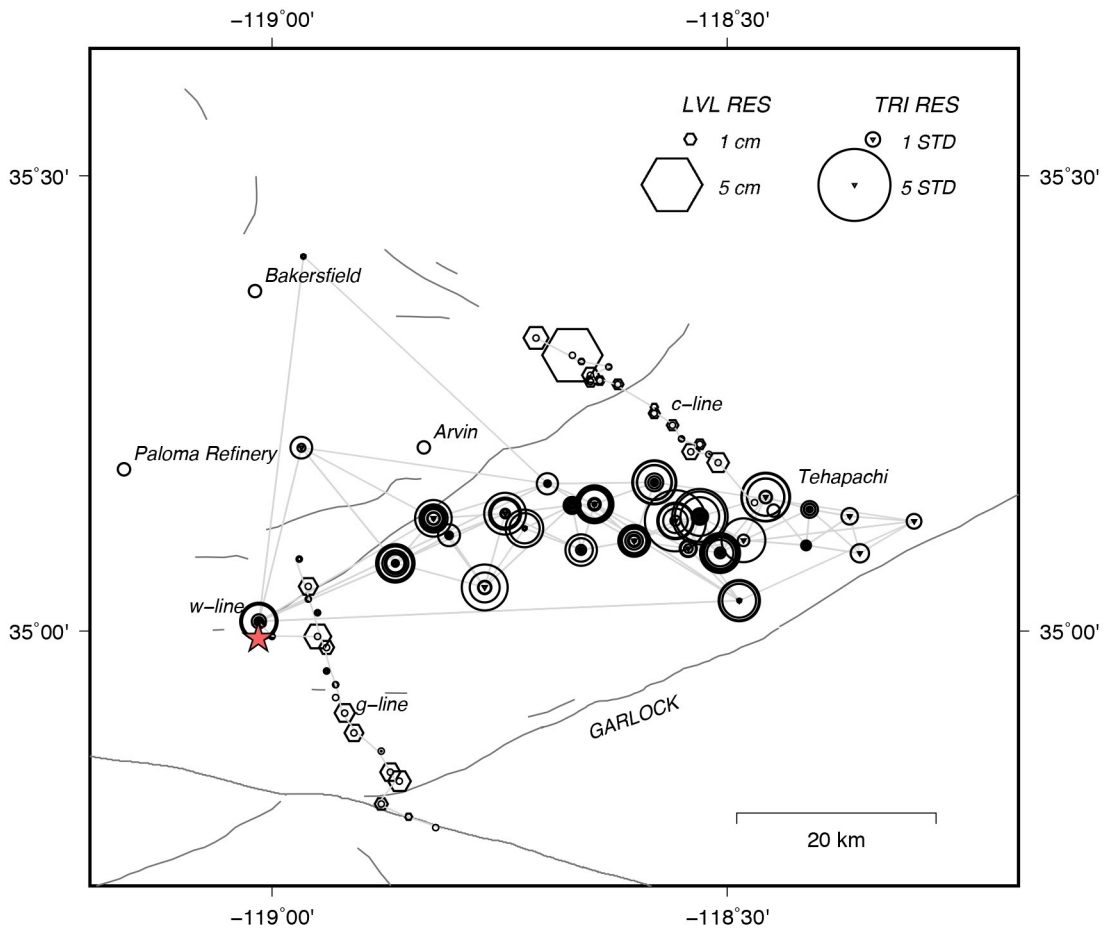
Figure 3.16: Triangulation and leveling residuals resulting from inversion assuming extended fault planes. Circles are for triangulation residuals and hexagons are for leveling residuals. Scales corresponding to each measurement residuals are plotting in the top right corner.

FIGURE 3.17 MODEL 3: SLIP AMPLITUDE & DIRECTION
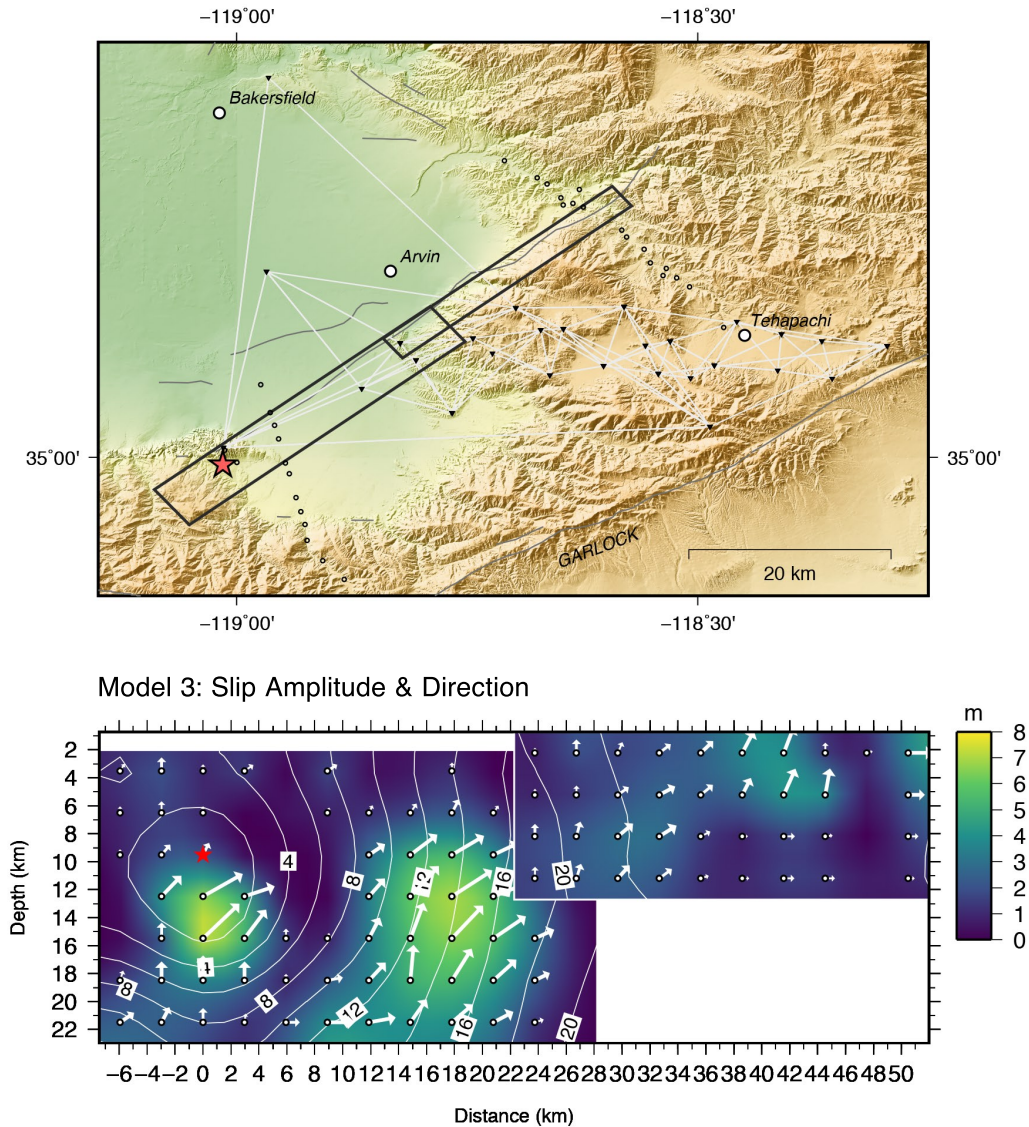
Figure 3.17: Slip amplitude resulting from inversion assuming a source depth of 9.5 km. There are 124 fault segments in total (open circles). The rupture begins at the hypocenter (red star) and propagates to the northeast. Depth is on the y-axis and along-strike distance is on the x-axis. Colors correspond to total displacements (m) and contours denote the rupture propagation through time (s). Vectors point in the direction of rake, (0° to the right and 90° upward) and are also scaled according to total displacements (m).

FIGURE 3.18 MODEL 3, SLIP VELOCITY & RISE TIME
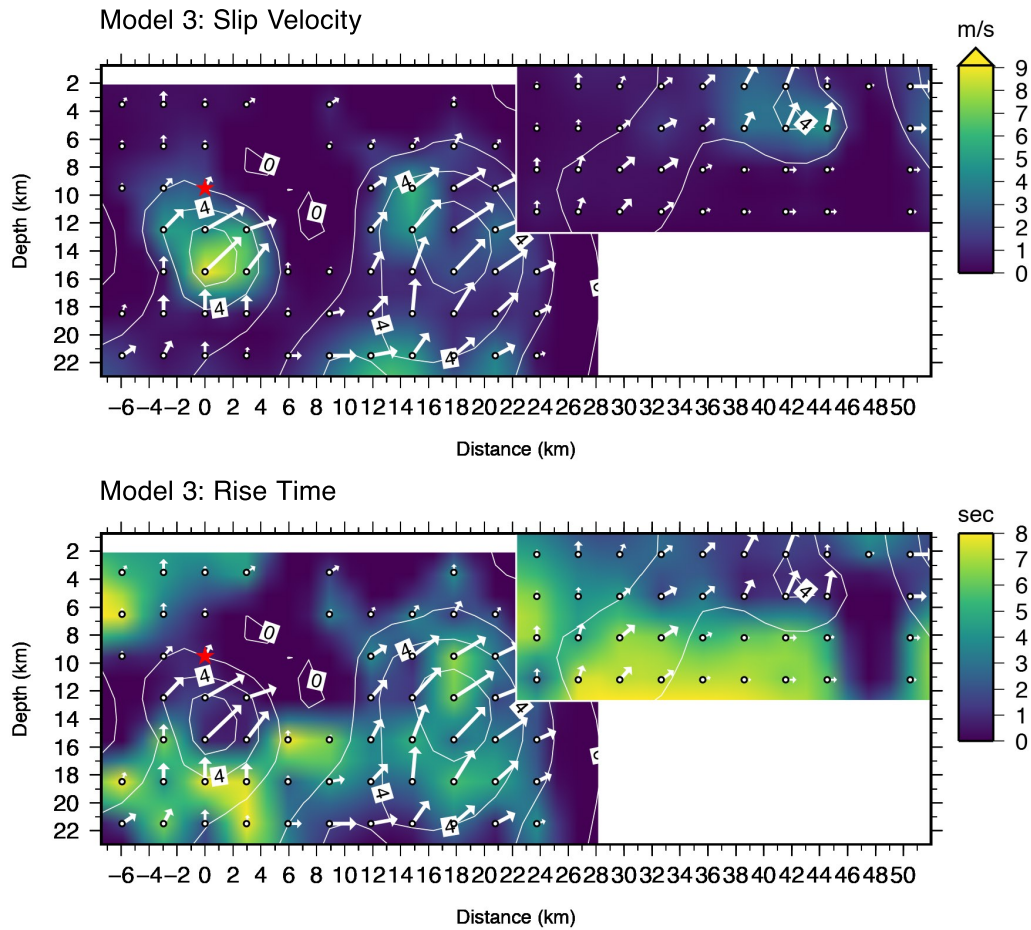
Figure 3.18: Slip velocity and rise time resulting from finite fault inversion assuming a source depth of 9.5 km (continuation of Figure 3.17). Colors correspond to slip velocity (m/s) and rise time (s). Contours and vectors correspond to total slip displacements and directions (Figure 3.17).
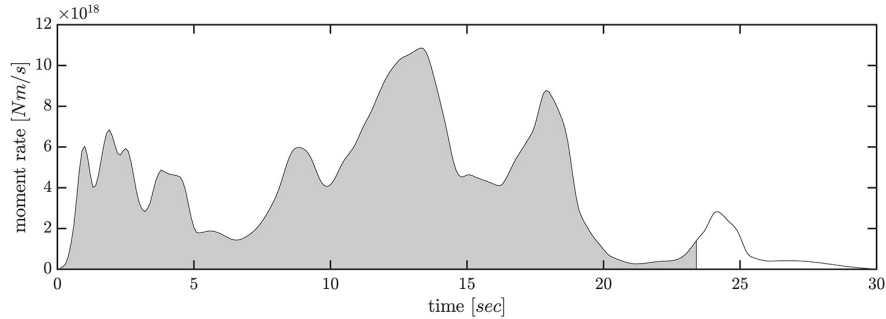
FIGURE 3.19 MODEL 3, MOMENT RATE FUNCTION
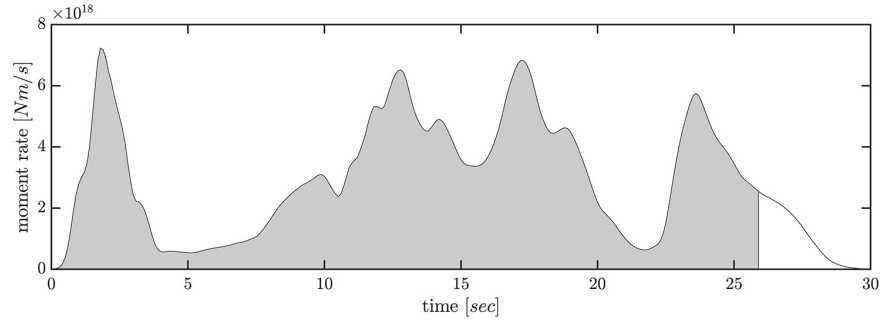
Figure 3.19: Moment rate function resulting from inversion assuming a source depth of 9.5 km. The shaded region represents 95% of cumulative moment.

FIGURE 3.20 MODEL 3, SEISMIC WAVEFORM FIT
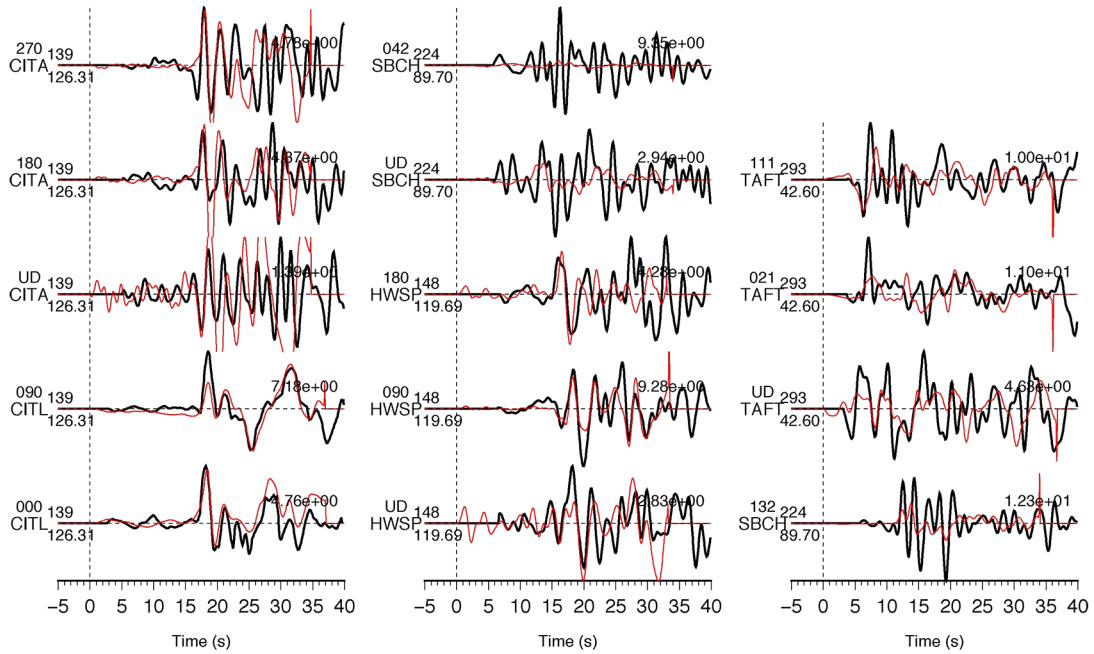
Figure 3.20: Seismic waveform fit resulting from inversion assuming a source depth of 9.5 km. Black waveforms correspond to observations, filtered from 0.08 to 0.5Hz. Red waveforms correspond to synthetics. Station locations are provided in Figure 3.1. Each recording has a corresponding station name, component orientation (N°E), distance from epicenter (km) and azimuth (N°E).

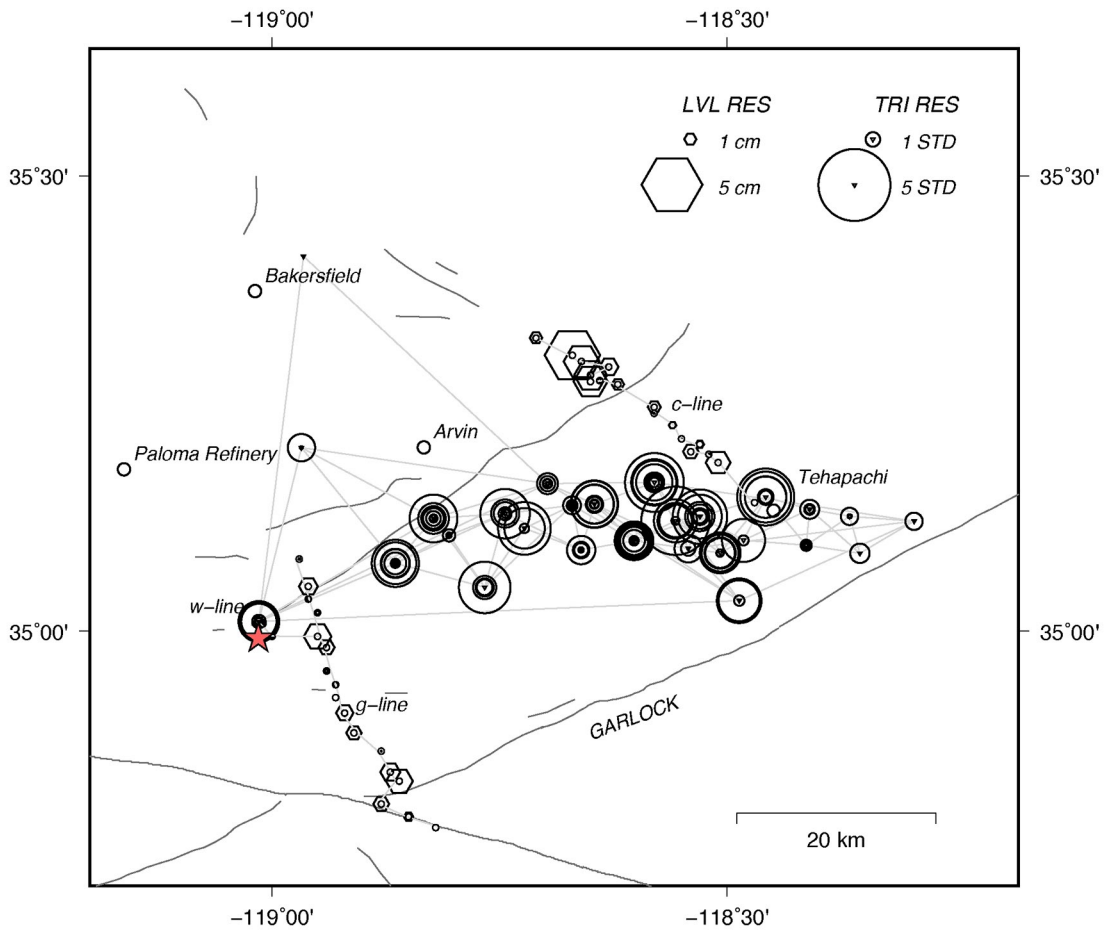61

FIGURE 3.21 MODEL 3, GEODETIC RESIDUALS
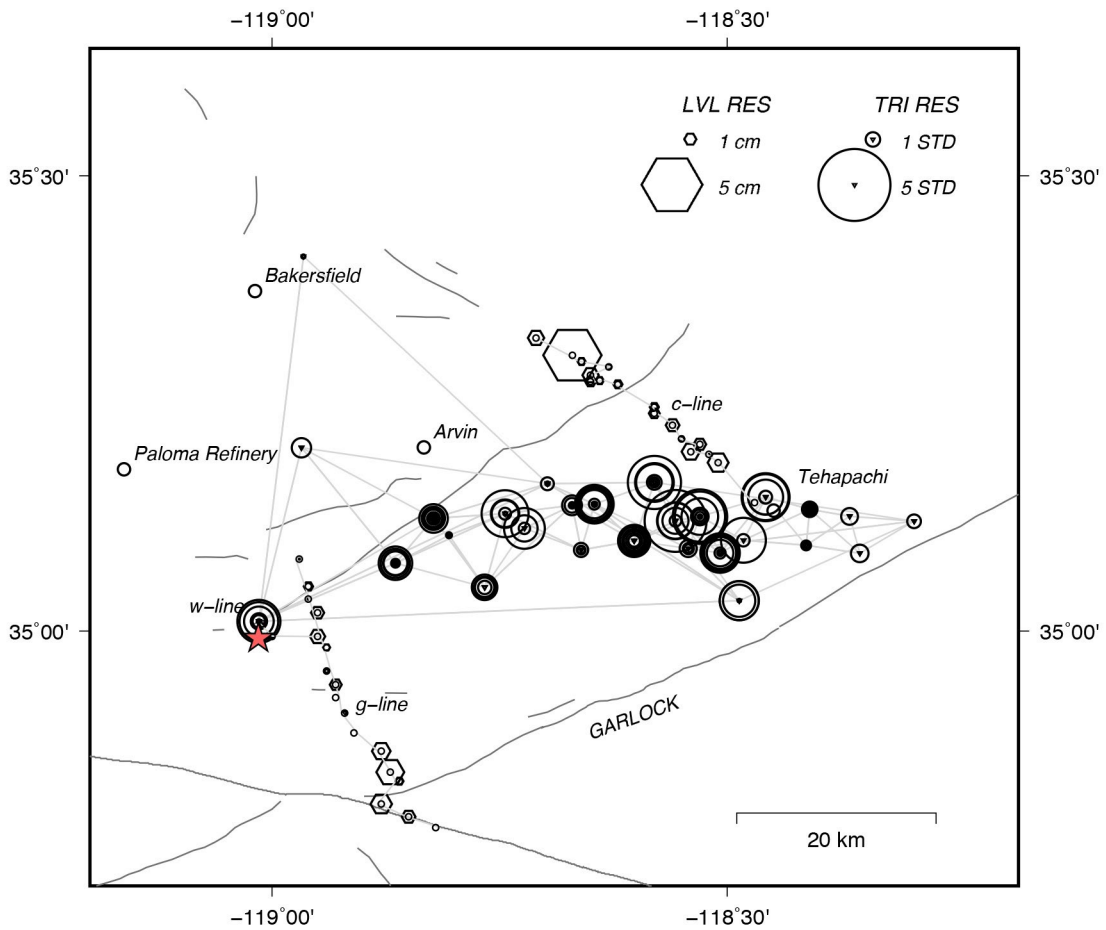
Figure 3.21: Triangulation and leveling residuals resulting from inversion assuming a source depth of 9.5 km. Circles are for triangulation residuals and hexagons are for leveling residuals. Scales corresponding to each measurement residuals are plotting in the top right corner.

FIGURE 3.22 MODEL 4, SLIP AMPLITUDE & DIRECTION

Model 4: Slip Amplitude & Direction
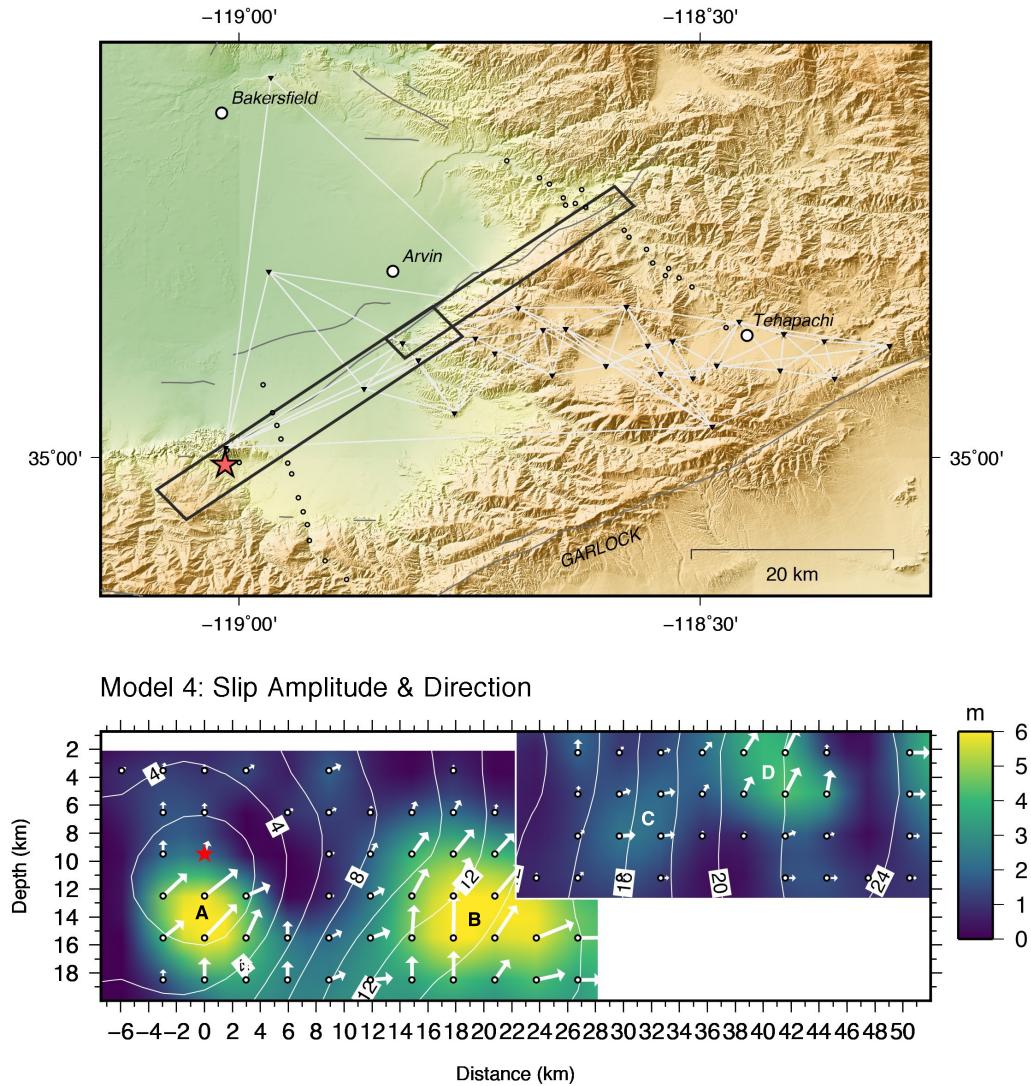
Figure 3.22: Slip amplitude resulting from inversion assuming a maximum seismogenic depth of 20 km. There are 112 fault segments in total (open circles). The rupture begins at the hypocenter (red star) and propagates to the northeast. Depth is on the y-axis and along-strike distance is on the x-axis. Colors correspond to total displacements (m) and contours denote the rupture propagation through time (s). Vectors point in the direction of rake, (0° to the right and 90° upward) and are also scaled according to total displacements (m). Asperities have been labeled (A–D) along strike.

FIGURE 3.23 MODEL 4, SLIP VELOCITY & RISE TIME
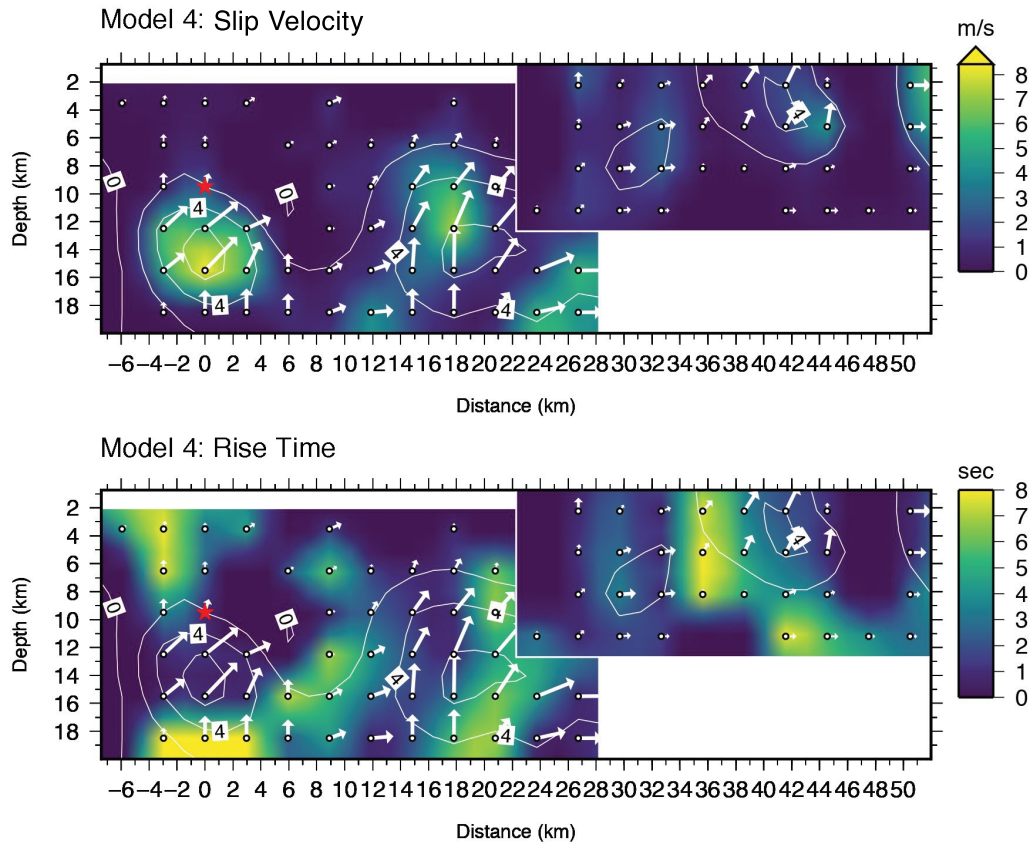
Figure 3.23: Slip velocity and rise time resulting from inversion assuming a maximum seismogenic depth of 20 km (continuation of Figure 3.22). Colors correspond to slip velocity (m/s) and rise time (s). Contours and vectors correspond to total slip displacements and directions (Figure 3.22).
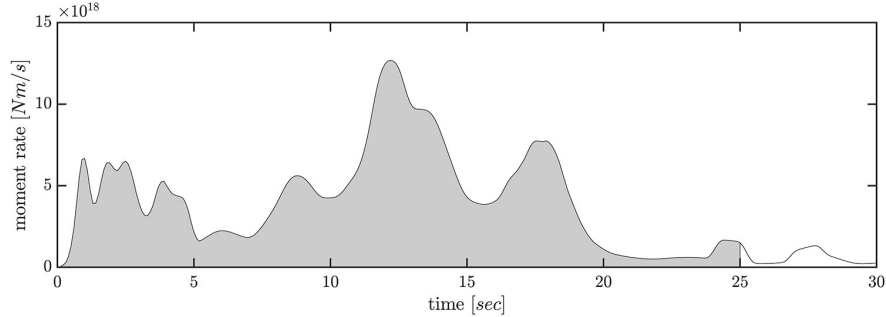
FIGURE 3.24 MODEL 4, MOMENT RATE FUNCTION
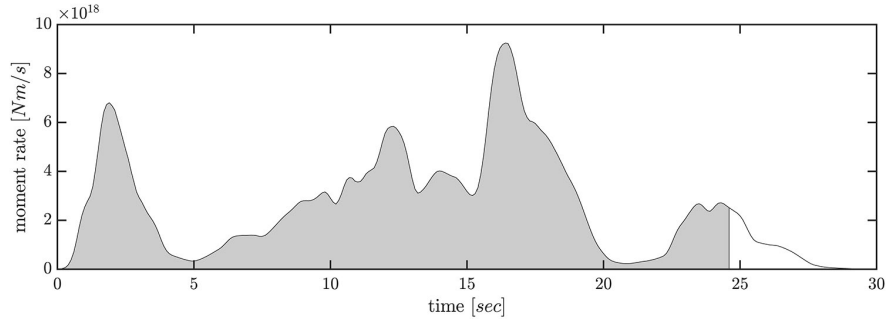
Figure 3.24: Moment rate function resulting from inversion assuming assuming a maximum seismogenic depth of 20 km. The shaded region represents 95% of cumulative moment.

FIGURE 3.25 MODEL 4, SEISMIC WAVEFORM FIT
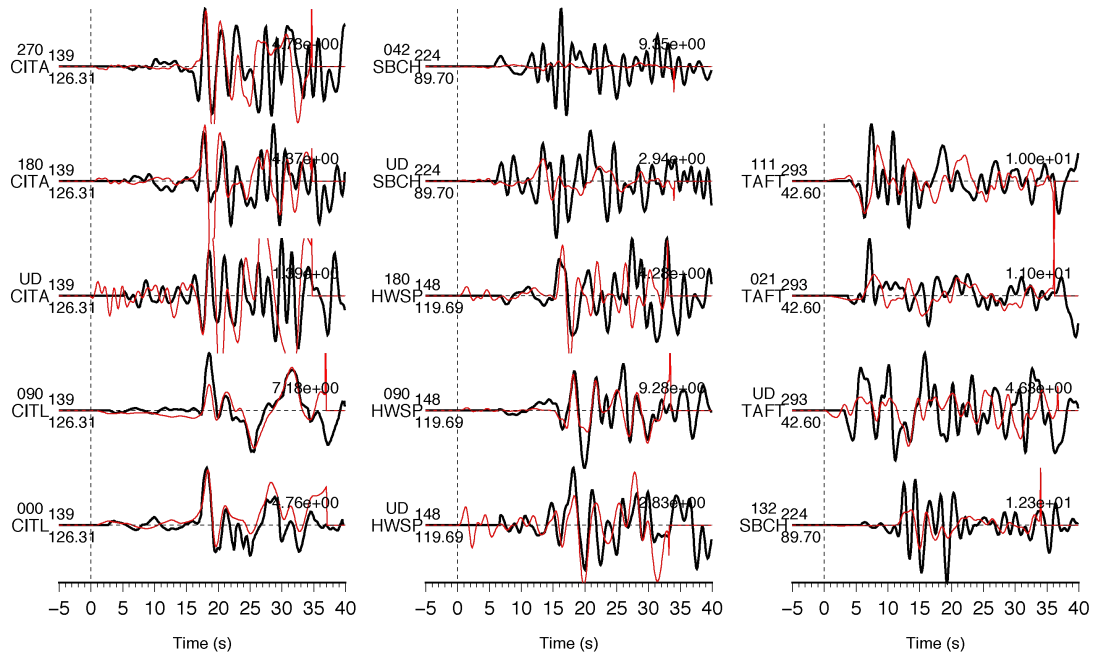
Figure 3.25: Seismic waveform fit resulting from inversion assuming a maximum seismogenic depth of 20 km. Black waveforms correspond to observations, filtered from 0.08 to 0.5Hz. Red waveforms correspond to synthetics. Station locations are provided in Figure 3.1. Each recording has a corresponding station name, component orientation (N°E), distance from epicenter (km) and azimuth (N°E).

FIGURE 3.26 MODEL 4, GEODETIC RESIDUALS
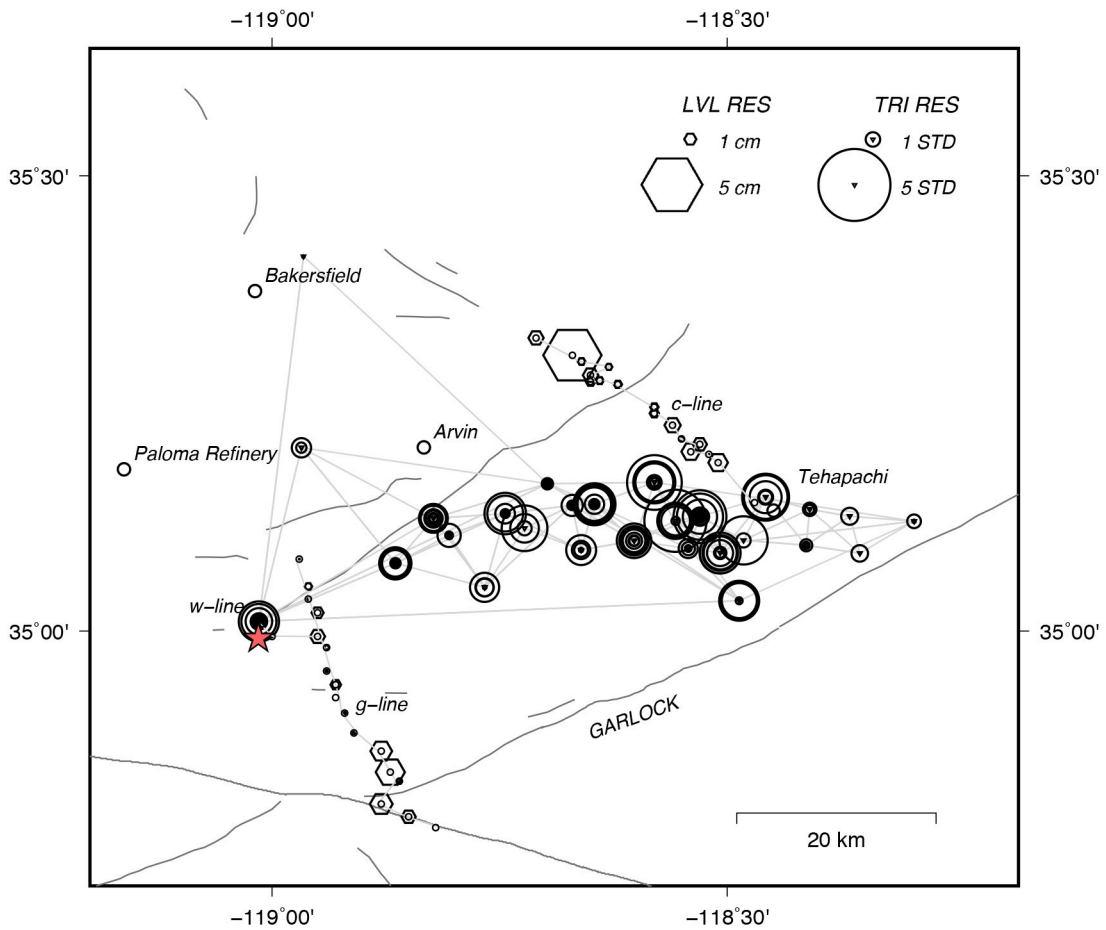
Figure 3.26: Seismic waveform fit resulting from inversion assuming a maximum seismogenic depth of 20 km. Circles are for triangulation residuals and hexagons are for leveling residuals. Scales corresponding to each measurement residuals are plotting in the top right corner.

FIGURE 3.27 MODEL 4, AVERAGE STRESS DROP
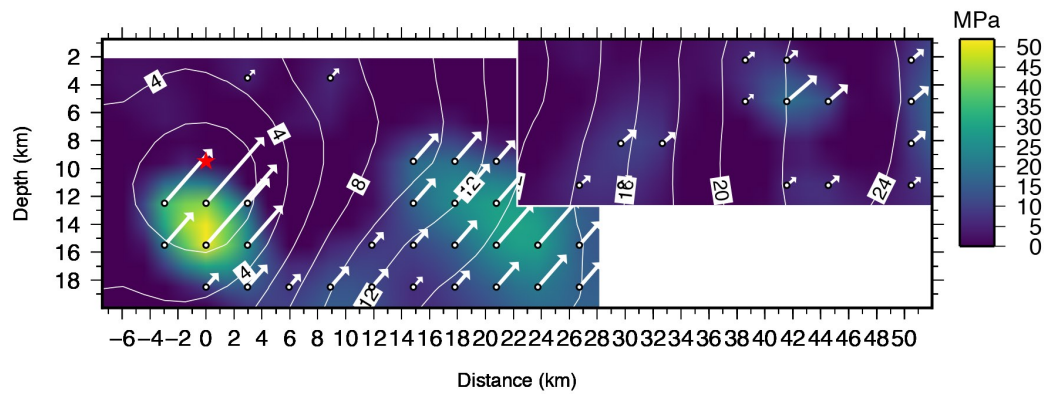
Figure 3.27: Stress drop in the direction of average rake. Depth is on the y-axis and along-strike distance is on the x-axis. Colors correspond to stress drop (MPa) and contours denote the rupture propagation through time (s). Vectors point in the direction of average rake, (0° to the right and 90° upward) and are also scaled according to stress drop (MPa). Peak stress drop is 52 MPa.

Chapter 4

Discussion

4.1 Slip History

Our study reveals that the M_W 7.2, Kern County earthquake had a very complicated rupture history. The rupture initiated on a shallow dipping branch of White Wolf fault system with dominant left-lateral strike-slip motion (strike=49±4°, dip=35±1°, and rake=11±5°). While, the hypocenter of this nucleation event is not well constrained, it is most likely larger than 5 km.

The subsequent rupture on the White Wolf fault (strike=51°and dip=75°) was triggered at approximately 2.0 s later. The cumulative seismic moment in next 5 s is about 1.5×10^{19} Nm (M_W 6.75). Using the simple circular fault approximation, $\Delta\sigma_s \approx 2.44 M_0/A^{3/2}$ [*Kanamori and Anderson*, 1975], the average static stress drop for this sub-event is 50 MPa. Considering the fact that we chose a relatively large sub-fault size (3 km by 3 km), the size of asperity A (9 km by 6 km in Model 4) could be smaller. Therefore this stress-drop estimate is representative of a lower bound. The centroid depth of asperity A is 15–17 km. The peak slip of this patch is also reasonably well constrained (6.6–7.1 m), although this may be the result of large sub-fault size [*Shao and Ji*, 2012].

Over the next 7-8 s, the rupture propagated unilaterally along the strike until it broke asperity B from its southwest edge (approximately 12 km away from the hypocenter). The dimensions of asperity B are 18 km along strike and 12 km down dip. The rupture of this asperity was relatively slow and continued for approximately 10 s. The cumulative seismic moment for this rupture is 4.3×10^{19} Nm (M_W 7.05) and the static stress drop of this asperity is 33 MPa.

Rupture initiation along the NEF occurred before the end of asperity B rupturing at about 15 s. Asperity C has a seismic moment of 1.0×10^{19} Nm (M_W 6.63), failing roughly from 15 to 20 s with dominant strike-slip motion. The rupture of asperity D occurred from 22 to 30 s and also released a similar amount of seismic moment, 1.0×10^{19} Nm (M_W 6.63). However, the temporal evolution of slip within the NEF is poorly constrained.

4.2   Comparison with Previous Works

4.2.1   Magnitudes

The M_W of 7.2–7.3 is consistent with previous published magnitude estimates for the 1952 Kern County, California earthquake [*Gutenberg*, 1955c; *Ben-Menahem*, 1978; *Dunbar et al.*, 1980; *Stein and Thatcher*, 1981; *Bawden*, 2001].

4.2.2   Ben-Menahem [1978]

Ben-Menahem [1978] modeled this earthquake using a rupture velocity of 3.2 km/s and a total rupture duration of 24 s. Our results show that the rupture velocity during this earthquake, particularly on the southwest fault, is slow (approximately 1.5 km/s). We note that *Ben-Menahem* [1978] assumed uniform slip on a fault of 65 km. Our slip model suggest a similar fault length but 75% of seismic moment occurred on SWF.

Whether this heterogeneous rupture can explain the directivity observations reported by *Kanamori and Jennings* [1978] will be one of our future efforts.

4.2.3   Kanamori and Jennings [1978] & Bolt [1978]

Kanamori and Jennings [1978] and *Bolt* [1978] reported a M_L of 7.2 for the Kern County earthquake, which is, to our best knowledge, the largest M_L measurement of any earthquake in the literature. While M_L is defined as $M_L = log(A_{wa}) - log(A_0)$, where A_{wa} is the half peak-to-peak amplitude of a Wood Anderson recording [*Richter*, 1935], *Boore* [1983] reported an empirical, linear relationship between peak ground velocity (PGV) and A_{wa} ($PGV \approx 0.77A_{wa}$). Thus, inspecting observed PGV could shed the light on the possible cause of the abnormally large M_L.

We find, at stations with abnormally large M_L estimates (for example, SBCH), that the PGV in strong-motion seismic recordings is dominated by seismic phases radiated from asperity A (Figure 3.22). We note, that while asperity A only has a M_W of 6.75, its average stress drop is 50 MPa. This is 5 times larger than the 10 MPa stress drop that *Brune* [1970] and *Boore* [1983] used to explain the M_L observations in California. Therefore, if we use reported the numeric scaling relationship between PGV and stress drop ($log(PGV) \approx (1/3)log(M_0) + (2/3)log(\Delta\sigma) + c$) [*Boore*, 1983] we can estimate a M_L for this event. Based on the assumption that the scaling relationship between M_W and M_L is similar for a M_W 6.75 earthquake [*Bakun*, 2006], the predicted M_L for asperity A would be 7.15–7.25. This value is close to the estimates made by *Kanamori and Jennings* [1978] and *Bolt* [1978]. Such an agreement suggests that the previous reported high M_L estimate reflects the abnormally high stress drop that occurred during the beginning portion of the 1952 Kern County, California earthquake.

4.2.4 Geodetic Studies

All available solutions indicate that the rupture of the Kern County earthquake occurred on a high angle fault plate fault (60°<dip<80°), with rake angles ranging from 32–57°. Comparing these results to previously published source studies, we note that the weighted average rake of 47–57°over the SWF is in good agreement with *Dunbar et al.* [1980] and *Stein and Thatcher* [1981]. It is however, notably smaller than the solutions proposed by *Gutenberg* [1955c] and *Ben-Menahem* [1978], and greater than the solution proposed by *Bawden* [2001]. For the NEF, the weighed average rake angles appear to be less constrained and ranges from 32–50°.

4.3 Regional Velocity Structure

The White Wolf fault is not very active, with slip rates less than 10 mm/yr [*Stein and Thatcher*, 1981; *Hearn et al.*, 2013]. One of the most striking features of our inversion results is the along strike variation of rupture depth (Figures 3.7, 3.12, 3.17 and 3.22). Slip on the southwest fault plane is deeper than 8 km and possibly extends to depths greater than 20 km (centroid depth around 14-16 km). Slip on the northeast fault plane, in contrast, is shallower than 12 km. The southwest fault plane in our preferred model is bounded by high topography to the southwest (Wheeler Ridge) and to the northeast (Comanche Point). Geological maps show that the basement depth increases sharply by approximately 3 km when crossing the White Wolf fault [*Oakeshott*, 1955]. This is consistent with the thrust motion of southwest fault plane.

It is of interest to note that the centroids of asperities A and B are located beneath the basin-side foothills of these two regions of high topography. Additionally, the epicenter of the 1952 Kern County earthquake is located at the northwest edge of Wheeler Ridge. To explore the relationship between topography and slip distribution, we make several

velocity profiles using SCEC CVM-S4.26 (Figure 4.1) [*Lee et al.*, 2014; *Small et al.*, 2017], along which we interpolate V_P and V_S (Figures 4.2–4.3). This state-of-art velocity model was constrained using a full-3-D tomography technique with 38,000 earthquake seismograms and 12,000 ambient-noise correlagrams. The smallest scale that can be resolve in this velocity model is about 5 km within center of the tomography region from about 1 km to 25 km depth [*Lee et al.*, 2014].

Subsequently, we observe a bi-modal distribution of slip with respect to the the southwest and northeast fault planes. Fault slip within the southwest fault occurs at depths deeper than 10 km and sharply transitions to depths less than 10 km, moving along strike. The along fault cross section (Figure 4.2) has V_P values (up to 7.2 km/s) and V_S values (up to 4.4 km/s). Near the hypocenter, there is a high velocity anomaly with $V_p > 6.8$ km/s and $V_s > 3.8$ km/s. It is of interest to note that we see a high correlation between this V_P region and the centroid depth of asperity A (15–17 km). To the northeast, there is a low velocity anomaly with $V_p < 6.0$ km/s and $V_s < 3.2$ km/s spanning a depth range of 10 to 20 km. Above it, is another high velocity anomaly, which is correlated with asperities C and D. The cause of abnormally low velocity in the mid-crust is not clear but if it is a result of higher crustal temperatures, the bottom of seismogenic zone would be raised. *Huang and Zhao* [2013] found that the locations of large interplate thrust earthquakes correspond to regions of high seismic velocity and that low velocity zones are correlated with the regions of low GPS backslip rates. It is not clear why there is high friction associated with rock that has higher seismic velocities.

Profiles in Figure 4.3 show additional cross-fault seismic velocities. *Lee et al.* [2014]; *Small et al.* [2017] previously reported high seismic velocities within this region and attribute them to the structure of the San Joaquin basin. High velocities along the left-hand side of these cross-sections are thought represent a large scale middle crust high velocity structure, and the White Wolf fault appears to mark its southern edge.
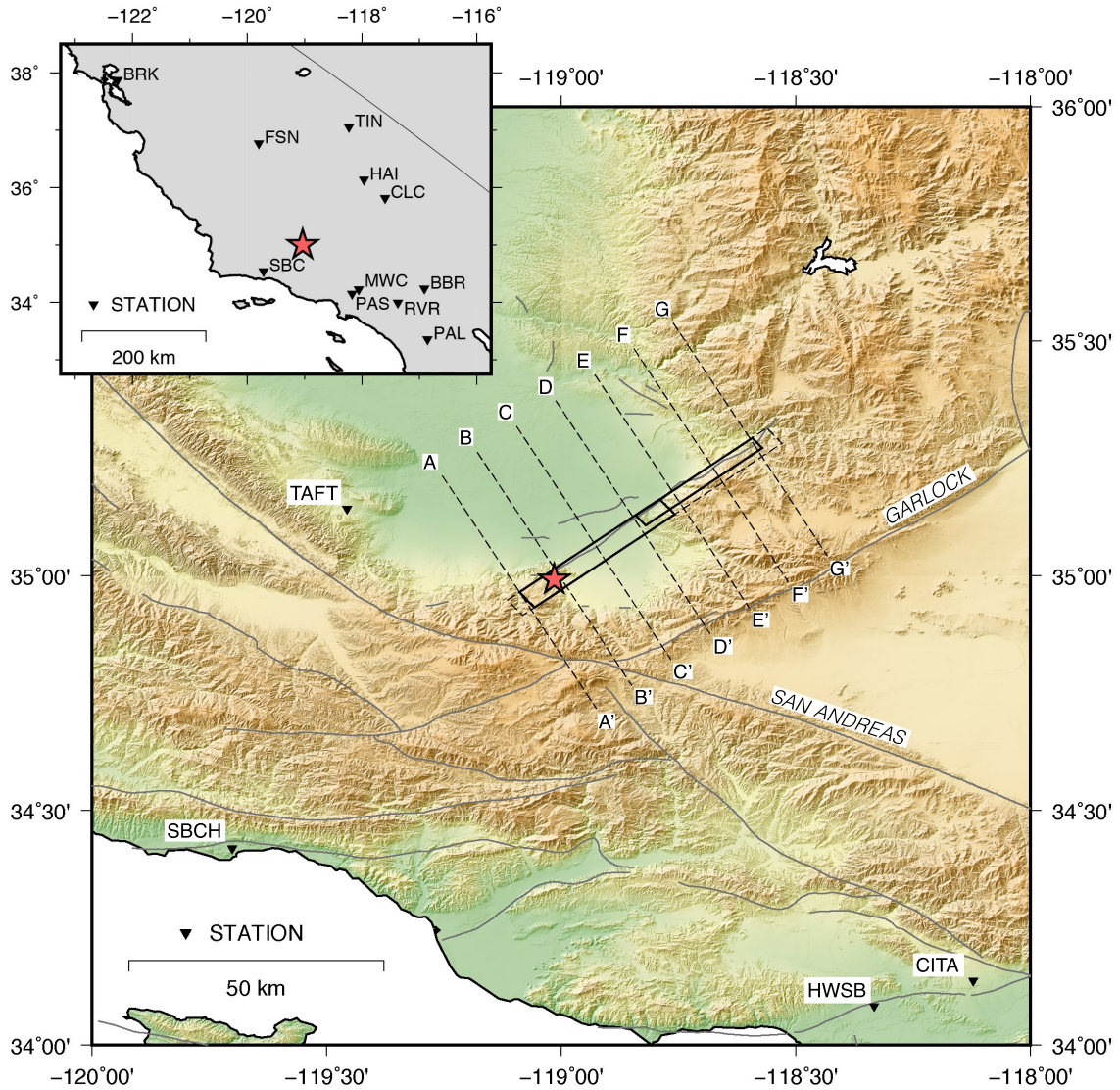
Figure 4.1: Top down view of cross sections made every 10 km along strike (dashed lines). Faults are outlined in dark grey. Model 4 fault geometry is shown in solid black. The earthquake epicenter is represented by a red star. Surrounding strong motion stations are labeled with an inverted triangle (colored panel). First-motion stations are in the grey panel.

FIGURE 4.2 ALONG FAULT, SCEC CVM-S4.26
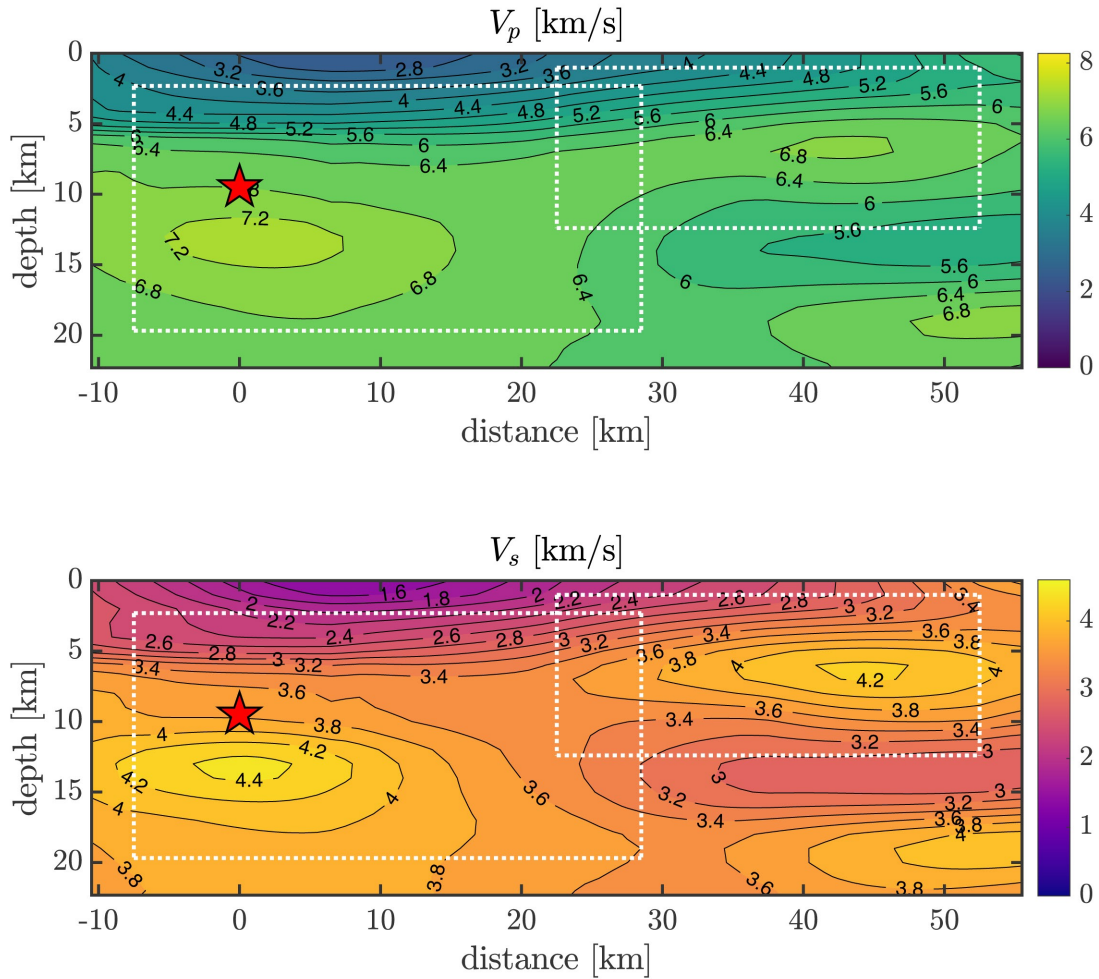
Figure 4.2: Along fault velocity structure according to SCEC CVM-S4.26 [*Lee et al.*, 2014; *Small et al.*, 2017]. We see a bi-modal distribution of high seismic velocities that correlates with regions of high slip. This cross section dips at 75°and runs parallel with the Model 4 fault geometry (white dashed rectangles). Seismic velocities are in units of km/s. The hypocenter (depth of 9.5 km) is represented as a red star.

74

FIGURE 4.3 ACROSS FAULT SOUTHWEST, SCEC CVM-S4.26
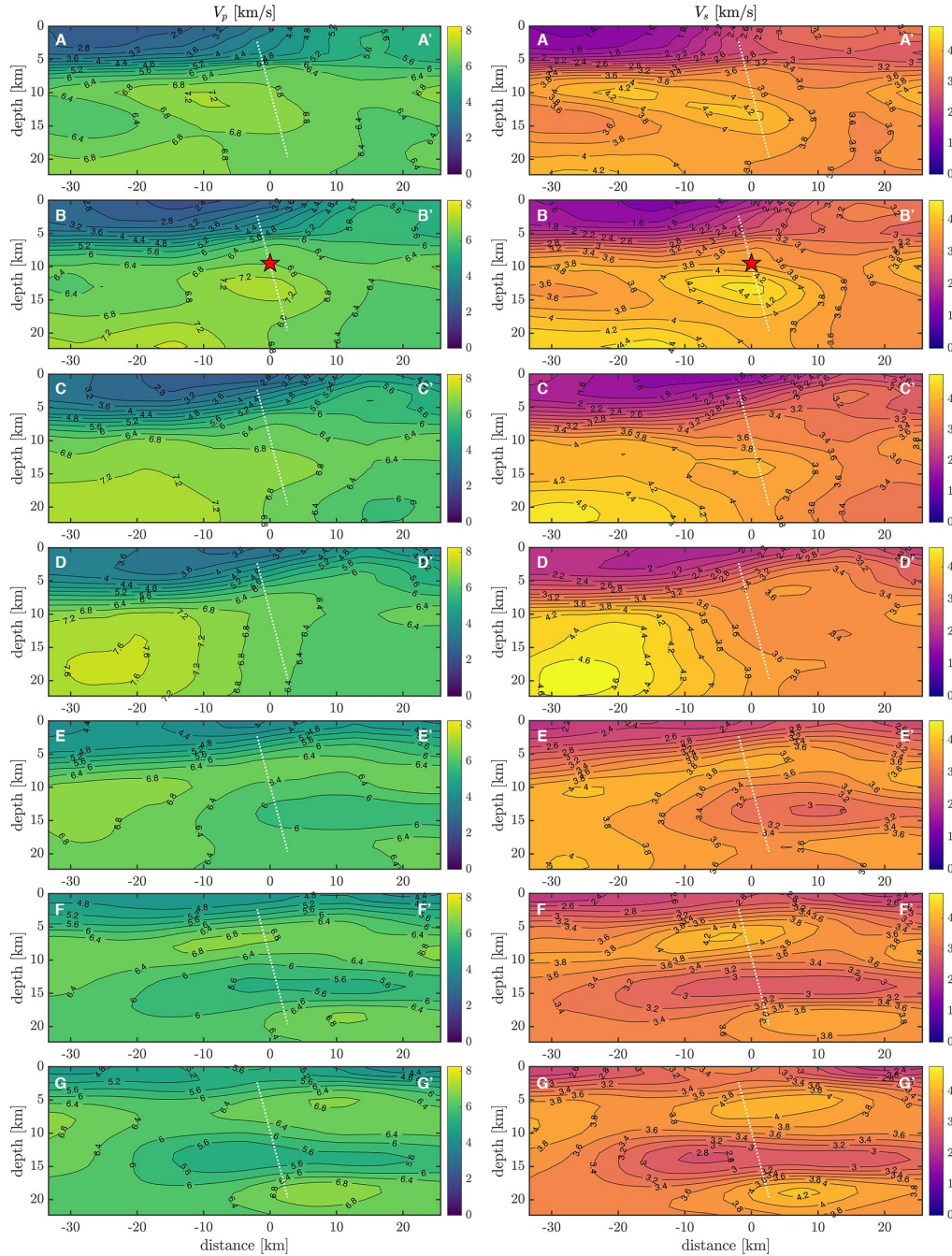
Figure 4.3: Across fault velocity structure [*Lee et al.*, 2014; *Small et al.*, 2017] corresponding to Figure 4.1. Cross sections (A–G) are made every 10 km, along strike. The earthquake epicenter is represented by a red star. Approximate Model 4 fault geometry is lined in white. Seismic velocities are in units of km/s.

Conclusion

We constrain the rupture history of the 1952 Kern County, California through the joint-analysis of seismic recordings and geodetic observations. Our results reveal that this large intraplate event, had a complex rupture history along a high dipping White Wolf fault, oriented N51°E and dipping 75° to the southeast.

The rupture initiated on a shallow dipping branch of White Wolf fault system with dominant left-lateral strike-slip motion (strike=49±4°, dip=35±1°, and rake=11±5°). The subsequent rupture on the White Wolf fault (strike=51°and dip=75°) was triggered approximately 2 s later. Over the next 5 s, the rupture broke asperity A (1.5×10^{19} Nm or M_W 6.75), which had a high average static stress drop (50 MPa). The moment release rate increased again over the next 7–8 s, breaking into sub-event B from its southwest edge. The rupture of this 18 km by 12 km, M_W 7.05 sub-event continued for another 10 s. The weighted average rake angle over the southwest fault segment was 47–57°. From there the rupture propagated along shallower depths to the northeast, where it broke asperities C and D. In contrast to asperities A and B, the ruptures within the northeastern fault plane have larger variations to rake with weighted average rake angles of 32–50°. The total rupture duration for this event is 23–26 s and has a cumulative moment of 7.61×10^{19} Nm, or M_W 7.18.

Appendix A

Additional Work

A.1   *S*-wave Radiation Patterns

In Chapter 3, we examined *P*-wave first-motion as observed from Berkeley and determined that the 1952 Kern County earthquake initiated with a nucleation event lasting at least 2 s. This interpretation led to the assertion that the work of *Gutenberg* [1955b] may be erroneous. What we left out in this chapter, was our work trying to compare observed *SV* and *SH* polarities to predicted radiation patterns in a forward calculation.

Given 21 teleseismic *S*-wave observations (30-90°) [*Gutenberg*, 1955b], we calculated *SV* and *SH* polarities based on the convention that positive values point away from the source. As magnification factors of these observations are unknown [*Gutenberg*, 1955b], we only consider their relative amplitudes. Using formulae provided by *Aki and Richards* [2002] we can plot these amplitudes atop predicted *SV* and *SH* radiation patterns and assess consistencies across given focal solutions (Figure A.1). Of all the solutions we assess, none of the predicted radiation patterns match all observations well. This suggests that this data is not adequate for constraining the degree of strike-slip and dip-slip motions and that Gutenberg's analysis is erroneous.

FIGURE A.1 PREDICTED S-WAVE POLARITIES AND OBSERVATIONS
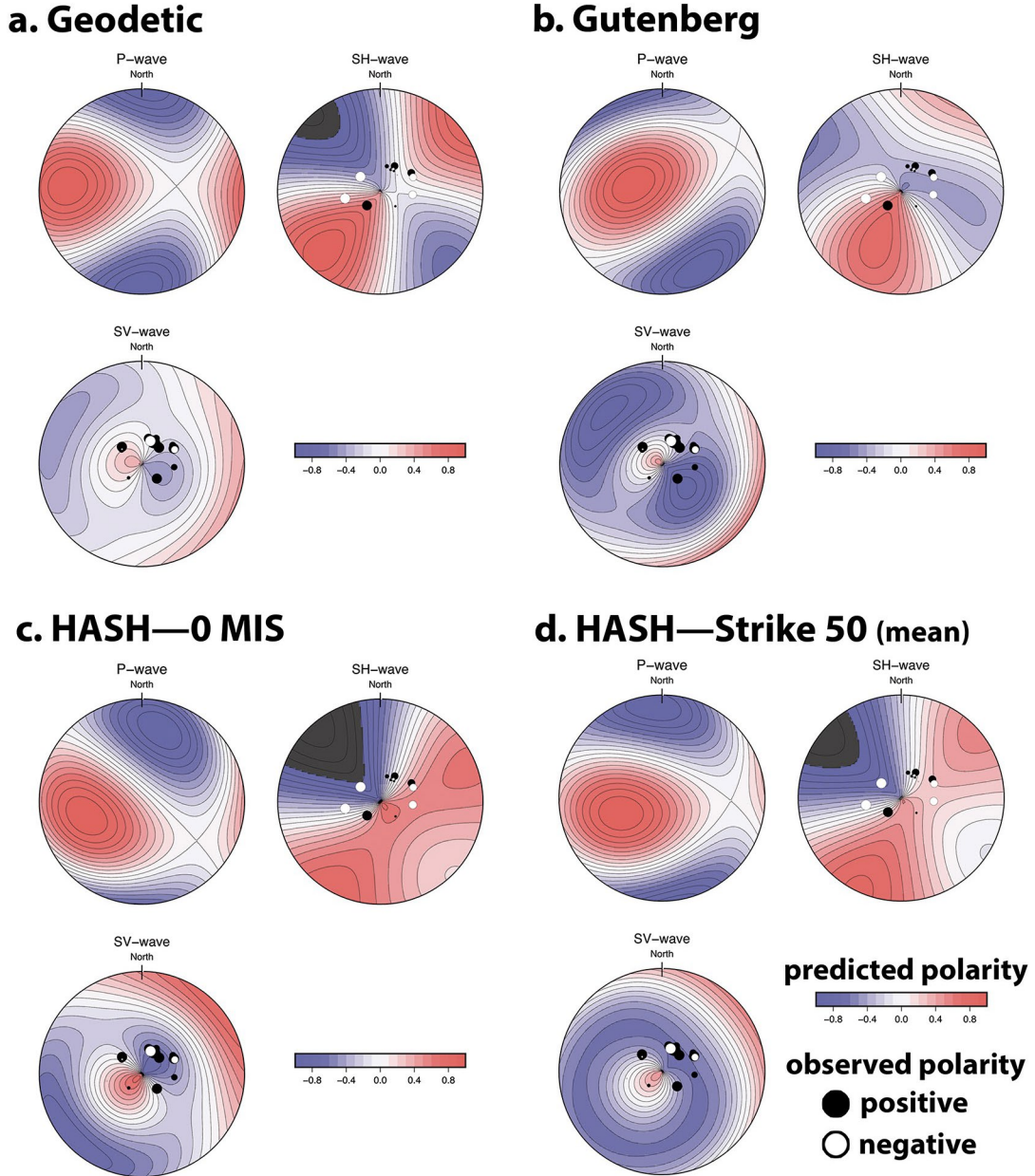
Figure A.1: Predicted radiation patterns [*Aki and Richards*, 2002] versus observed *SH* and *SV* polarities for 21 stations located at teleseismic distances (30–90°). White dots are expected to align with blue areas and black dots with red areas. The size of each dot corresponds to the amplitude of the observation. Of all the solutions we assess, none of the predicted radiation patterns match all observations well.

Appendix B

Tabels

B.1   Velocity Models

The 1D velocity structures used in our finite fault inversion are made by averaging along 2D, interpolated cross-sections of the SCEC CVM-S4.26 [*Lee et al.*, 2014; *Small et al.*, 2017]. Their corresponding plots can be found in Figure 3.6. The tabulated values for each velocity model can be found in the Tables B.1–B.5. There are five models in total: Kern County, Caltech, Hollywood, Santa Barbara, and Taft.

B.2   Adapted Geodetic Datasets

When we examined reported geodetic data in *Bawden* [2001], we found discrepancies between the tabulated station locations and corresponding figures. It appeared that several station locations had incorrect latitudes and longitudes. Luckily, we were able to locate the correct values through the National Geodetic Survey. The following Tables (B.6–B.9) reflect these changes and were used directly in our joint inversion.

TABLE B.1 VELOCITY STRUCTURE, KERN COUNTY (KERN)

Vp	Vs	ρ	z	Qp	Qs	Vp	Vs	ρ	z	Qp	Qs
3.3248	2.0092	2.3430	0	500	250	6.6231	3.8186	2.8690	25	500	250
3.4576	2.0939	2.3579	1	500	250	6.6402	3.8317	2.8752	26	500	250
3.8644	2.3437	2.4001	2	500	250	6.6552	3.8434	2.8803	27	500	250
4.2799	2.5739	2.4486	3	500	250	6.6592	3.8460	2.8805	28	500	250
4.7158	2.8178	2.5150	4	500	250	6.6482	3.8363	2.8742	29	500	250
5.2886	3.1321	2.6091	5	500	250	6.6363	3.8250	2.8676	30	500	250
5.9925	3.4514	2.7135	6	500	250	7.1615	4.1467	3.0399	31	1200	600
6.3470	3.6336	2.7827	7	500	250	7.6017	4.4145	3.1862	32	1200	600
6.5155	3.6744	2.7961	8	500	250	7.8975	4.5917	3.2837	33	1200	600
6.5540	3.6534	2.7828	9	500	250	7.8781	4.5777	3.2768	34	1200	600
6.5915	3.6398	2.7774	10	500	250	7.8542	4.5603	3.2676	35	1200	600
6.5944	3.6754	2.8026	11	500	250	7.8365	4.5480	3.2608	36	1200	600
6.6192	3.7185	2.8352	12	500	250	7.8333	4.5482	3.2601	37	1200	600
6.5979	3.7048	2.8363	13	500	250	7.8387	4.5607	3.2656	38	1200	600
6.5701	3.6787	2.8234	14	500	250	7.8440	4.5763	3.2727	39	1200	600
6.5410	3.6604	2.8087	15	500	250	7.8578	4.5940	3.2813	40	1200	600
6.5381	3.6796	2.8097	16	500	250	7.8703	4.6095	3.2891	41	1200	600
6.5699	3.7324	2.8282	17	500	250	7.8793	4.6209	3.2954	42	1200	600
6.6105	3.7918	2.8542	18	500	250	7.8807	4.6254	3.2985	43	1200	600
6.6462	3.8299	2.8728	19	500	250	7.8711	4.6200	3.2968	44	1200	600
6.6627	3.8491	2.8828	20	500	250	7.8443	4.5995	3.2873	45	1200	600
6.6606	3.8530	2.8855	21	500	250	7.7976	4.5616	3.2685	46	1200	600
6.6527	3.8523	2.8861	22	500	250	7.7355	4.5100	3.2419	47	1200	600
6.6272	3.8274	2.8734	23	500	250	7.6732	4.4575	3.2140	48	1200	600
6.6175	3.8163	2.8679	24	500	250	7.6229	4.4151	3.1910	49	1200	600

Table B.1: Layered velocity structure for Kern County, California (KERN) [*Lee et al.*, 2014; *Small et al.*, 2017]. *P*-wave velocity (Vp), *S*-wave velocity (Vs), density (ρ), layer depth in km (z) and quality factors (Qp & Qs).

TABLE B.2 VELOCITY STRUCTURE, CALTECH (CITA & CITL)

Vp	Vs	ρ	z	Qp	Qs	Vp	Vs	ρ	z	Qp	Qs
2.8415	1.5835	2.2232	0	500	250	6.8571	3.8257	2.8717	25	500	250
4.6500	2.6645	2.4701	1	500	250	6.8674	3.8273	2.8719	26	500	250
4.9290	2.8603	2.5139	2	500	250	6.8540	3.8096	2.8619	27	500	250
5.2220	3.0176	2.5478	3	500	250	6.8894	3.8511	2.8842	28	500	250
5.3553	3.0543	2.5568	4	500	250	6.9374	3.8817	2.9008	29	500	250
5.5140	3.1268	2.5787	5	500	250	7.2463	4.0756	3.0070	30	1200	600
5.9431	3.3720	2.6622	6	500	250	7.4402	4.1990	3.0743	31	1200	600
6.1940	3.5421	2.7321	7	500	250	7.4727	4.2248	3.0891	32	1200	600
6.3811	3.6702	2.7920	8	500	250	7.5997	4.3338	3.1458	33	1200	600
6.5257	3.7778	2.8468	9	500	250	7.5876	4.3247	3.1409	34	1200	600
6.6281	3.8607	2.8906	10	500	250	7.5982	4.3360	3.1471	35	1200	600
6.6029	3.8522	2.8856	11	500	250	7.6333	4.3682	3.1648	36	1200	600
6.5300	3.8033	2.8604	12	500	250	7.6855	4.4148	3.1903	37	1200	600
6.4270	3.7236	2.8210	13	500	250	7.7445	4.4751	3.2225	38	1200	600
6.3533	3.6620	2.7919	14	500	250	7.7906	4.5274	3.2498	39	1200	600
6.3023	3.6030	2.7635	15	500	250	7.8347	4.5708	3.2717	40	1200	600
6.3059	3.5678	2.7455	16	500	250	7.8668	4.6035	3.2878	41	1200	600
6.3588	3.5619	2.7411	17	500	250	7.8932	4.6296	3.3004	42	1200	600
6.4394	3.5741	2.7462	18	500	250	7.9118	4.6483	3.3093	43	1200	600
6.5177	3.6105	2.7634	19	500	250	7.9218	4.6593	3.3144	44	1200	600
6.5910	3.6491	2.7821	20	500	250	7.9204	4.6601	3.3147	45	1200	600
6.6494	3.6805	2.7978	21	500	250	7.9053	4.6487	3.3092	46	1200	600
6.6932	3.7032	2.8095	22	500	250	7.8735	4.6229	3.2967	47	1200	600
6.7674	3.7616	2.8387	23	500	250	7.8292	4.5860	3.2786	48	1200	600
6.8250	3.8048	2.8610	24	500	250	7.7819	4.5464	3.2588	49	1200	600

Table B.2: Layered velocity structure for Caltech, California (CITA & CITL) [*Lee et al.*, 2014; *Small et al.*, 2017]. *P*-wave velocity (Vp), *S*-wave velocity (Vs), density (ρ), layer depth in km (z) and quality factors (Qp & Qs).

TABLE B.3 VELOCITY STRUCTURE, HOLLYWOOD (HWSB)

Vp	Vs	ρ	z	Qp	Qs	Vp	Vs	ρ	z	Qp	Qs
2.8808	1.6202	2.2264	0	500	250	6.9002	3.8048	2.8608	25	500	250
4.1061	2.3838	2.4181	1	500	250	6.8872	3.7850	2.8496	26	500	250
4.5455	2.6360	2.4621	2	500	250	6.8653	3.7579	2.8351	27	500	250
4.8696	2.7603	2.4758	3	500	250	6.8551	3.7500	2.8315	28	500	250
5.0468	2.7870	2.4771	4	500	250	6.8685	3.7718	2.8439	29	500	250
5.2600	2.8817	2.5011	5	500	250	7.2424	4.0220	2.9792	30	1200	600
5.7658	3.2212	2.6093	6	500	250	7.4697	4.1793	3.0641	31	1200	600
6.0607	3.4357	2.6896	7	500	250	7.5129	4.2221	3.0878	32	1200	600
6.3012	3.5966	2.7590	8	500	250	7.6115	4.3353	3.1467	33	1200	600
6.4529	3.6964	2.8060	9	500	250	7.6266	4.3550	3.1571	34	1200	600
6.5484	3.7572	2.8370	10	500	250	7.6284	4.3604	3.1602	35	1200	600
6.5286	3.7459	2.8335	11	500	250	7.6502	4.3827	3.1725	36	1200	600
6.4970	3.7167	2.8223	12	500	250	7.6856	4.4163	3.1907	37	1200	600
6.4433	3.6589	2.7974	13	500	250	7.7308	4.4651	3.2167	38	1200	600
6.4084	3.6277	2.7826	14	500	250	7.7639	4.5063	3.2382	39	1200	600
6.4001	3.6049	2.7682	15	500	250	7.7931	4.5376	3.2543	40	1200	600
6.4371	3.6131	2.7667	16	500	250	7.8118	4.5587	3.2652	41	1200	600
6.5146	3.6477	2.7803	17	500	250	7.8256	4.5740	3.2730	42	1200	600
6.6100	3.6883	2.8005	18	500	250	7.8357	4.5853	3.2788	43	1200	600
6.6899	3.7210	2.8177	19	500	250	7.8434	4.5939	3.2831	44	1200	600
6.7558	3.7493	2.8329	20	500	250	7.8462	4.5976	3.2849	45	1200	600
6.8060	3.7664	2.8423	21	500	250	7.8415	4.5947	3.2835	46	1200	600
6.8353	3.7688	2.8441	22	500	250	7.8264	4.5824	3.2773	47	1200	600
6.8766	3.7992	2.8594	23	500	250	7.8026	4.5625	3.2671	48	1200	600
6.8985	3.8109	2.8649	24	500	250	7.7762	4.5402	3.2553	49	1200	600

Table B.3: Layered velocity structure for Hollywood, California (HWSB) [*Lee et al.*, 2014; *Small et al.*, 2017]. *P*-wave velocity (Vp), *S*-wave velocity (Vs), density (ρ), layer depth in km (z) and quality factors (Qp & Qs).

Vp	Vs	ρ	z	Qp	Qs	Vp	Vs	ρ	z	Qp	Qs
4.5912	2.5045	2.4228	0	500	250	6.6795	3.8108	2.8691	25	500	250
4.5923	2.4941	2.4207	1	500	250	6.6744	3.8111	2.8687	26	500	250
4.7113	2.5345	2.4272	2	500	250	6.6655	3.8076	2.8658	27	500	250
4.8134	2.5716	2.4338	3	500	250	6.6546	3.8016	2.8610	28	500	250
4.9706	2.6702	2.4544	4	500	250	6.9954	4.0249	2.9806	29	500	250
5.3086	2.9231	2.5148	5	500	250	7.5715	4.3818	3.1702	30	1200	600
5.9555	3.3267	2.6479	6	500	250	7.8046	4.5254	3.2474	31	1200	600
6.2420	3.5550	2.7403	7	500	250	7.7793	4.5049	3.2371	32	1200	600
6.3599	3.6270	2.7708	8	500	250	7.7596	4.4892	3.2289	33	1200	600
6.4032	3.6524	2.7823	9	500	250	7.7527	4.4842	3.2262	34	1200	600
6.4314	3.6734	2.7933	10	500	250	7.7581	4.4895	3.2290	35	1200	600
6.4043	3.6654	2.7921	11	500	250	7.7710	4.5013	3.2350	36	1200	600
6.3634	3.6452	2.7862	12	500	250	7.7868	4.5153	3.2422	37	1200	600
6.2951	3.5882	2.7623	13	500	250	7.8061	4.5348	3.2523	38	1200	600
6.2376	3.5612	2.7500	14	500	250	7.8139	4.5461	3.2581	39	1200	600
6.1996	3.5339	2.7360	15	500	250	7.8154	4.5489	3.2598	40	1200	600
6.2276	3.5426	2.7373	16	500	250	7.8095	4.5463	3.2587	41	1200	600
6.3052	3.5873	2.7562	17	500	250	7.8044	4.5435	3.2577	42	1200	600
6.4180	3.6552	2.7886	18	500	250	7.8011	4.5417	3.2572	43	1200	600
6.5048	3.7087	2.8152	19	500	250	7.7999	4.5413	3.2574	44	1200	600
6.5779	3.7528	2.8381	20	500	250	7.8006	4.5425	3.2585	45	1200	600
6.6372	3.7847	2.8552	21	500	250	7.8035	4.5458	3.2605	46	1200	600
6.6847	3.8063	2.8672	22	500	250	7.8082	4.5503	3.2629	47	1200	600
6.6856	3.8097	2.8690	23	500	250	7.8154	4.5567	3.2661	48	1200	600
6.6834	3.8110	2.8694	24	500	250	7.8250	4.5651	3.2701	49	1200	600

Table B.4: Layered velocity structure for Santa Barbara, California (SBCH) [*Lee et al.*, 2014; *Small et al.*, 2017]. *P*-wave velocity (Vp), *S*-wave velocity (Vs), density (ρ), layer depth in km (z) and quality factors (Qp & Qs).

TABLE B.5 VELOCITY STRUCTURE, TAFT (TAFT)

Vp	Vs	ρ	z	Qp	Qs	Vp	Vs	ρ	z	Qp	Qs
2.9977	1.6712	2.4228	0	500	250	7.0022	4.1362	2.8691	25	500	250
3.0556	1.7027	2.4207	1	500	250	7.0373	4.1669	2.8687	26	500	250
3.1785	1.7601	2.4272	2	500	250	7.0489	4.1773	2.8658	27	500	250
3.2818	1.7939	2.4338	3	500	250	7.0239	4.1569	2.8610	28	500	250
3.5683	1.9409	2.4544	4	500	250	6.9585	4.1030	2.9806	29	500	250
4.2109	2.3300	2.5148	5	500	250	6.8807	4.0363	3.1702	30	500	250
5.2539	2.9357	2.6479	6	500	250	8.1653	4.8374	3.2474	31	1200	600
5.9535	3.5030	2.7403	7	500	250	8.0914	4.7781	3.2371	32	1200	600
6.4443	3.8593	2.7708	8	500	250	8.0101	4.7133	3.2289	33	1200	600
6.7176	4.0522	2.7823	9	500	250	7.9378	4.6556	3.2262	34	1200	600
6.8952	4.1541	2.7933	10	500	250	7.8761	4.6066	3.2290	35	1200	600
6.8032	4.0745	2.7921	11	500	250	7.8262	4.5675	3.2350	36	1200	600
6.7025	3.9753	2.7862	12	500	250	7.7871	4.5375	3.2422	37	1200	600
6.5789	3.8511	2.7623	13	500	250	7.7521	4.5139	3.2523	38	1200	600
6.4758	3.7392	2.7500	14	500	250	7.7158	4.4916	3.2581	39	1200	600
6.4249	3.6871	2.7360	15	500	250	7.6903	4.4745	3.2598	40	1200	600
6.4323	3.6991	2.7373	16	500	250	7.6778	4.4661	3.2587	41	1200	600
6.4845	3.7530	2.7562	17	500	250	7.6751	4.4654	3.2577	42	1200	600
6.5715	3.8272	2.7886	18	500	250	7.6810	4.4719	3.2572	43	1200	600
6.6371	3.8659	2.8152	19	500	250	7.6947	4.4847	3.2574	44	1200	600
6.7081	3.9093	2.8381	20	500	250	7.7125	4.5008	3.2585	45	1200	600
6.7916	3.9668	2.8552	21	500	250	7.7295	4.5158	3.2605	46	1200	600
6.8948	4.0451	2.8672	22	500	250	7.7380	4.5231	3.2629	47	1200	600
6.9192	4.0651	2.8690	23	500	250	7.7353	4.5202	3.2661	48	1200	600
6.9580	4.0984	2.8694	24	500	250	7.7260	4.5115	3.2701	49	1200	600

Table B.5: Layered velocity structure for Taft, California (TAFT) [*Lee et al.*, 2014; *Small et al.*, 2017]. *P*-wave velocity (Vp), *S*-wave velocity (Vs), density (ρ), layer depth in km (z) and quality factors (Qp & Qs).

#	Latitude	Longitude	Station	#	Latitude	Longitude	Station
1	35.14083	-118.47190	3848_USGS	20	34.81027	-118.88361	C_54
2	35.18472	-118.50889	C_56	21	34.83500	-118.86417	D_54
3	35.19444	-118.52278	B_56	22	34.83500	-118.86417	D_54
4	35.19694	-118.53750	3064_USGS	23	34.84528	-118.86972	F_54
5	35.20472	-118.53417	A_56	24	34.86777	-118.88333	G_54
6	35.21083	-118.55138	2719_USGS	25	34.88806	-118.90667	H_54
7	35.22556	-118.55806	Z_55	26	34.91000	-118.92360	J_54
8	35.23889	-118.57694	2410_USGS	27	34.92722	-118.92583	K_54
9	35.24639	-118.58222	Y_55	28	34.94111	-118.93028	T_824
10	35.27138	-118.62416	W_55	29	34.95639	-118.93556	M_54
11	35.27527	-118.63527	1732_USGS	30	34.98222	-118.94278	N_54
12	35.27361	-118.64583	V_55	31	34.99389	-118.94694	S_604
13	35.28138	-118.64833	U_55	32	35.02000	-118.95444	E_608
14	35.29028	-118.62833	T_55	33	35.03472	-118.95889	P_64
15	35.29638	-118.66333	S_55	34	35.04861	-118.96361	R_824
16	35.30305	-118.67416	R_55	35	35.07889	-118.97390	S_824
17	35.32166	-118.70944	Q_55	36	34.99444	-118.99972	V_604
18	34.78417	-118.81556	A_54	37	35.00778	-119.01310	X_604
19	34.79583	-118.85167	B_54				

Table B.6: Kern County leveling stations used in finite-fault inversion. Adapted from *Bawden* [2001], this list of leveling stations have been corrected in accordance with the National Geodetic Survey.

TABLE B.7 LEVELING ELEVATION CHANGES

# From	# To	Elev. Δ [cm]	σ	# From	# To	Elev. Δ [cm]	σ
1	2	3.42	0.33	19	20	2.59	0.40
2	3	1.06	0.33	20	21	1.04	0.38
3	4	2.75	0.33	22	23	3.38	0.33
4	5	-1.25	0.33	23	24	4.85	0.34
5	6	2.38	0.33	24	25	5.00	0.38
6	7	0.12	0.36	25	26	7.00	0.36
7	8	4.47	0.33	27	28	6.49	0.33
8	9	-0.43	0.56	28	29	6.02	0.33
9	10	-7.71	0.33	29	30	5.87	0.34
10	11	-14.01	0.33	30	31	-1.38	0.33
11	12	-11.2	0.33	31	32	-5.61	0.34
12	13	2.89	0.38	32	33	-9.85	0.33
13	14	15.54	0.38	33	34	-15.56	0.33
14	15	-13.02	0.38	34	35	-37.09	0.38
15	16	7.28	0.33	31	36	3.82	0.46
16	17	7.22	0.41	36	37	-14.42	0.38
18	19	1.61	0.40				

Table B.7: Kern County leveling observations [*Bawden*, 2001] used in the finite-fault inversion. Elevations are in units of [cm] and correspond to relative changes between two leveling stations, represented has a number in the "# From" and "# To" columns. Station numbers and locations are detailed in Table B.6.

TABLE B.8 TRIANGULATION STATIONS

#	Latitude	Longitude	Station	#	Latitude	Longitude	Station
1	34.9769	-118.3480	ACROSS	28	35.0106	-118.3662	LIMESTONE
2	35.2014	-118.9676	ADOBE	29	34.7975	-118.3074	LITTLE B
3	34.9001	-118.3588	BAJADA	30	34.8083	-118.3603	LOPE
4	35.0942	-118.4132	BED	31	35.1290	-118.7438	MART
5	35.1619	-118.6973	BLACK OAK	32	35.1260	-118.3654	MONOLITH
6	35.1257	-118.5299	BRITE	33	34.8521	-118.3704	MOVE
7	35.0720	-118.3339	CAMERON	34	34.7457	-118.3251	NUMBER RES
8	35.1471	-118.4576	CHAPI	35	34.8321	-118.3152	OLD RESET
9	35.1052	-118.8055	COMMANCH	36	35.1207	-118.2946	PAJUELA
10	35.1633	-118.5799	CUB	37	35.0776	-118.3061	PASS
11	35.0858	-118.5077	DEER	38	35.0581	-118.3929	QUARTZ
14	35.0333	-118.4867	DOUBLE	39	34.9889	-118.3264	QUICK
15	35.0745	-118.8644	EL PASO	40	35.1381	-118.6703	R. SPRINGS
16	34.8802	-118.3008	FAULT	41	34.8050	-118.3525	SAND
17	35.0906	-118.5427	FENCE	42	34.6931	-118.5614	SAWMILL*
18	35.1393	-118.6458	FLANNAGAN	43	35.0991	-118.6021	SCHOOL
19	34.9612	-118.2830	GOLD	44	35.0854	-118.3543	SHRUB 2
20	35.0480	-118.7664	GORGE	45	34.8633	-118.3265	SINGLE 2
21	35.1128	-118.7226	HORSETHIEF	46	34.9825	-118.1888	SOLEDAD
22	35.0890	-118.6604	JACKS	47	34.9128	-118.3000	STRAIGHT
23	35.1211	-118.5567	JAIL	48	35.1336	-118.4093	SUMMIT
24	34.8496	-118.3645	JOSHUA	49	34.9364	-118.3095	T10N R14
25	35.4142	-118.9658	KERN 3 RES	50	35.1238	-118.8226	TEJON
26	35.0996	-118.4820	KILN	51	34.9456	-118.3533	WASH
27	34.9558	-118.5733	LIEBRE	52	35.0105	-119.0144	WHEELER

Table B.8: Kern County triangulation stations used in finite-fault inversion. Adapted from *Bawden* [2001], this list of triangulation stations have been corrected in accordance with the National Geodetic Survey.

TABLE B.9 TRIANGULATION ANGLE CHANGES

A	V	B	$\Delta\theta$	A	V	B	$\Delta\theta$	A	V	B	$\Delta\theta$	A	V	B	$\Delta\theta$
5	2	57	7.36	6	11	8	-4.49	22	21	45	0.93	6	48	18	2.19
16	2	57	4.88	6	11	27	-1.55	33	21	22	0.87	10	48	24	0.66
27	4	53	0.54	8	11	27	2.48	23	22	21	-9.66	18	48	23	-4.60
49	4	27	0.70	18	11	6	-1.28	45	22	21	-2.43	19	48	10	-7.30
53	4	35	-1.39	18	11	8	-5.18	45	22	23	6.98	23	48	6	2.04
53	4	49	0.91	18	11	24	-1.16	19	23	48	-1.42	23	48	19	7.64
10	5	14	3.41	18	11	27	-2.83	22	23	19	-3.97	23	48	24	1.54
10	5	19	2.41	5	14	19	0.53	22	23	45	-0.84	23	48	45	4.78
19	5	14	1.23	18	14	10	3.76	33	23	19	-2.93	24	48	6	0.28
55	5	2	-5.71	19	14	18	-4.35	33	23	45	-1.18	45	48	19	2.85
57	5	55	-1.08	19	14	39	-4.95	33	23	48	-4.51	4	49	53	0.66
8	6	11	1.76	57	14	19	6.24	45	23	19	-3.08	53	49	35	0.95
8	6	18	3.38	2	16	55	0.77	6	24	11	-1.67	4	53	27	-1.17
8	6	27	3.47	9	16	33	-3.09	6	24	18	1.08	8	53	35	0.42
8	6	48	-1.80	21	16	57	7.81	6	24	48	-4.68	27	53	8	1.49
11	6	18	1.65	33	16	21	-3.86	11	24	18	2.75	35	53	27	-1.91
18	6	48	-5.18	55	16	9	2.96	18	24	48	-5.82	35	53	49	-0.28
27	6	11	-1.10	55	16	33	0.70	5	26	57	4.12	49	53	4	0.40
48	6	24	1.94	57	16	2	-5.42	6	27	8	-6.80	2	55	5	5.27
4	8	27	1.68	57	16	9	-3.33	53	27	4	2.31	5	55	21	-8.96
11	8	6	1.44	57	16	33	-4.21	9	33	55	-3.74	5	55	33	-5.99
27	8	11	0.67	57	16	55	-5.53	16	33	9	-1.58	5	55	57	1.72
53	8	6	2.41	10	18	24	-1.54	21	33	16	1.93	16	55	57	2.28
53	8	11	0.97	14	18	19	0.78	23	33	21	-8.87	21	55	16	8.01
53	8	27	1.36	19	18	39	-5.87	45	33	21	-5.51	33	55	21	-2.97
21	9	16	4.04	5	19	10	-4.73	45	33	23	1.45	57	55	2	-6.70
33	9	16	5.22	10	19	14	8.54	4	35	53	1.15	2	57	16	0.65
33	9	21	1.96	10	19	18	9.08	53	35	39	-1.72	2	57	55	-0.76
14	10	18	1.61	10	19	23	3.21	18	39	35	-0.85	5	57	14	1.06
18	10	48	-6.59	10	19	48	10.17	49	39	35	0.87	5	57	16	1.25
19	10	5	1.01	18	19	14	-0.62	19	45	23	3.13	26	57	2	-0.66
39	10	5	-4.19	23	19	45	-0.05	19	45	48	3.91	26	57	5	-0.98
39	10	18	2.01	45	19	5	1.46	21	45	22	1.64	55	57	5	-0.82
39	10	19	-5.54	45	19	10	-3.16	22	45	33	1.52	55	21	9	7.70
39	10	48	-5.04	48	19	23	-6.96	23	45	21	-4.43				
48	10	19	-0.70	16	21	55	-7.84	48	45	23	-0.78				

Table B.9: A, V and B are triangle vertices of stations numbered in Table B.8. $\Delta\theta$ is the angle change clockwise from AV to BV and are in units of arc s [*Bawden*, 2001].

Bibliography

Aki, K., and P. G. Richards (2002), *Quantitative Seismology*, 2nd ed., 700 pp., University Science Books, doi:10.1016/S0065-230X(09)04001-9.

Atkinson, G. M., and D. J. Wald (2007), "Did You Feel It?" Intensity Data: A Surprisingly Good Measure of Earthquake Ground Motion, *Seismological Research Letters*, *78*(3), 362–368, doi:10.1785/gssrl.78.3.362.

Bakun, W. H. (2006), Estimating Locations and Magnitudes of Earthquakes in Southern California from Modified Mercalli Intensities, *Bulletin of the Seismological Society of America*, *96*(4A), 1278–1295, doi:10.1785/0120050205.

Bawden, G. W. (2001), Source parameters for the 1952 Kern County earthquake, California: A joint inversion of leveling and triangulation observations, *Journal of Geophysical Research-Solid Earth*, *106*(B1), 771–785.

Bawden, G. W., A. Donnellan, L. H. Kellogg, D. Dong, and J. B. Rundle (1997), Geodetic measurements of horizontal strain near the White across The Kern County earthquake was the iargest Eocene-Pliocene, *Journal of Geophysical Research*, *102*(B3), 4957–4967.

Ben-Menahem, A. (1978), Source mechanism of the 1906 San Francisco earthquake, *Physics of the Earth and Planetary Interiors*, *17*(2), 163–181, doi:10.1016/0031-9201(78)90057-2.

Benioff, H. (1955), Seismograph Development in California, *California Division of Mines Bulletin: Earthquakes in Kern County, 1952, 171*, 147–151.

Bolt, B. A. (1978), Letters to the Editor: The Local Magnitude ML of the Kern County Earthquake of July 21, 1952, *Bulletin of the Seismological Society of America, 68*(2), 513–515.

Boore, D. M. (1983), Stochastic simulation of high-frequency ground motions based on seismological models of the radiated spectra, *Bulletin of the Seismological Society of America, 73*(6A), 1865–1894.

Brune, J. N. (1970), Tectonic stress and the spectra of seismic shear waves from earthquakes, *Journal of geophysical research, 75*(26), 4997–5009.

Brune, J. N., A. Anooshehpoor, B. Shi, and Y. Zheng (2004), Precarious rock and overturned transformer evidence for ground shaking in the Ms 7.7 Kern County earthquake: An analog for disastrous shaking from a major thrust fault in the Los Angeles basin, *Bulletin of the Seismological Society of America, 94*(6), 1993–2003, doi: 10.1785/0120030252.

Castillo, D. A., and M. D. Zoback (1995), Systematic stress variations in the southern San Joaquin Valley and along the White Wolf Fault: implications for the rupture mechanics of the 1952 Ms7.8 Kern County earthquake and contemporary seismicity, *Journal of Geophysical Research, 100*(B4), 6249–6264, doi:10.1029/94JB02476.

Dreger, D., and B. Savage (1999), Aftershocks of the 1952 Kern County, California, earthquake sequence, *Bulletin of the Seismological Society of America, 89*(4), 1094–1108.

Dunbar, W. S., D. M. Boore, and W. Thatcher (1980), Pre-, co-, and postseismic strain

changes associated with the 1952 ML = 7.2 Kern County, California, earthquake, *Bulletin of the Seismological Society of America*, *70*(5), 1893–1905.

Dziewonski, A. M., T. A. Chou, and J. H. Woodhouse (1981), Determination of earthquake source parameters from waveform data for studies of global and regional seismicity., *Journal of Geophysical Research*, *86*(B4), 2825–2852, doi: 10.1029/JB086iB04p02825.

Ekström, G., M. Nettles, and A. M. Dziewoński (2012), The global CMT project 2004-2010: Centroid-moment tensors for 13,017 earthquakes, *Physics of the Earth and Planetary Interiors*, *200-201*, 1–9, doi:10.1016/j.pepi.2012.04.002.

Ellsworth, W., and G. Beroza (1995), Seismic evidence for an earthquake nucleation phase, *Science*, *268*(5212), 851–855.

Gubbins, D. (2004), *Time series analysis and inverse theory for geophysicists*, Cambridge University Press.

Gutenberg, B. (1955a), Magnitude Determination for Large Kern County Shocks, 1952; Effects of Station Azimuth and Calculation Meathods, *California Division of Mines Bulletin: Earthquakes in Kern County, 1952*, *171*, 171–175.

Gutenberg, B. (1955b), The First Motion in Longitudinal and Transverse Waves of the Main Shock and the Direction of Slip, *California Division of Mines Bulletin: Earthquakes in Kern County, 1952*, *171*, 165–170.

Gutenberg, B. (1955c), Epicenter and Origin Time of the Main Shock on July 21 and Travel Times of Major Phases, *California Division of Mines Bulletin: Earthquakes in Kern County, 1952*, *171*, 157–163.

Gutenberg, B., and C. F. Richter (1942), Earthquake magnitude, intensity, energy and acceleration, *Bulletin of the Seismological Society of America*, *32*(3), 163–191.

Gutenberg, B., and C. F. Richter (1955), Magnitude and energy of earthquakes, *Nature*, *176*(4486), 795–795.

Hanks, T. C., and H. Kanamori (1979), A moment magnitude scale, *Journal of Geophysical Research B: Solid Earth*, *84*(B5), 2348–2350, doi:10.1029/JB084iB05p02348.

Hardebeck, J. L., and P. M. Shearer (2002), A new method for determining first-motion focal mechanisms, *Bulletin of the Seismological Society of America*, *92*(6), 2264–2276, doi:10.1785/0120010200.

Hartzell, S., P. Liu, and C. Mendoza (1996), The 1994 Northridge, California, earthquake: Investigation of rupture velocity, risetime, and high-frequency radiation, *Journal of Geophysical Research: Solid Earth*, *101*(B9), 20,091–20,108, doi:10.1029/96jb01883.

Hearn, E., F. Pollitz, W. Thatcher, and C. Onishi (2013), How do "ghost transients" from past earthquakes affect gps slip rate estimates on southern california faults?, *Geochemistry, Geophysics, Geosystems*, *14*(4), 828–838.

Heaton, T., and D. V. Helmberger (1979), Generalized Ray Models of the San Fernando Earthquake, *Bulletin of the Seismological Society of America*, *69*(5), 1311.

Hough, S. E., V. C. Tsai, R. Walker, and F. Aminzadeh (2017), Was the Mw 7.5 1952 Kern County, California, earthquake induced (or triggered)?, *Journal of Seismology*, *21*(6), 1613–1621, doi:10.1007/s10950-017-9685-x.

Huang, Z., and D. Zhao (2013), Mechanism of the 2011 tohoku-oki earthquake (mw 9.0) and tsunami: Insight from seismic tomography, *Journal of Asian Earth Sciences*, *70*, 160–168.

Hutton, L. K., and D. M. Boore (1987), The Ml Scale in Southern California, *Bulletin Of The Seismological Society Of America*, *77*(6), 2074–2094.

Ji, C., D. J. Wald, and D. V. Helmberger (2002a), Source description of the 1999 Hector Mine, California, earthquake, part I: Wavelet domain inversion theory and resolution analysis, *Bulletin of the Seismological Society of America*, *92*(4), 1192–1207, doi:10.1785/0120000916.

Ji, C., D. J. Wald, and D. V. Helmberger (2002b), Source description of the 1999 Hector Mine, California, earthquake, part II: Complexity of slip history, *Bulletin of the Seismological Society of America*, *92*(4), 1208–1226, doi:10.1785/0120000917.

Kanamori, H., and D. L. Anderson (1975), Theoretical basis of some empirical relations in seismology, *Bulletin of the seismological society of America*, *65*(5), 1073–1095.

Kanamori, H., and D. Hadley (1975), Crustal structure and temporal velocity change in southern California, *Pure and Applied Geophysics PAGEOPH*, *113*(1), 257–280, doi:10.1007/BF01592916.

Kanamori, H., and P. Jennings (1978), Determination of local magnitude, ML, from strong-motion accelerograms, *Bulletin of the Seismological Society of America*, *68*(2), 471–485.

Lee, E. J., P. Chen, T. H. Jordan, P. B. Maechling, M. A. Denolle, and G. C. Beroza (2014), Full-3-D tomography for crustal structure in Southern California based on the scattering-integral and the adjoint-wavefield methods, *Journal of Geophysical Research: Solid Earth*, *119*(8), 6421–6451, doi:10.1002/2014JB011346.

Lee, W. H. K., H. Meyers, K. Shimazaki, and B. H. Lee (1988), *Historical seismograms and earthquakes of the world*, Academic Press.

Lian-She Zhao, and D. V. Helmberger (1994), Source estimation from broadband regional seismograms, *Bulletin - Seismological Society of America*, *84*(1), 91–104.

Mallat, S. (1999), *A wavelet tour of signal processing*, Elsevier.

Oakeshott, G. B. (1955), The kern county earthquakes in california's geologic history, *California Division of Mines Bulletin: Earthquakes in Kern County, 1952*, *171*, 15–22.

Rabiner, L. R., J. H. McClellan, and T. W. Parks (1975), Fir digital filter design techniques using weighted chebyshev approximation, *Proceedings of the IEEE*, *63*(4), 595–610.

Richter, C. F. (1935), An instrumental earthquake magnitude scale, *Bulletin of the seismological society of America*, *25*(1), 1–32.

Richter, C. F. (1955), Seismic History in the San Joaquin Valley, *California Division of Mines Bulletin: Earthquakes in Kern County, 1952*, *171*, 143–146.

Rothman, D. H. (1985), Nonlinear inversion, statistical mechanics, and residual statics estimation, *Geophysics*, *50*(12), 2784–2796.

Rothman, D. H. (1986), Automatic estimation of large residual statics corrections., *Geophysics*, *51*(2), 332–346, doi:10.1190/1.1442092.

Salditch, L., S. E. Hough, S. Stein, B. D. Spencer, E. M. Brooks, J. S. Neely, and M. C. Lucas (2018), The 1952 Kern County, California earthquake: A case study of issues in the analysis of historical intensity data for estimation of source parameters, *Physics of the Earth and Planetary Interiors*, *283*(April), 140–151, doi:10.1016/j.pepi.2018.08.007.

Sen, M. K., and P. L. Stoffa (1990), Nonlinear seismic waveform inversion in one dimension using simulated annealing, *1990 SEG Annual Meeting*, *56*(10), 1119–1122.

Shao, G., and C. Ji (2012), What the exercise of the SPICE source inversion validation BlindTest 1 did not tell you, *Geophysical Journal International, 189*(1), 569–590, doi: 10.1111/j.1365-246X.2012.05359.x.

Small, P., D. Gill, P. J. Maechling, R. Taborda, S. Callaghan, T. H. Jordan, K. B. Olsen, G. P. Ely, and C. Goulet (2017), The SCEC unified community velocity model software framework, *Seismological Research Letters, 88*(6), 1539–1552, doi:10.1785/0220170082.

Stein, R. S., and W. Thatcher (1981), Seismic and aseismic deformation associated with the 1952 Kern County, California, earthquake and relationship to the Quaternary history of the White Wolf Fault., *Journal of Geophysical Research, 86*(B6), 4913–4928, doi:10.1029/JB086iB06p04913.

Trifunac, M. (1974), A three-dimensional dislocation model for the san fernando, california, earthquake of february 9, 1971, *Bulletin of the Seismological Society of America, 64*(1), 149–172.

Yamada, M., and K. Ohkitani (1991), Orthonormal wavelet analysis of turbulence, *Fluid Dynamics Research, 8*(1-4), 101–115, doi:10.1016/0169-5983(91)90034-G.